STUDY OF AlN/FSMA MAGNETOELECTRIC HETEROSTRUCTURE FOR MEMS APPLICATIONS

Ph.D. THESIS

by

SHUVAM PAWAR

CENTRE OF NANOTECHNOLOGY
INDIAN INSTITUTE OF TECHNOLOGY ROORKEE
ROORKEE- 247667 (INDIA)
OCTOBER, 2020


भारतीय प्रौद्योगिकी संस्थान रुड़की
INDIAN INSTITUTE OF TECHNOLOGY ROORKEE

STUDY OF AlN/FSMA MAGNETOELECTRIC HETEROSTRUCTURE FOR MEMS APPLICATIONS

A THESIS

Submitted in partial fulfilment of the
requirements for the award of the degree
of

DOCTOR OF PHILOSOPHY
in
NANOTECHNOLOGY

by
SHUVAM PAWAR

CENTRE OF NANOTECHNOLOGY
INDIAN INSTITUTE OF TECHNOLOGY ROORKEE
ROORKEE- 247667 (INDIA)
OCTOBER, 2020


भारतीय प्रौद्योगिकी संस्थान रुड़की
INDIAN INSTITUTE OF TECHNOLOGY ROORKEE


भारतीय प्रौद्योगिकी संस्थान रुड़की
INDIAN INSTITUTE OF TECHNOLOGY ROORKEE

INDIAN INSTITUTE OF TECHNOLOGY ROORKEE

STUDENT'S DECLARATION

I hereby certify that the work which is being presented in the thesis entitled **"STUDY OF AIN/FSMA MAGNETOELECTRIC HETEROSTRUCTURE FOR MEMS APPLICATIONS"** is my own work carried out during a period from 8th July, 2015 to 5th June, 2020 under the supervision of Dr. Davinder Kaur, Professor, Centre of Nanotechnology, Indian Institute of Technology Roorkee, Roorkee.

The matter presented in this thesis has not been submitted by me for the award of any other degree of this or any other Institute.

Dated: ____________ **Signature of the Student**

SUPERVISOR'S DECLARATION

This is to certify that the above mentioned work is carried out under my supervision.

Dated: ____________ **Signature of Supervisor(s)**


भारतीय प्रौद्योगिकी संस्थान रुड़की
INDIAN INSTITUTE OF TECHNOLOGY ROORKEE

ABSTRACT

In the current era, the progress of electronic technology is directly coupled with the advancement made in materials science. Magnetoelectric materials are the potential candidate for several multifunctional devices such as magnetic random-access memory, switches, magnetic sensors and tunable resonators. In these kinds of composites, the Magnetoelectric (ME) response is a product tensor property, i.e., outcome of the mechanical interaction between the magnetostrictive effect (magnetic/mechanical effect) occurring in the magnetic phase and the piezoelectric effect (mechanical/electrical effect) present in the piezoelectric phase. The ME coupling is observed in diverse structures such as bulk ceramic, two and three-phase ME composites and nanostructured thin films. However, the ME composite thin films have attracted enormous attention because different phases can be attached and designed at the atomic level with higher precision and sharp interface. Furthermore, nanostructured thin film composites enable the researchers to investigate the physical cause of the ME coupling effect at the nanoscale level.

The strength of the ME coupling depends on many factors, such as interface quality, high anisotropy magnetostriction, lattice mismatching, and functional characteristics of the individual piezoelectric and magnetostrictive layers. The ideal candidates for magnetostrictive and piezoelectric layers are ferromagnetic shape memory alloys (like-NiMnIn, NiMnSb, etc.) and AlN, respectively. Ferromagnetic shape memory alloys (FSMAs) exhibit a large applied magnetic field and temperature induced strain in the temperature region during the martensite to austenite phase transition as compared to leading magnetostrictive materials such as Trefnol-D and metglas. The NiMnIn exhibits giant magnetostriction coefficient at room temperature with multiple degrees of freedom to tune its magnetostriction, i.e., by varying temperature, magnetic field, stress. On the other hand, Aluminium Nitride (AlN) is a lead-free complementary metal-oxide-semiconductor (CMOS) compatible piezoelectric material with a high value of voltage piezoelectric coefficient (e_{33}). The deposition process of AlN is also well reproducible, and its chemical compatibility is well suited with semiconductor fabrication technology. For strong coupling between ferromagnetic and piezoelectric layers in the artificial magnetoelectric heterostructure, it is desirable to fabricate high-quality thin films with a sharp interface that can be attained by several growth techniques such as molecular beam epitaxy, pulsed laser deposition, metal oxide chemical vapor deposition, sputtering.

The main objectives of the thesis are (i) Fabrication of c-axis oriented AlN thin films using sputtering, and its characterization for electronics and microelectromechanical system applications (ii) Study and fabrication of strong ME response in silicon integrated FSMA and AlN based artificial thin film multiferroics structures. (iii) Synthesis and characterization of magnetic field tunable ferromagnetic shape memory alloy based piezo-resonator. A chapter-wise summary of the thesis is given below.

Chapter 1 gives an overview of the magnetoelectric effect and magnetoelectric materials. Magnetoelectric multilayered heterostructure based on AlN and FSMA thin films are studied. The chapter also provides essential information to understand the magnetoelectric coupling mechanism and its application in MEMS based Magnetic Sensors.

Chapter 2 presents the details of the experimental techniques employed for the synthesis and characterization of Magnetoelectric heterostructure and its layers. All thin film samples were fabricated using reactive DC magnetron sputtering technique. Various characterization techniques, such as X-rays diffraction (XRD), X-ray photoelectronic spectra (XPS), atomic force microscopy (AFM) and field emission scanning electron microscopy (FESEM), vibrating sample microscopy (VSM), and double beam laser interferometry have been discussed in details. Electrical properties of the samples were studied using Keithley 4200 semiconductor characterization system (SCS), 4294 Impedance analyzer and Vector Network Analyzer (VNA). Also, a magnetic setup attached to VNA was used to measure the frequency response of Magnetoelectric coupling based bulk acoustic wave (BAW) resonator.

Chapter 3 describes the growth assessment and scrutinize dielectric reliability of c-axis oriented insulating AlN thin films in MIM structures for microelectronics applications. The effect of bottom electrodes (Al, Pt & Ti) on the texture, piezoelectric characteristics, dielectric properties and leakage current of AlN thin films have been systematically studied. X-ray diffraction results revealed that the lattice structure and texture of the bottom electrode play a vital role in c-axis wurtzite phase growth of AlN thin films. A highly (002) oriented c-axis AlN thin film was obtained over Ti as compared to Al and Pt electrodes. The piezoelectric coefficient (d_{33eff}) of these fabricated AlN thin films were measured by piezoresponse force microscopy to evaluate their piezoelectric efficiency in resonators. AlN is a good option for passivation purpose in microelectronic devices because of high chemical stability and excellent dielectric properties. Therefore, the dielectric reliability of AlN thin films is very crucial. Among all structures, AlN/Ti structure exhibits the highest dielectric constant (ε_r)~8.63 at 1 MHz. This work also provided a comprehensive study of leakage current conduction mechanism with an electric field. The leakage behavior depicts that all AlN film endures a transition from ohmic conduction (E < 70 kV/cm) to Space charge limited current conduction (E > 70 kV/cm). Besides, the breakdown characteristics of these fabricated films were also studied for deciding the long-term device reliability and life. This study suggests that the electrode engineering of AlN thin films has potential in electrical devices applications.

Chapter 4 is divided into two sections. **Section 4.1** explores the presence of strong magnetoelectric (ME) coupling in a sputtered deposited NiMnIn/AlN heterostructure on a Si substrate. The X-ray diffraction, scanning electron microscopy, and X-ray photoelectron spectroscopy results confirm the formation of a pure AlN wurtzite phase in the ME heterostructure. The magnetization vs temperature measurement shows the presence of the martensite transformation region of the NiMnIn/AlN heterostructure. The magnetic measurements exhibit the room temperature ferromagnetic nature of the NiMnIn/AlN heterostructure. The NiMnIn/AlN ME heterostructure was found to have a high ME coupling coefficient of 99.2 V/cm Oe at H_{dc} ~300 Oe. The induced ME coupling coefficient shows a linear dependency on Hac up to 8 Oe. In **Section 4.2**, a lead-free ME composite of NiMnIn (180 nm) / AlN (180 nm) / NiMnIn (50 nm) / AlN (180 nm) / NiMnIn (180 nm) structure has been fabricated using magnetron sputtering. The AlN structure with encapsulated NiMnIn layer exhibits higher dielectric permittivity, piezoelectric response and magnetodielectric response as compared to pure AlN (~360 nm) structure. The dielectric constant of the encapsulated structure was found to be about 300 % (22.3) more as compared to that of pure AlN (~ 7.24) structure. The piezoelectric coefficient of the multilayered structure was found to be about 7.49. A high value (~1268 ppm) of the magnetostriction coefficient was obtained for ferromagnetic NiMnIn layer using cantilever deflection method. The magnetic field sensing characteristics of the fabricated encapsulated structure is studied in term of magneto-dielectric effect as large as 8.5%. Such proposed multilayered structures with enhanced dielectric constant and excellent magnetodielectric characteristics are useful for futuristic magnetic field sensing and MEMS based devices applications.

Chapter 5 shows the realization of a magnetic field tunable piezo-resonator. A comprehensive analysis of the influence of the magnetic field on BAW resonator consisting of a highly magnetostrictive layer and AlN thin film is systematically studied. The fundamental resonant frequency of the fabricated BAW resonator is about ~4.22 GHz. In the presence of a magnetic field, we studied the effect on the resonator parameters such as resonant frequency, acoustic velocity, and coupling coefficient. For the magnetic field of strength 1200 Oe, the resonant frequency significantly shifts by ~360 MHz. Resonant frequency increases and electromechanical coupling coefficient (k_t) decreases with the increase in the DC magnetic field. The maximum acoustic velocity of ~7350 m/sec was observed at the magnetic field of 1500 Oe when applied parallel to the surface. Agilent Advanced Design Software (ADS) was used to extract the equivalent Modified Butterworth-Van Dyke circuit parameters (R_m, C_m, and L_m) of the resonator. Further, in the presence of the magnetic field, we obtained the variation in values of R_m, C_m, and L_m of the resonator structure. Such tunable resonators can be useful and vital in dealing with varying frequency bands for sustainable growth in wireless communication and magnetic field sensor applications.

Chapter 6 describes major conclusions drawn after thorough discussion and in-depth analysis presented in individual chapters. A brief report on the scope for future work is also included.

ACKNOWLEDGEMENTS

Though the following research work presented in this thesis is an individual work, but I could never have reached this milestone in my life without the support and guidance of many people.

Firstly, I want to thanks my supervisor Dr. Davinder Kaur, Professor, Institute for her motivation, ideas, moral support, willingness to support her knowledge and experience and a keen interest in research. The joy and enthusiasm, she has for his research were contagious and motivational for me, even during tough times in the Ph.D. pursuit. Without her guidance and constant feedback, this PhD would not have been achievable.

I would also like to express my sincere thanks to Prof. R. K. Dutta, Head of the Centre and all other faculty members of Centre for Nanotechnology for their support. I am also thankful to my research committee members, Dr. S. K. Nath (Chairman CRC, Centre of Nanotechnology), Dr. Brijesh Kumar Kaushik (External expert, Dept. of Electronics and Communication Engineering), Dr. P. Jeevanandam (Internal expert, Dept. of Chemistry), IIT Roorkee, for their valuable suggestions and estimation of the progress of my thesis.

I am also grateful to Prof. Ramesh Chandra, who has always been very generous and forthcoming in allowing me to run equipment at the Institute Instrumentation Center (IIC), IIT Roorkee. His cheerful disposition has always been a great source of inspiration and encouragement.

It is my pleasure to acknowledge the advice and love receive from my senior researchers in the lab: Dr. Kirandeep Singh, Dr. Narendra Singh, Dr. Ravi Prakash and Dr. Rahul Barman. I want to thank Mr. Anuj Kumar and Mr. Pradeep Kumar for their utmost care in both my academic and personal matters. I much enjoyed working with my lab mates Shubham, Krishan, Pankaj, Bhanu, Gagan, Diksha and Sushma for all the help they have extended. We had valuable research discussions and enjoyed parties and entertainment. It was a phenomenal experience with Dr. Ashwani Kumar, Dr. Satyendra Kumar, Dr. Gaurav Malik, Rinku Choudhary, Ravikant and Aditya at IIC, IIT Roorkee. The group has been a source of friendships as well as sound advice and collaboration.

I will be failing my emotion if I do not mention the name of my wife, Arooshi Mogha, who has always been a great source of motivation and her continuous support, patience and understanding in many ways cannot be expressed in words. I express my heartfelt gratitude to my adorable parents, for their unconditional love, encouragement and blessing.

I also thank people who were not part of my research group but helped me out, including, Dr. Sanjay Saini, Dr Ankit Dev and Dr. Narendra Patel, and a special thanks to Dr. Adtiya Khatri for his incredible works in daily life.

The financial support provided by the Ministry of Human Resource and Development (MHRD); Govt. of India is gratefully acknowledged.

Finally, let me thank the almighty God, who has given me courage, strength, wisdom, and memorable moments of my life. I will keep on trusting you for my future. Thank you, Lord.

(Shuvam Pawar)

List of Figures

List of Tables

List of Publications

Paper published in referred International Journals

1 Magnetic field tunable Ferromagnetic Shape Memory Alloy based Piezo-Resonator
Shuvam Pawar, Jitendra Singh, Davinder Kaur
IEEE Electron Device Letter **41** (2), pp-280 (2020)

2 High magnetoelectric coupling in Si-integrated AlN/NiMnIn thin film double layers at room temperature.
Shuvam Pawar, Anuj Kumar, Kirandeep Singh, Davinder Kaur
Applied Physics Letters **113** (24), 242902 (2018)

3 Growth assessment and scrutinize dielectric reliability of c-axis oriented insulating AlN thin films in MIM structures for microelectronics applications.
Shuvam Pawar, Kirandeep Singh, Shubham Sharma, Akhilesh Pandey, Shankar Dutta, Davinder Kaur
Materials Chemistry and Physics **219**, 74 (2018).

4 Enhanced Magneto-Dielectric response in c-axis AlN based magnetoelectric multilayer encapsulating highly magnetostrictive thin film.
Shuvam Pawar, Anuj Kumar, Kirandeep Singh, Davinder Kaur
IEEE/TMS Journal of electronic materials **49**, 8, (2020)

5 Strain-Induced Dielectric Enhancement in AlN-Based Multiferroic Layered Structure
Shuvam Pawar, Anuj Kumar, Davinder Kaur
Shape Memory and Superelasticity **6**, 24 (2020)

6 Bipolar resistive switching behavior in MoS_2 nanosheets fabricated on ferromagnetic shape memory alloy.
Anuj Kumar, **Shuvam Pawar**, Shubham Sharma, Davinder Kaur
Applied Physics Letters 112 (26), 262106 (2018).

7 Anisotropic magnetoelectric functionality of FSMAs heterostructures for MEMS magnetic sensors
Anuj Kumar, **Shuvam Pawar**, Davinder Kaur
Journal of Applied Physics: D Applied Physics, **53**, 39 (2020)


भारतीय प्रौद्योगिकी संस्थान रुड़की
INDIAN INSTITUTE OF TECHNOLOGY ROORKEE

Paper presented in International Conferences

1 Optimizing strain mediated magnetoelectric coupling in NiMnIn/AlN layered heterostructure

Shuvam Pawar, Anuj Kumar, Davinder Kaur

IEEE ICEE 2018 held at IISC Bangalore, India from 16th – 19th Dec, 2018

"**Best Poster award**".

2 Dielectric enhancement of AlN based multiferroic heterostructures via insertion of NiMnIn thin layer between AlN films.

Shuvam Pawar, Anuj Kumar, Davinder Kaur

IEEE-INEC 2019 held at Kuching, Malaysia.

3 Strain-Induced Dielectric Enhancement in AlN-Based Multiferroic Layered Structure

Shuvam Pawar, Anuj Kumar, Davinder Kaur

ICFSMA 2019 held at Prague.

4 Growth temperature modulated phase evolution and functional characteristics of high quality $Pb_{1-x}La_x(Zr_{0.9}Ti_{0.1})O_3$ thin films

Anuj Kumar, **Shuvam Pawar**, Kirandeep Singh, Davinder Kaur

2nd International Conference on Condensed Matter and Applied Physics (ICC 2017) held at Bikaner, India from November 24-25, 2017.


भारतीय प्रौद्योगिकी संस्थान रुड़की
INDIAN INSTITUTE OF TECHNOLOGY ROORKEE

CONTENTS

1. INTRODUCTION

2. SYNTHESIS AND CHARACTERIZATION

3. GROWTH ASSESSMENT OF ALN THIN FILMS

4. ME COUPLING RESPONSE IN AlN/FSMA HETEROSTRUCTURES

5. MAGNETIC FIELD TUNABLE AlN PIEZO-RESONATOR

6. CONCLUSIONS AND FUTURE PROSPECTS

Chapter 1

Introduction


भारतीय प्रौद्योगिकी संस्थान रुड़की
INDIAN INSTITUTE OF TECHNOLOGY ROORKEE

CHAPTER 1

INTRODUCTION


भारतीय प्रौद्योगिकी संस्थान रुड़की
INDIAN INSTITUTE OF TECHNOLOGY ROORKEE

1.1. Magnetoelectric effect

The magnetoelectric (ME) effect is the interaction between the magnetic field and the electric field in a matter. ME effect is the induction of electric polarization on applying the magnetic field and induction of magnetization on the application of the electric field **[1-4]**. The ME effect is used in a wide range of modern science and technology such as novel memory devices, wave modulators, optical diodes, amplifiers, tunable resonators, sensors **[5-11]**. For the first time, in the year 1888, Rontgen observed magnetization in a dipole moving in the presence of the electric field **[12]**. Later, in 1926, Debye referred to this phenomenon as a ME effect. Fox and Scott showed that ferroelectricity could produce magnetic order and vice versa **[13-15]**. These findings had triggered an interest in the study and understanding of 'ME' materials. ME coupling in ME materials can exist independently of the electric and magnetic nature **[16]**. It may be a direct result of product interaction of polarization (magnetization) and magnetic field (electric field) or indirect as a result of a combination of few order parameters coupled via strain, exchange bias or mediated charges [17-24]. There are two types of ME coupling in layered composite systems: i) Direct ME coupling and ii) Converse ME coupling [**25, 26**]. In direct ME coupling, when an external magnetic field (H) is applied to the composite, it results in the mechanical deformation of the ferromagnetic phase. As the ferromagnetic material is coupled to the piezoelectric phase, there is a variation induced electric field (E) in the piezoelectric phase due to the piezoelectric effect. The ME voltage coefficient, $(\alpha_E = \partial E/\partial H)$ gives the strength of direct ME interaction. The Direct ME coupling finds its applications in areas related to magnetic sensors, current sensors, energy harvesting devices, and tunable resonators **[27-29]**. In the case of converse ME interaction, the application of an electric field gives rise to strain-induced magnetization and can be measured using M vs E data or electric field tuning of ferromagnetic resonance. The Converse ME coupling finds its uses in spintronics, MERAM, voltage tunable filters/resonators **[30-35]**.

1.2. Magnetoelectric materials

Magnetoelectric materials have covered a long journey in terms of their material constituents and dimensions. They have progressed from single phase compounds to particulate composites, laminated composites and, lastly to nano/micro-thin films **(figure 1.1) [36]**. The single-phase ME materials have been immensely studied in the 20th century after the discovery of first bulk single multiferroic material ($Ni_2B_7O_{13}I$). Researchers are continuously working to explore possible methods or techniques to obtain efficient coupling of electric and magnetic ordering in the single-phase material system **[37, 38]**. But these materials are not suitable for practical room temperature application as the ME coupling interaction of these materials dramatically drops to zero around room temperature (above transition temperature) **[39-41]**.

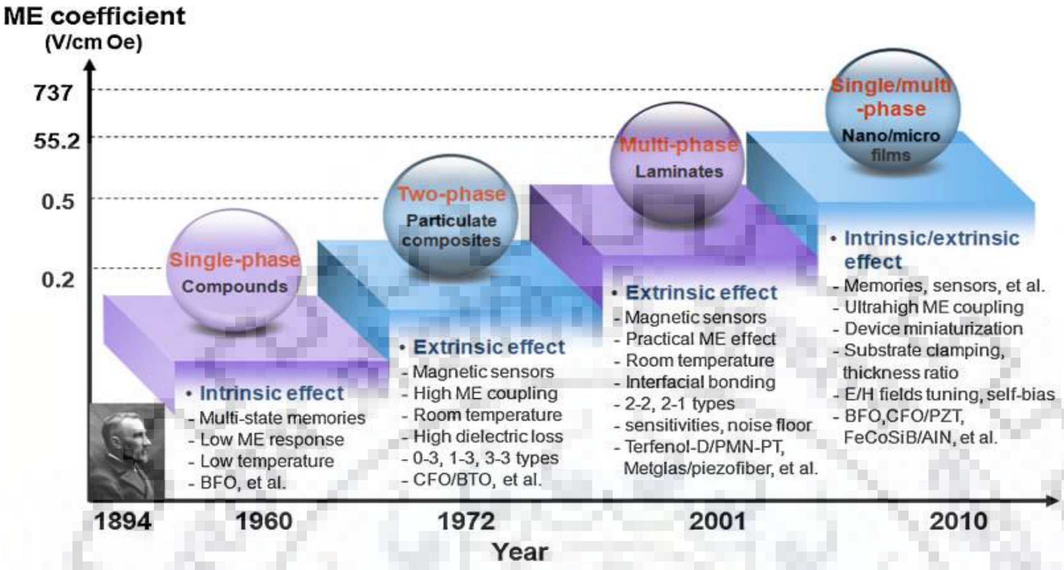

Figure 1.1 Evolution of Magnetoelectric materials.

In 1972, Van Suchtelen *et al.* facilitated the appearance of particulate ferroelectric/ferromagnetic two-phase ME composites. He proposed a product effect of combining both piezoelectric and piezomagnetic materials such as $Pb(Zr_{0.56}Ti_{0.44})O_3$-$Ni_{0.6}Zn_{0.2}Cu_{0.2}Fe_2O_4$ and $BaTiO_3$-$CoFe_2O_3$ **[42]**. These particulates were synthesized by co-sintering at elevated temperatures. The issue associated with these types of composites were high leakage current due to low resistivity of magnetic particle and non-ideal strain transfer at the interface of the two phases **[43]**. At the beginning of the 21st century, particulate composites have opened a window to achieve high ME coupling performance at room temperature. Thus, the realization of strong coupling is getting attention **[44, 45]**. New techniques such as using a mixture of piezoelectric powders and magnetic ferrites at high temperature, multilayered configurations, such as bulk sandwiched structure of piezomagnetic material (Ni, FeCoSiB, FeGa, Trefenol-D or Ni-Mn-X) with an embedded piezoelectric phase (PZT, PMN-PT, AlN or ZnO) and bi-layered structure of ferromagnetic and piezoelectric thin films (FeGaB/AlN, NiMnIn/PZT, etc.) to suppress the leakage current, retain individual material properties of each phase and to improve the interfacial strain transfer process [**46-55**]. Advanced material fabrication techniques such as pulsed laser deposition, chemical vapour deposition, molecular beam epitaxy, and sputtering have accelerated the research on Ferromagnetic and piezoelectric nanostructured thin films **[56]**.

The ME coupling in layered magnetoelectric materials is a product tensor property, resulted from the combination of two phases, i.e. ferromagnetic and piezoelectric of the composite [**42, 57**]. The coupling mechanism takes place at the interface of the piezoelectric and ferromagnetic materials. The ME composite thin films have attracted enormous attention because different phases can be attached and designed at the atomic level with higher precision, providing a more in-depth insight into the fundamental mechanisms of ME coupling. Furthermore, nanostructured thin film composites are required from the perspective of future devices and engineering applications [**58**].

Many efforts have been made to achieve strong ME coupling in layered structures, especially the control through strain mediated coupling, while another two ways of modulation are spin exchange and charge carrier. Among these, the strain mediated effect has been widely investigated and is the main route to realize both types of ME coupling, while the research on the remaining two mechanisms is in the early stage **[59-62]**. The strength of the ME coupling depends on many factors, such as interface quality, high anisotropy magnetostriction, lattice mismatching, and functional characteristics of the individual piezoelectric and magnetostrictive layers [**63**].

Since ME coupling in layered structure takes place at the interface of a piezoelectric and magnetostrictive layer. Therefore, the ME coupling is expected to increase with the increment of the contact area. The architecture of the composite is a crucial factor in deciding the overall ME coupling of the composite structure **[64-66]**. Also, ME coupling in two phases piezoelectric/ magnetostrictive composite would transduce a magnetic signal directly to voltage. The two phases are stress coupled in such composite, thus producing the desired ME signal. The zero-order magnitude of ME susceptibility, α, is given by:

$$\alpha = \frac{\partial P}{\partial H} = \frac{\partial P}{\partial \sigma} \times \frac{\partial \sigma}{\partial \lambda_M} \times \frac{\partial \lambda_M}{\partial H} \tag{1.1}$$

Where, $\partial\lambda_M/\partial H$ describes the magnetostrictive susceptibility; $\partial\sigma/\partial\lambda_M$ is the transduction of magnetostrictive strain to the stress, σ, in the piezoelectric material and $\partial P/\partial\sigma$ is the piezoelectric effect in the piezoelectric phase. These three partial derivatives are known as the piezomagnetic coefficient, the coupling coefficient, and the piezoelectric coefficient, respectively **[67, 68]**. Since the ME response in the case of two-phase composite depends on the piezoelectric, magnetostrictive layer, and coupling between them. Thus, the selection of appropriate magnetostrictive and piezoelectric materials (with high piezomagnetic and piezoelectric coefficients and strong coupling) is the primary step toward achieving strong ME coupling. In succeeding sections, the magnetostrictive and piezoelectric layers are discussed.

Furthermore, the heterostructure based on a combination of best suited magnetostrictive and piezoelectric material is also studied.

1.2.1. Piezoelectric Materials

Piezoelectric materials exhibit a direct transduction property to convert a mechanical signal to electric domains and vice versa. The generation of charge (voltage) on the application of stress is known as the direct piezoelectric effect, on the other hand, the production of mechanical stress upon the application of an electric field is known as the converse piezoelectric effect. During these effects, there is a deviation in the center of the inversion symmetry of the crystal structure **[69]**. The deviation is accompanied by a variation in charge distribution on the atoms and bonds within the crystal changes. This distribution develops a net electrical polarization across the crystal on the application of stress.

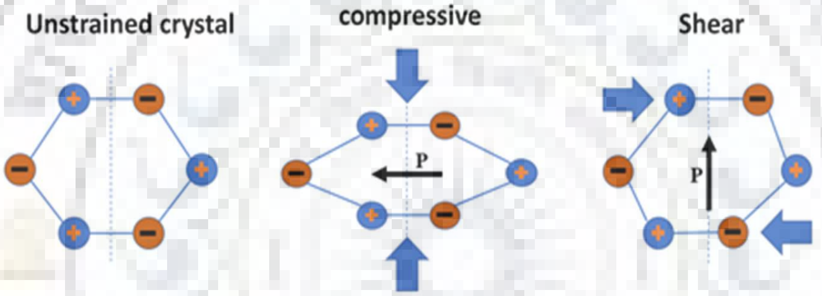

Figure 1. 2 Schematic illustration of the piezoelectric effect. Compressive or shear stress leads to dipole formations.

Under the free or unstrained state, the ions within the crystal are arranged in such a way that the net charge dipole is zero. When the piezoelectric materials are exposed to mechanical deformation (compressive or tensile), the ions having opposite charges get displaced to each other. This displacement produces a non-zero dipole, and subsequently, an electrical polarization in the crystal is developed [**fig 1.2**].

With the increasing demand for performance and miniaturization of devices, a considerable amount of research is being pursued in piezoelectric thin films for electronic and micro-electro-mechanical system applications. The most commonly used piezoelectric thin films are Lead Zirconate Titanate (PZT), Zinc Oxide (ZnO), and aluminum nitride (AlN), etc. **[70]**.

The application of these materials depends on the knowledge of their piezoelectric parameters and required applications. PZT has the highest piezoelectric strain coefficient (d_{33}) and electromechanical coupling coefficient (k) which makes it one of the most promising piezoelectric material. However, its toxic nature, it cannot be implemented in the complementary metal-oxide-semiconductor (CMOS) fabrication industry **[71]**.

Table 1.1 Comparison of ZnO, PZT and AlN

Property	**PZT**	**ZnO**	**AlN**
D₃₃	High	Moderate	Low
D₃₁	High	Moderate	Low
Resistance	High	High	High
Constant	High	High	Low
RF losses	High	Moderate	Low
Sound velocity	Slow	Slow	High
Thermal Expansion coefficient	High	High	Low
GHz capability	High	Poor	Good
Ferroelectricity	Yes	Yes	No
Environment	Unfriendly	--	Friendly
Density	High	--	Low
CMOS compatible	Not	Not fully	Fully

Both AlN and ZnO have similar piezoelectric properties, but the performance of ZnO degrades with the increase in temperature due to its low curie temperature. AlN is a material with several applications in electronics, MEMS, optoelectronic devices due to its outstanding electrical, mechanical, optical, and chemical properties combined with high acoustic velocity **[72]**. **Table 1.1** summarizes the properties of PZT, AlN, and ZnO **[73]**. Among the above discussed piezoelectric materials, AlN has gained much interest due to its CMOS compatibility and high-frequency applications.

Aluminum Nitride

Aluminum Nitride (AlN) thin films have attracted a large number of researchers worldwide because of its excellent properties such as high thermal conductivity, chemical stability, a wide bandgap (6.2 eV), and a higher acoustic velocity **[74, 75]**. The combination of these chemical and physical properties has increased the interest of AlN in thin films and bulk form for practical applications. Its applications are not limited to surface passivation of insulators and/or semiconductors, but also to surface/bulk acoustic wave devices, acousto-optic (AO) devices, and optical devices in an ultraviolet spectral region **[76, 77]**. The properties of AlN are summarized in **table 1.2 [78, 79]**.

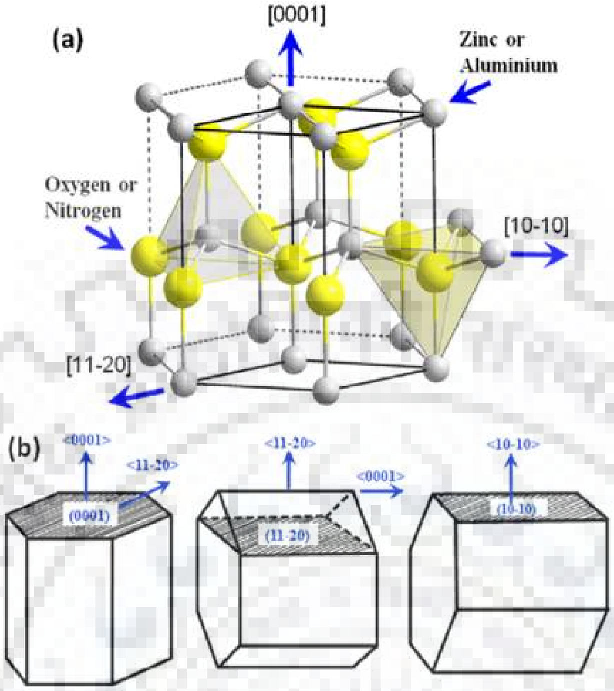

Figure 1.3 Aluminium Nitride (AlN) crystal structure.

Aluminum nitride film exhibits piezoelectric properties and therefore finds its application in the fabrication of transducer, bulk, and surface acoustic waves devices, etc. Aluminum Nitride (AlN) thin films have two different structures, namely wurtzite and Zinc blende. The wurtzite hexagonal closed packed (hcp) aluminum nitride exhibits a higher piezoelectric coefficient as compared to the zinc blende structure **[80]**. Material properties greatly influence the efficiency of piezoelectric mems devices such as gyroscopes, resonators, accelerometers, etc.

Crystal structure, c-axis orientation, defects in AlN thin films strongly affects the dielectric and piezoelectric properties of AlN thin films. Hence, c-direction oriented AlN thin film having the dominant piezoresponse can play a crucial role in increasing the overall efficiency of the piezoelectric based devices (**figure 1.3**) **[81]**.

Aluminum Nitride (AlN) can be configured either as sensors or actuators for transducer applications. For sensors, the device is made to have a maximum electric signal as an output, in response to mechanical input. On the other hand, for the transducer, a device is designed to generate maximum stress or strain in response to an applied electric field using the converse piezoelectric effect. Therefore, a large piezoelectric coefficient (d_{33}) and large piezoelectric voltage coefficient (e_{33}) are required for actuator and sensor applications, respectively **[82]**.

Table 1.2 Properties of Aluminium Nitride (AlN)

Properties	Value
Chemical Formula	AlN
Molar Mass	40.989 g/mol
Electron Mobility	~300 cm^2/V. s
Crystal Structure	Wurtzite
Lattice constant *a*	3.112 A
Lattice constant *c*	4.982 A
Density	3.3 g/cm^3
Band gap	6.2 eV
Thermal expansion co-efficient	4.6 x 10^{-6} /C
Thermal conductivity	2.0 W/cm. K
Critical field strength (E_c)	6-15 MV/cm
Relative index *n*	2.15
Acoustic Velocity	6000~10000 m/s
Melting Point	> 2000 C

1.2.2. Magnetostrictive Materials

Magnetostrictive materials are the class of smart materials that can convert energy between magnetic and elastic states **[83]**. This bidirectional nature of energy exchange in magnetostrictive can find its application in both actuation and sensing. The magnetostrictive materials and the devices fabricated using these materials are often referred to as a transducer. The magnetostrictive phase in a ME composite can be characterized into single element metals, alloys, and ceramics as summarized in **table 1.3 [84-89]**.

Although $CoFe_2O_4$ and $NiFe_2O_4$ are known soft magnetic materials. Metglas (highest permeability) and Terfenol-D (with giant magnetostriction) are widely used magnetostrictive alloys because of their high piezomagnetic coefficient. Most of the transducer applications require maximum movements as output. Therefore, a significant value of magnetostriction plays a vital role in the overall response of ferromagnetic alloys-based sensors. Therefore, there is a new class of materials known as a ferromagnetic shape memory alloy (FSMA), having a large stain as compared to existing magnetostrictive materials is studied **[90]**.

Table 1.3 Classification of magnetostrictive materials for ME composites.

Piezomagnetic Materials		**λ (ppm)**	μ_r
Single element metals	Fe	-7	5000
	Co	31	250
	Ni	-33	100-600
Alloys	Metglas	40	40000
	FeGaB thin films	70	400
	Permalloy	27	2700
	Trefnol-D	2000	10
	NiMn-X (In, Sb)	10000	400-600
Ceramics	Fe_3O_4	40	40
	$NiFe_2O_4$	-26	44
	$CoFe_2O_4$	-160-300	20

Note λ denotes magnetostriction and μ_r denotes relative permeability

Ferromagnetic Shape Memory Alloy

Ferromagnetic shape memory alloy (FSMA) is a subcategory of shape memory alloy (SMA), which shows a shape memory effect in the presence of a magnetic field (**figure 1.4**). FSMA exhibits fast and remote actuation or sensing with a magnetic field, in addition to large strain capability of SMA. Therefore, FSMA can play a vital role in novel applications and demonstrate a new mechanism for conversion between magnetic and mechanical energies **[91-94]**.

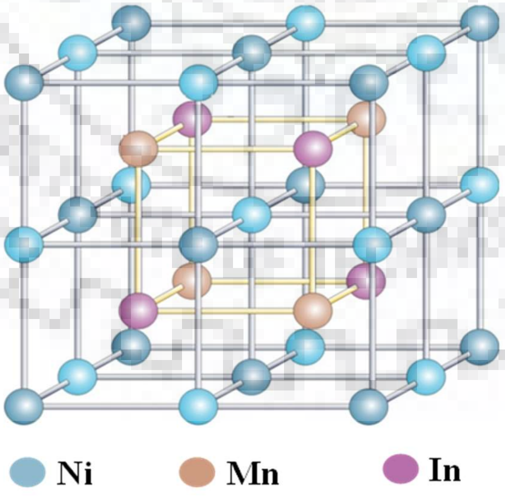

Figure 1.4 Crystal structure of ferromagnetic shape memory alloy (NiMnIn).

FSMA alloys show large output strain and very short reaction time, thus making them a promising candidate for practical applications in intelligent micro electro mechanical systems (MEMS) such as sensors and actuators **[95]**.

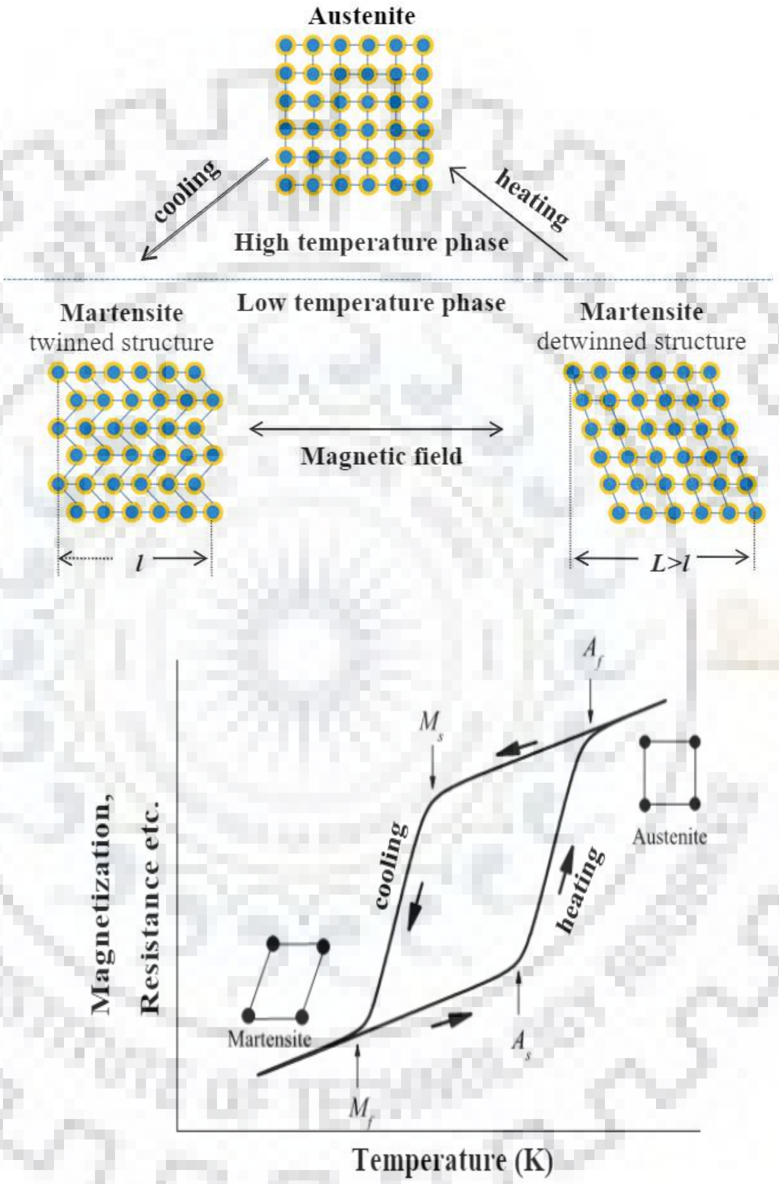

Figure 1.5 Effect of magnetic field and temperature on the ferromagnetic shape memory alloy.

The magnetic response of shape memory alloy was first observed in Ni_2MnGa by Ullakko with a strain of 0.2%. These results led to the advancement in the field of ferromagnetic with improved deformation strain of about 10%. The high cost of Ga-based alloy and their low melting point led to considerable interest in Ni-Mn-X (X= In, Sn, Sb) based alloy. Recently, Ni-Mn-X

(X= In, Sn, Sb) have gained much attention due to their favorable properties such as large magnetic field induced strain, large magnetoresistance (MR), hall effect, large magnetocaloric effect (MCE) and reversible distortion. These properties make them a strong candidate for the creation of new devices such as magnetic sensors, actuators, and coolant for magnetic refrigeration **[96-99]**. The reason for large strain in ferromagnetic shape memory alloy is the distortion in the structure during martensite transformation experienced by these materials (**figure 1.5**) **[100, 101]**.

Hernado et al. studied the magneto structural properties of NiMnIn and NiMnSn alloy. He found that these alloys are monophase and exhibits ferromagnetic $L2_1$ austenite at high temperature and get transformed to martensite with structure 10M, 14M, or $L1_0$ type **[102]**. Although many results have been reported on the bulk NiMnIn alloys, the number of potential applications can be extended to multiple folds by extrapolating its properties in thin films **[103]**. Various ways to deposit thin films were undertaken, such as pulsed laser deposition (PLD), molecular beam epitaxy (MBE), sputtering, and flash-evaporation of alloy powders. Among these, sputtering has gained high importance due to large area deposition and the use of non-toxic gases. For emerging micro-devices such as MEMS sensors, high quality of NiMnIn thin film technology is developed intensively **[104]**.

1.2.3. Piezoelectric/magnetostrictive heterostructures.

There was a sudden upsurge in the research of ME composite in the early 2000s. Srinivasan et al. reported the highest room temperature ME coupling coefficient in a few hundreds of mV/cm at room temperature for 2-2 type laminate ceramic composites. ME bulk composite comprising of Terfenol-D ($Tb_{1-x}Dy_xFe_2$) created a landmark in the growth of bulk ME composites Terfenol-D is a rare earth iron alloy with giant magnetostriction **[105-107]**. With the advancement in thin film fabrication technology, a variety of nanostructured composite thin films of piezoelectric and magnetostrictive are vigorously studied in the past few years **[108, 109]**.

Nanostructured thin films provide more degree of freedom like interlayer interaction or lattice strain for an alteration in ME response. It provides the opportunity to the researchers to investigate the cause of ME effect at the nanoscale. Zheng et al. in 2014 reported a study of BTO/STO based nanostructured films as the first fruitful work **[110]**. The commonly studied layered ME along with their ME response, are summarized in **table 1.4**.

Table 1.4 Magnetoelectric heterostructure thin films

ME Composites		***References***
Magnetostrictive Phase	***Piezoelectric phase***	
$BiFeO_3$	$BaTiO_3$	**[111]**
LSMO	PZT	**[112-114]**
Fe	$BiTiO_3$	**[115]**
NiFe	$BiTiO_3$	**[116]**
$Ni_{0.65}Zn_{0.35}Fe_2O_4$	$Pb(Fe_{0.5}Nb_{0.5})O_3$	**[117]**
$CoFe_2O_4$	$Bi_4Ti_3O_{12}$	**[118]**
NiMnIn	$Pb(Zr_{0.52}Ti_{0.48})O_3$	**[119]**
Ni	$Pb(Zr_{0.52}Ti_{0.48})O_3$	**[120]**
Ni	$Pb(Zr_{0.52}Ti_{0.48})O_3$	**[121]**
Metglas	$Pb(Zr, Ti)O_3$	**[122]**
Metglas	Strontium titanate	**[123]**

The strength of magnetodielectric coupling in these structures depends on factors such as interface quality, morphology, and functional properties of individual layers. Therefore, these layered structures require attention for their use in futuristic magnetic field devices such as tunable microwave devices like filters, resonators, phase shifters, sensitive sensors, and energy harvesters.

1.3. MEMS based Acoustic Wave Resonators

Microelectromechanical system or MEMS have emerged as an ultramodern tool to design, manufacture, and package the futuristic devices. The MEMS based devices find its application in sensors, biotechnology, defense, consumer products, environmental protection and safety, telecommunication, aerospace, and automotive industry **[124, 125]**.

MEMS is a transducer, which converts mechanical energy to electrical energy and vice versa. The fundamental advantage of MEMS /NEMS over existing technologies is its ultra-low noise performance and its high sensitivity to external agitations **[126]**. It consists of two prime components, (a) sensing element or actuating element and (b) signal transduction unit. The **figure 1.6** shows the building block of MEMS as a sensor **[127]**.

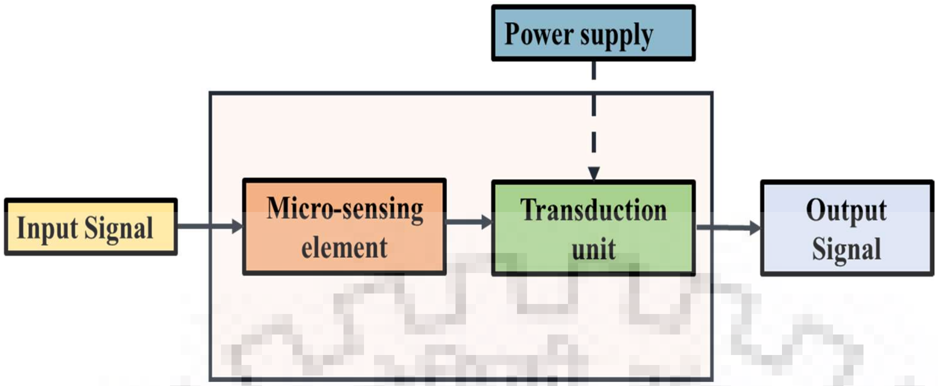

Figure 1.6 MEMs as a microsensor

There have been many advancements in micro-machined sensors and actuators area to meet the ever-growing demand. Still, there is a need to integrate new materials in existing MEMS technologies apart from silicon or silicon-based compounds **[128]**. To bridge this gap, piezoelectric materials have found in its application with more possibilities and crucial than ever. Piezoelectric materials properties can be tailored or altered by scaling or through the process of miniaturization to bring huge interest **[129]**.

MEMS technology makes use of manufacturing techniques preferred in integrated circuit (IC) foundries to design and fabricate miniature electronic and mechanical systems. The advantage of using IC fabrication processes in acoustic wave resonators is that the resonators can be mass-produced with low cost, portability, and low power consumption **[130]**. Acoustic wave-based MEMS device is a promising technique for a broad range of applications due to their capability to operate wirelessly and high selectivity. These devices make use of acoustic waves on the surface or bulk of a piezoelectric material. Any direct or indirect variation in the characteristic properties in the piezoelectric material or the propagation path affects the amplitude or velocity of the acoustic wave **[131]**.

The MEMS fabrication of acoustic wave sensors enables the integration of Acoustic waves devices with electronics circuits. The compatibility of the piezoelectric layer and its fabrication process is crucial for the realization and designing of advanced multifunctional devices **[132]**. Depending on the propagation of the acoustic waves, the acoustic wave resonators can be broadly classified into two categories.

a) Surface Acoustic Wave resonator:

The acoustic wave in surface acoustic resonator propagates along the surface of the piezoelectric/active layer, in a mixed longitudinal-shear Rayleigh mode **[133]**. The active layer for SAW devices could be the carrying substrate itself, and the excitation is applied with the help of inter-digital electrodes (IDT) located on the top of the piezoelectric and within the same plane **(fig 1.7)**.

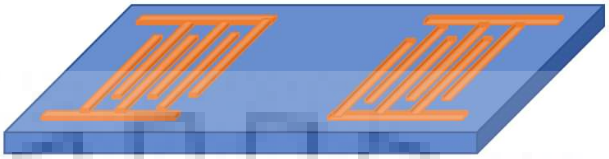

Figure 1.7 Schematic of Surface Acoustic Wave resonators

b). Bulk Acoustic Wave resonator.

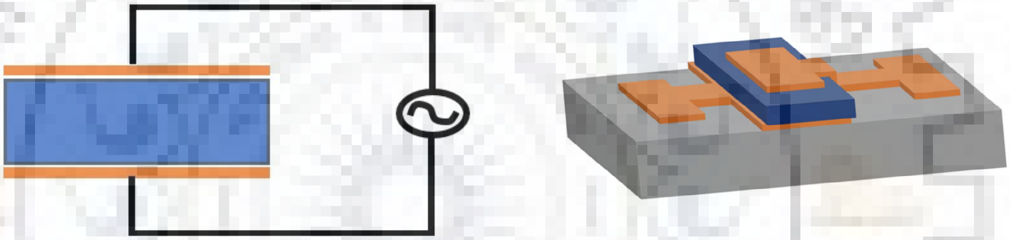

Figure 1.8 Schematic of Bulk Acoustic Wave resonator

Bulk acoustic wave resonators are the MEMS devices in which the acoustic wave propagates through the bulk of its active layer, and the excitation electrode is across the piezoelectric layer **(figure 1.8)**. It is fabricated using a thin layer of piezoelectric material with metal electrodes on both sides. The acoustic wave propagates unguided through the volume of the piezoelectric layer **[134]**.

1.4. Motivation of the thesis

With the advancement in technology, research is being focused on new materials that could meet the requirement for MEMS devices in terms of CMOS compatibility, work efficiency, fabrication process and cost effective. There is an urgent need to propose a novel ME composite that can perform at low power, offer new functionalities and can be actuated by various external independent variables. As discussed in the previous sections, several ME structures have been reported by the researchers with an improved ME response at room temperature. Still, there is a requirement of ME material with CMOS compatible piezoelectric and high magnetostrictive thin film.

For reliable ME composite, there is a need of functional magnetic materials having large magnetostriction, high electrical conductivity which diminishes the requirement of a separate bottom electrode. Ferromagnetic Shape Memory Alloys (FSMAs) are a new class of multifunctional magnetic materials with a great potential to overcome the limitations as mentioned earlier for ME applications. They exhibit intrinsically large magnetostriction which can be tuned by temperature, magnetic field or stress. Among different, piezoelectric materials available, AlN has been considered as it offers many advantages that were discussed in the beginning.

Driven by these opportunities, the initial motive of my PhD work was to fabricate layered ME structure with combining thin films of CMOS compatible aluminum nitride (AlN) and high magnetostrictive ferromagnetic shape memory alloy (FSMA). The work also includes characterization of fabricated AlN/FSMA structure for MEMS application.

MEMS based thin film bulk acoustic wave resonator (FBAR) has established as a reliable option in the field of filters, sensors and wireless devices. FBAR devices are based on a stack of multiple thin film layers. Each layer has a specific function to make it operative or to improve its characteristic response. The final motive of my thesis to realize a tunable piezo-resonator based on the optimized AlN/FSMA heterostructure. The realized tunable resonator can play a crucial role in sustainable growth in wireless communication and magnetic field sensor application. In the present work, we have performed the following:

- Growth assessment and scrutinize dielectric reliability of c-axis oriented insulating AlN thin films in MIM structures for microelectronics applications.
- High magnetoelectric coupling in Si-integrated AlN/NiMnIn thin film double layers at room temperature.
- Enhanced Magneto-Dielectric response in c-axis AlN based magnetoelectric multilayer encapsulating highly magnetostrictive thin film.
- Design and fabrication of Magnetic field tunable Ferromagnetic Shape Memory Alloy based Piezo-Resonator

1.5. REFERENCES

[1]. Fiebig, M., 2005. Revival of the magnetoelectric effect. Journal of physics D: applied physics, 38(8), p.R123.

[2]. Ryan, P.J., Kim, J.W., Birol, T., Thompson, P., Lee, J.H., Ke, X., Normile, P.S., Karapetrova, E., Schiffer, P., Brown, S.D. and Fennie, C.J., 2013. Reversible control of magnetic interactions by electric field in a single-phase material. Nature communications, 4(1), pp.1-8.

[3]. Smolenskii, G.A. and Chupis, I.E., 1982. Segnetomagnetics. Uspekhi Fizicheskikh Nauk, 137(3), pp.415-448.

[4]. Buurma, A.J.C., Blake, G.R., Palstra, T.T.M. and Adem, U., 2016. Multiferroic materials: physics and properties.

[5]. Scott, J.F., 2012. Applications of magnetoelectrics. Journal of Materials Chemistry, 22(11), pp.4567-4574.

[6]. Bibes, M. and Barthélémy, A., 2008. Towards a magnetoelectric memory. Nature materials, 7(6), pp.425-426.

[7]. Quindeau, A., Fina, I., Marti, X., Apachitei, G., Ferrer, P., Nicklin, C., Pippel, E., Hesse, D. and Alexe, M., 2015. Four-state ferroelectric spin-valve. Scientific reports, 5, p.9749.

[8]. Pantel, D., Goetze, S., Hesse, D. and Alexe, M., 2012. Reversible electrical switching of spin polarization in multiferroic tunnel junctions. Nature materials, 11(4), pp.289-293.

[9]. Balinskiy, M., Chavez, A.C., Barra, A., Chiang, H., Carman, G.P. and Khitun, A., 2018. Magnetoelectric spin wave modulator based on synthetic multiferroic structure. Scientific reports, 8(1), pp.1-10.

[10]. Wei, C.M., Shih, H.Y., Chen, Y.F. and Lin, T.Y., 2011. Optical detection of magnetoelectric effect in the composite consisting of InGaN/GaN multiple quantum wells and FeCo thin film. Applied Physics Letters, 98(13), p.131913.

[11]. Kiser, J., Finkel, P., Gao, J., Dolabdjian, C., Li, J. and Viehland, D., 2013. Stress reconfigurable tunable magnetoelectric resonators as magnetic sensors. Applied Physics Letters, 102(4), p.042909.

[12]. Röntgen, W.C., 1888. Ueber die durch Bewegung eines im homogenen electrischen Felde befindlichen Dielectricums hervorgerufene electrodynamische Kraft. Annalen der Physik, 271(10), pp.264-270.

[13]. Curie, P., 1894. On symmetry in physical phenomena, symmetry of an electric field and of a magnetic field. J. Phys, 3, pp.395-415.

[14]. Debye, P., 1926. Comment on some new experiments on a magneto-electrical directional effect. Journal of Physics, 36 (4), pp.300-301.

[15]. Fiebig, M., 2005. Revival of the magnetoelectric effect. Journal of physics D: applied physics, 38(8), p.R123.

[16]. To be searched

[17]. Vaz, C.A., Hoffman, J., Ahn, C.H. and Ramesh, R., 2010. Magnetoelectric coupling effects in multiferroic complex oxide composite structures. Advanced Materials, 22(26-27), pp.2900-2918.

[18]. Vaz, C.A.F. and Staub, U., 2013. Artificial multiferroic heterostructures. Journal of Materials Chemistry C, 1(41), pp.6731-6742.

[19]. Vaz, C.A., 2012. Electric field control of magnetism in multiferroic heterostructures. Journal of Physics: Condensed Matter, 24(33), p.333201.

[20]. Ramesh, R. and Spaldin, N.A., 2007. Multiferroics: progress and prospects in thin films. Nature materials, 6(1), pp.21-29.

[21]. Hochstrat, A., Binek, C., Chen, X. and Kleemann, W., 2004. Extrinsic control of the exchange bias. Journal of magnetism and magnetic materials, 272, pp.325-326.

[22]. Molegraaf, H.J., Hoffman, J., Vaz, C.A., Gariglio, S., Van Der Marel, D., Ahn, C.H. and Triscone, J.M., 2009. Magnetoelectric effects in complex oxides with competing ground states. Advanced Materials, 21(34), pp.3470-3474.

[23]. Kambale, R.C., Jeong, D.Y. and Ryu, J., 2012. Current status of magnetoelectric composite thin/thick films. Advances in Condensed Matter Physics, 2012.

[24]. Nan, C.W., 1994. Magnetoelectric effect in composites of piezoelectric and piezomagnetic phases. Physical Review B, 50(9), p.6082.

[25]. Nan, C.W., Bichurin, M.I., Dong, S.X., Viehland, D. and Srinivasan, G., 2008. Magnetoelectric multiferroic composites. J. Appl. Phys, 103, p.031101.

[26]. Palneedi, H., Annapureddy, V., Priya, S. and Ryu, J., 2016, March. Status and perspectives of multiferroic magnetoelectric composite materials and applications. In Actuators (Vol. 5, No. 1, p. 9). Multidisciplinary Digital Publishing Institute.

[27]. Dong, S., Cheng, J., Li, J.F. and Viehland, D., 2003. Enhanced magnetoelectric effects in laminate composites of Terfenol-D/Pb (Zr, Ti) O 3 under resonant drive. Applied Physics Letters, 83(23), pp.4812-4814.

[28]. Zhai, J., Xing, Z., Dong, S., Li, J. and Viehland, D., 2006. Detection of pico-Tesla magnetic fields using magneto-electric sensors at room temperature. Applied physics letters, 88(6), p.062510.

[29]. Dong, S., Zhai, J., Li, J.F., Viehland, D. and Priya, S., 2008. Multimodal system for harvesting magnetic and mechanical energy. Applied Physics Letters, 93(10), p.103511.

[30]. Chu, Y.H., Martin, L.W., Holcomb, M.B., Gajek, M., Han, S.J., He, Q., Balke, N., Yang, C.H., Lee, D., Hu, W. and Zhan, Q., 2008. Electric-field control of local ferromagnetism using a magnetoelectric multiferroic. Nature materials, 7(6), pp.478-482.

[31]. Heron, J.T., Trassin, M., Ashraf, K., Gajek, M., He, Q., Yang, S.Y., Nikonov, D.E., Chu, Y.H., Salahuddin, S. and Ramesh, R., 2011. Electric-field-induced magnetization reversal in a ferromagnet-multiferroic heterostructure. Physical review letters, 107(21), p.217202.

[32]. Hu, J.M., Li, Z., Chen, L.Q. and Nan, C.W., 2011. High-density magnetoresistive random access memory operating at ultralow voltage at room temperature. Nature communications, 2(1), pp.1-8.

[33]. Nan, T.X., Zhou, Z.Y., Lou, J., Liu, M., Yang, X., Gao, Y., Rand, S. and Sun, N.X., 2012. Voltage impulse induced bistable magnetization switching in multiferroic heterostructures. Applied Physics Letters, 100(13), p.132409.

[34]. Lou, J., Reed, D., Liu, M. and Sun, N.X., 2009. Electrostatically tunable magnetoelectric inductors with large inductance tunability. Applied Physics Letters, 94(11), p.112508.

[35]. Yang, G.M., Lou, J., Wu, J., Liu, M., Wen, G., Jin, Y. and Sun, N.X., 2011, June. Dual H-and E-field tunable multiferroic bandpass filters with yttrium iron garnet film. In 2011 IEEE MTT-S International Microwave Symposium (pp. 1-4). IEEE.

[36]. Wang, Y., Li, J. and Viehland, D., 2014. Magnetoelectrics for magnetic sensor applications: status, challenges and perspectives. Materials Today, 17(6), pp.269-275.

[37]. Ascher, E., Rieder, H., Schmid, H. and Stössel, H., 1966. Some properties of ferromagnetoelectric nickel-iodine boracite, Ni3B7O13I. Journal of Applied Physics, 37(3), pp.1404-1405.

[38]. Yan, Q.Y., Kim, T., Purkayastha, A., Xu, Y., Shima, M., Gambino, R.J. and Ramanath, G., 2006. Magnetic properties of Sb-doped FePt nanoparticles. Journal of applied physics, 99(8), p.08N709.

[39]. Ma, J., Hu, J., Li, Z. and Nan, C.W., 2011. Recent progress in multiferroic magnetoelectric composites: from bulk to thin films. Advanced materials, 23(9), pp.1062-1087.

[40]. Nan, C.W., Bichurin, M.I., Dong, S., Viehland, D. and Srinivasan, G., 2008. Multiferroic magnetoelectric composites: Historical perspective, status, and future directions. Journal of applied physics, 103(3), p.1.

[41]. Jin, J., Lu, S.G., Chanthad, C., Zhang, Q., Haque, M.A. and Wang, Q., 2011. Multiferroic polymer composites with greatly enhanced magnetoelectric effect under a low magnetic bias. Advanced Materials, 23(33), pp.3853-3858.

[42]. Van Suchtelen, J., 1972. Product properties: a new application of composite materials. Philips Res. Rep, 27(1), pp.28-37.

[43]. Priya, S., Islam, R., Dong, S. and Viehland, D., 2007. Recent advancements in magnetoelectric particulate and laminate composites. Journal of Electroceramics, 19(1), pp.149-166.

[44]. Ryu, J., Priya, S., Uchino, K. and Kim, H.E., 2002. Magnetoelectric effect in composites of magnetostrictive and piezoelectric materials. Journal of electroceramics, 8(2), pp.107-119.

[45]. Ryu, J., Carazo, A.V., Uchino, K. and Kim, H.E., 2001. Magnetoelectric properties in piezoelectric and magnetostrictive laminate composites. Japanese Journal of Applied Physics, 40(8R), p.4948.

[46]. Chu, Z., Shi, H., Shi, W., Liu, G., Wu, J., Yang, J. and Dong, S., 2017. Enhanced resonance magnetoelectric coupling in (1-1) connectivity composites. Advanced Materials, 29(19), p.1606022.

[47]. Liang, X., Dong, C., Celestin, S.J., Wang, X., Chen, H., Ziemer, K.S., Page, M., McConney, M.E., Jones, J.G., Howe, B.M. and Sun, N.X., 2018. Soft Magnetism, Magnetostriction, and Microwave Properties of Fe-Ga-C Alloy Films. IEEE Magnetics Letters, 10, pp.1-5.

[48]. Lou, J., Insignares, R.E., Cai, Z., Ziemer, K.S., Liu, M. and Sun, N.X., 2007. Soft magnetism, magnetostriction, and microwave properties of FeGaB thin films. Applied Physics Letters, 91(18), p.182504.

[49]. Li, D., Zheng, W., Zheng, D., Gong, J., Wang, L., Jin, C., Li, P. and Bai, H., 2016. Magnetization and resistance switchings induced by electric field in epitaxial Mn: ZnO/BiFeO3 multiferroic heterostructures at room temperature. ACS applied materials & interfaces, 8(6), pp.3977-3984.

[50]. Nan, T., Lin, H., Gao, Y., Matyushov, A., Yu, G., Chen, H., Sun, N., Wei, S., Wang, Z., Li, M. and Wang, X., 2017. Acoustically actuated ultra-compact NEMS magnetoelectric antennas. Nature communications, 8(1), pp.1-8.

[51]. Li, M., Matyushov, A., Dong, C., Chen, H., Lin, H., Nan, T., Qian, Z., Rinaldi, M., Lin, Y. and Sun, N.X., 2017. Ultra-sensitive NEMS magnetoelectric sensor for pico-tesla DC magnetic field detection. Applied Physics Letters, 110(14), p.143510.

[52]. Singh, K. and Kaur, D., 2017. Piezoelectric control of magnetoelectric coupling driven non-volatile memory switching and self-cooling effects in FE/FSMA multiferroic heterostructures. Journal of Applied Physics, 121(8), p.084104.

[53]. Singh, K. and Kaur, D., 2017. Room-temperature giant magneto-mechanical-electric cross-coupling in Si-integrated $PbZr_{0.52}Ti_{0.48}O_3/Ni_{50}Mn_{35}In_{15}$ multiferroic heterostructures. Journal of Physics D: Applied Physics, 50(14), p.145002.

[54]. Cui, J., 2014. Shape memory alloys and their applications in power generation and refrigeration. In Mesoscopic phenomena in multifunctional materials (pp. 289-307). Springer, Berlin, Heidelberg.

[55]. Kumar, A., Goswami, A., Singh, K., McGee, R., Thundat, T. and Kaur, D., 2019. Magnetoelectric Coupling in NiMnIn/PLZT Artificial Multiferroic Heterostructure and Its Application in Mid-IR Photothermal Modulation by External Magnetic Field. ACS Applied Electronic Materials, 1(11), pp.2226-2235.

[56]. Ma, J., Hu, J., Li, Z. and Nan, C.W., 2011. Recent progress in multiferroic magnetoelectric composites: from bulk to thin films. Advanced materials, 23(9), pp.1062-1087.

[57]. Ryu, J., Kang, J.E., Zhou, Y., Choi, S.Y., Yoon, W.H., Park, D.S., Choi, J.J., Hahn, B.D., Ahn, C.W., Kim, J.W. and Kim, Y.D., 2015. Ubiquitous magneto-mechano-electric generator. Energy & Environmental Science, 8(8), pp.2402-2408.

[58]. Chu, Z., PourhosseiniAsl, M. and Dong, S., 2018. Review of multi-layered magnetoelectric composite materials and devices applications. Journal of Physics D: Applied Physics, 51(24), p.243001.

[59]. Ma, J., Hu, J., Li, Z. and Nan, C.W., 2011. Recent progress in multiferroic magnetoelectric composites: from bulk to thin films. Advanced materials, 23(9), pp.1062-1087.

[60]. Sreenivasulu, G., Qu, P., Petrov, V., Qu, H. and Srinivasan, G., 2016. Sensitivity enhancement in magnetic sensors based on ferroelectric-bimorphs and multiferroic composites. Sensors, 16(2), p.262.

[61]. Gutiérrez, J., Lasheras, A., Martins, P., Pereira, N., Barandiarán, J.M. and Lanceros-Mendez, S., 2017. Metallic glass/PVDF magnetoelectric laminates for resonant sensors and actuators: A review. Sensors, 17(6), p.1251.

[62]. Annapureddy, V., Palneedi, H., Hwang, G.T., Peddigari, M., Jeong, D.Y., Yoon, W.H., Kim, K.H. and Ryu, J., 2017. Magnetic energy harvesting with magnetoelectrics: an emerging technology for self-powered autonomous systems. Sustainable Energy & Fuels, 1(10), pp.2039-2052.

[63]. Kimura, T., Tomioka, Y., Asamitsu, A. and Tokura, Y., 1998. Anisotropic magnetoelastic phenomena in layered manganite crystals: Implication of change in orbital state. Physical review letters, 81(26), p.5920.

[64]. Pal A, Shirodkar S N, Gohil S, Ghosh S, Waghmare U V. and Ayyub P 2013 Multiferroic behavior in elemental selenium below 40 K: Effect of electronic topology Sci. Rep. 3 1–7

[65]. Stognij, A., Novitskii, N., Sazanovich, A., Poddubnaya, N., Sharko, S., Mikhailov, V., Nizhankovski, V., Dyakonov, V. and Szymczak, H., 2013. Ion-beam sputtering deposition and magnetoelectric properties of layered heterostructures (FM/PZT/FM) n, where FM–Co or Ni 78 Fe 22. The European Physical Journal-Applied Physics, 63(2).

[66]. Zhai, J., Xing, Z., Dong, S., Li, J. and Viehland, D., 2008. Magnetoelectric laminate composites: an overview. Journal of the American Ceramic Society, 91(2), pp.351-358.

[67]. Van Den Boomgaard, J., Van Run, A.M.J.G. and Suchtelen, J.V., 1976. Magnetoelectricity in piezoelectric-magnetostrictive composites. Ferroelectrics, 10(1), pp.295-298.

[68]. Viehland, D., Wuttig, M., McCord, J. and Quandt, E., 2018. Magnetoelectric magnetic field sensors. MRS Bulletin, 43(11), pp.834-840.

[69]. Kholkin, A.L., Pertsev, N.A. and Goltsev, A.V., 2008. Piezoelectricity and crystal symmetry. In Piezoelectric and Acoustic Materials for Transducer Applications (pp. 17-38). Springer, Boston, MA.

[70]. Fraga, M.A., Furlan, H., Pessoa, R.S. and Massi, M., 2014. Wide bandgap semiconductor thin films for piezoelectric and piezoresistive MEMS sensors applied at high temperatures: an overview. Microsystem technologies, 20(1), pp.9-21.

[71]. Aksel, E. and Jones, J.L., 2010. Advances in lead-free piezoelectric materials for sensors and actuators. Sensors, 10(3), pp.1935-1954.

[72]. Iqbal, A. and Mohd-Yasin, F., 2018. Reactive sputtering of aluminum nitride (002) thin films for piezoelectric applications: A review. Sensors, 18(6), p.1797.

[73]. Al Ahmad, M. and Plana, R., 2009. Vertical displacement detection of an aluminum nitride piezoelectric thin film using capacitance measurements. International Journal of Microwave and Wireless Technologies, 1(1), pp.5-9.

[74]. Bu, G., Ciplys, D., Shur, M., Schowalter, L.J., Schujman, S. and Gaska, R., 2006. Surface acoustic wave velocity in single-crystal AlN substrates. ieee transactions on ultrasonics, ferroelectrics, and frequency control, 53(1), pp.251-254.

[75]. Lin, C.M., Chen, Y.Y., Felmetsger, V.V., Lien, W.C., Riekkinen, T., Senesky, D.G. and Pisano, A.P., 2013. Surface acoustic wave devices on AlN/3C–SiC/Si multilayer structures. Journal of Micromechanics and Microengineering, 23(2), p.025019.

[76]. Xiong, C., Pernice, W.H. and Tang, H.X., 2012. Low-loss, silicon integrated, aluminum nitride photonic circuits and their use for electro-optic signal processing. Nano letters, 12(7), pp.3562-3568.

[77]. Tadesse, S.A. and Li, M., 2014. Sub-optical wavelength acoustic wave modulation of integrated photonic resonators at microwave frequencies. Nature communications, 5, p.5402.

[78]. Fu, Y.Q., Luo, J.K., Nguyen, N.T., Walton, A.J., Flewitt, A.J., Zu, X.T., Li, Y., McHale, G., Matthews, A., Iborra, E. and Du, H., 2017. Advances in piezoelectric thin films for acoustic biosensors, acoustofluidics and lab-on-chip applications. Progress in Materials Science, 89, pp.31-91.

[79]. SULTAN, D., Characterization of GaN/AlN MQW based Heterostructures using Fourier Transform Infrared (FTIR) Spectroscopy.

[80]. Yang, R., Zhu, C., Wei, Q. and Du, Z., 2017. Phase stability, mechanical and optoelectronic properties of two novel phases of AlN. Modern Physics Letters B, 31(18), p.1750201.

[81]. Zhang, M., Yang, J., Si, C., Han, G., Zhao, Y. and Ning, J., 2015. Research on the piezoelectric properties of AlN thin films for MEMS applications. Micromachines, 6(9), pp.1236-1248.

[82]. Signore, M.A., Rescio, G., De Pascali, C., Iacovacci, V., Dario, P., Leone, A., Quaranta, F., Taurino, A., Siciliano, P. and Francioso, L., 2019. Fabrication and characterization of AlN-based flexible piezoelectric pressure sensor integrated into an implantable artificial pancreas. Scientific reports, 9(1), pp.1-11.

[83]. Santapuri, S., Scheidler, J.J. and Dapino, M.J., 2015. Two-dimensional dynamic model for composite laminates with embedded magnetostrictive materials. Composite Structures, 132, pp.737-745.

[84]. Kleemann, W., 2017. Multiferroic and magnetoelectric nanocomposites for data processing. Journal of Physics D: Applied Physics, 50(22), p.223001.

[85]. Lawes, G. and Srinivasan, G.J.P.D.A.P., 2011. Introduction to magnetoelectric coupling and multiferroic films. Journal of Physics D: Applied Physics, 44(24), p.243001.

[86]. Lanceros-Méndez, S. and Martins, P. eds., 2017. Magnetoelectric Polymer-based Composites: Fundamentals and Applications. John Wiley & Sons.

[87]. Fulay, P. and Lee, J.K., 2016. Electronic, magnetic, and optical materials. CRC press.

[88]. Engdahl, G. and Mayergoyz, I.D., 2000. Handbook of giant magnetostrictive materials (Vol. 107). San Diego: Academic press.

[89]. Khaja Mohaideen, K. and Joy, P.A., 2012. High magnetostriction and coupling coefficient for sintered cobalt ferrite derived from superparamagnetic nanoparticles. Applied Physics Letters, 101(7), p.072405.

[90]. Bachaga, T., Zhang, J., Khitouni, M. and Sunol, J.J., 2019. NiMn-based Heusler magnetic shape memory alloys: A review. The International Journal of Advanced Manufacturing Technology, 103(5-8), pp.2761-2772.

[91]. Nespoli, A., Besseghini, S., Pittaccio, S., Villa, E. and Viscuso, S., 2010. The high potential of shape memory alloys in developing miniature mechanical devices: A review on shape memory alloy mini-actuators. Sensors and Actuators A: Physical, 158(1), pp.149-160.

[92]. Faran, E. and Shilo, D., 2015. Ferromagnetic shape memory alloys—challenges, applications, and experimental characterization. Experimental Techniques.

[93]. Zhong, Z., Ma, S., Wang, D. and Du, Y., 2012. A review on the regulation of magnetic transitions and the related magnetocaloric properties in Ni-Mn-Co-Sn Alloys. Journal of Materials Science & Technology, 28(3), pp.193-199.

[94]. Wang, C., Meyer, J., Teichert, N., Auge, A., Rausch, E., Balke, B., Hütten, A., Fecher, G.H. and Felser, C., 2014. Heusler nanoparticles for spintronics and ferromagnetic shape memory alloys. Journal of Vacuum Science & Technology B, Nanotechnology and Microelectronics: Materials, Processing, Measurement, and Phenomena, 32(2), p.020802.

[95]. Krenke, T., Duman, E., Acet, M., Wassermann, E.F., Moya, X., Mañosa, L., Planes, A., Suard, E. and Ouladdiaf, B., 2007. Magnetic superelasticity and inverse magnetocaloric effect in Ni-Mn-In. Physical Review B, 75(10), p.104414.

[96]. Dubenko, I., Samanta, T., Pathak, A.K., Kazakov, A., Prudnikov, V., Stadler, S., Granovsky, A., Zhukov, A. and Ali, N., 2012. Magnetocaloric effect and multifunctional properties of Ni–Mn-based Heusler alloys. Journal of magnetism and magnetic materials, 324(21), pp.3530-3534.

[97]. Liu, E., Wang, W., Feng, L., Zhu, W., Li, G., Chen, J., Zhang, H., Wu, G., Jiang, C., Xu, H. and De Boer, F., 2012. Stable magnetostructural coupling with tunable magnetoresponsive effects in hexagonal ferromagnets. Nature communications, 3(1), pp.1-10.

[98]. Wu, G.H., Yu, C.H., Meng, L.Q., Chen, J.L., Yang, F.M., Qi, S.R., Zhan, W.S., Wang, Z., Zheng, Y.F. and Zhao, L.C., 1999. Giant magnetic-field-induced strains in Heusler alloy NiMnGa with modified composition. Applied Physics Letters, 75(19), pp.2990-2992.

[99]. Kainuma, R., Imano, Y., Ito, W., Sutou, Y., Morito, H., Okamoto, S., Kitakami, O., Oikawa, K., Fujita, A., Kanomata, T. and Ishida, K., 2006. Magnetic-field-induced shape recovery by reverse phase transformation. Nature, 439(7079), pp.957-960.

[100]. Khan, M., Dubenko, I., Stadler, S. and Ali, N., 2008. Magnetostructural phase transitions in $Ni_{50}Mn_{25+X}Sb_{25-X}$ Heusler alloys. Journal of Physics: Condensed Matter, 20(23), p.235204.

[101]. Sozinov, A., Likhachev, A.A., Lanska, N. and Ullakko, K., 2002. Giant magnetic-field-induced strain in NiMnGa seven-layered martensitic phase. Applied Physics Letters, 80(10), pp.1746-1748.

[102]. Hernando, B., Llamazares, J.S., Santos, J.D., Sánchez, M.L., Escoda, L., Suñol, J.J., Varga, R., García, C. and González, J., 2009. Grain oriented NiMnSn and NiMnIn Heusler alloys ribbons produced by melt spinning: Martensitic transformation and magnetic properties. Journal of Magnetism and Magnetic Materials, 321(7), pp.763-768.

[103]. Aksoy, S., 2015. Synthesis and characterization of NiMnIn nanoparticles. Journal of Magnetism and Magnetic Materials, 373, pp.236-239.

[104]. Maji, C., 2017. Properties of magnetic shape memory alloys in martensitic phase. CURRENT SCIENCE, 112(7), p.1390.

[105]. Srinivasan, G., Rasmussen, E.T., Gallegos, J., Srinivasan, R., Bokhan, Y.I. and Laletin, V.M., 2001. Magnetoelectric bilayer and multilayer structures of magnetostrictive and piezoelectric oxides. Physical Review B, 64(21), p.214408.

[106]. Ryu, J., Priya, S., Carazo, A.V., Uchino, K. and Kim, H.E., 2001. Effect of the Magnetostrictive Layer on Magnetoelectric Properties in Lead Zirconate Titanate/Terfenol-D Laminate Composites. Journal of the American Ceramic Society, 84(12), pp.2905-2908.

[107]. Sayed F N, Achary S N, Jayakumar O D, Deshpande S K, Krishna P S R, Chatterjee S, Ayyub P and Tyagi A K 2011 Role of annealing conditions on the ferromagnetic and dielectric properties of La_2NiMnO_6 J. Mater. Res. 26 567–77.

[108]. Wan, J.G., Liu, J.M., Chand, H.L.W., Choy, C.L., Wang, G.H. and Nan, C.W., 2003. Giant magnetoelectric effect of a hybrid of magnetostrictive and piezoelectric composites. Journal of applied physics, 93(12), pp.9916-9919.

[109]. Nan, C.W., Liu, L., Cai, N., Zhai, J., Ye, Y., Lin, Y.H., Dong, L.J. and Xiong, C.X., 2002. A three-phase magnetoelectric composite of piezoelectric ceramics, rare-earth iron alloys, and polymer. Applied Physics Letters, 81(20), pp.3831-3833.

[110]. Zheng, H., Wang, J., Lofland, S.E., Ma, Z., Mohaddes-Ardabili, L., Zhao, T., Salamanca-Riba, L., Shinde, S.R., Ogale, S.B., Bai, F. and Viehland, D., 2004. Multiferroic batio3-cofe2o4 nanostructures. Science, 303(5658), pp.661-663.

[111]. Gupta, R., Chaudhary, S. and Kotnala, R.K., 2015. Interfacial charge induced magnetoelectric coupling at BiFeO3/BaTiO3 bilayer interface. ACS applied materials & interfaces, 7(16), pp.8472-8479.

[112]. Dussan, S., Kumar, A., Scott, J.F. and Katiyar, R.S., 2010. Magnetic effects on dielectric and polarization behavior of multiferroic heterostructures. Applied Physics Letters, 96(7), p.072904.

[113]. Dussan, S., Kumar, A., Scott, J.F., Priya, S. and Katiyar, R.S., 2010. Room temperature multiferroic effects in superlattice nanocapacitors. Applied Physics Letters, 97(25), p.252902.

[114]. Dussan, S., Kumar, A., Katiyar, R.S., Priya, S. and Scott, J.F., 2011. Magnetic control of ferroelectric interfaces. Journal of Physics: condensed matter, 23(20), p.202203.

[115]. Venkataiah, G., Shirahata, Y., Suzuki, I., Itoh, M. and Taniyama, T., 2012. Strain-induced reversible and irreversible magnetization switching in Fe/BaTiO3 heterostructures. Journal of Applied Physics, 111(3), p.033921.

[116]. Li, Z., Hu, J., Shu, L., Zhang, Y., Gao, Y., Shen, Y., Lin, Y. and Nan, C.W., 2011. A simple method for direct observation of the converse magnetoelectric effect in magnetic/ferroelectric composite thin films.

[117]. Chakraborty, S., Mandal, S.K. and Saha, B., 2019. Optically tunable magnetoelectric properties of inorganic-organic multiferroic flexible film. Journal of Applied Physics, 125(20), p.204102.

[118]. Viehland, D., Wuttig, M., McCord, J. and Quandt, E., 2018. Magnetoelectric magnetic field sensors. MRS Bulletin, 43(11), pp.834-840.

[119]. Singh, K. and Kaur, D., 2015. Direct and converse magneto-electric coupling in ferromagnetic shape memory alloys based thin film multiferroic heterostructures. Applied Physics Letters, 107(26), p.262901.

[120]. Feng, M., Wang, J.J., Hu, J.M., Wang, J., Ma, J., Li, H.B., Shen, Y., Lin, Y.H., Chen, L.Q. and Nan, C.W., 2015. Optimizing direct magnetoelectric coupling in Pb (Zr, Ti) O3/Ni multiferroic film heterostructures. Applied Physics Letters, 106(7), p.072901.

[121]. Palneedi, H., Yeo, H.G., Hwang, G.T., Annapureddy, V., Kim, J.W., Choi, J.J., Trolier-McKinstry, S. and Ryu, J., 2017. A flexible, high-performance magnetoelectric heterostructure of (001) oriented pb (zr0. 52ti0. 48) o3 film grown on ni foil. APL Materials, 5(9), p.096111.

[122]. Palneedi, H., Maurya, D., Kim, G.Y., Annapureddy, V., Noh, M.S., Kang, C.Y., Kim, J.W., Choi, J.J., Choi, S.Y., Chung, S.Y. and Kang, S.J.L., 2017. Unleashing the full potential of magnetoelectric coupling in film heterostructures. Advanced Materials, 29(10), p.1605688.

[123]. Vivek, S., Geetha, P., Saravanan, V., Kumar, A.S., Lekha, C.C., Sudheendran, K., Anantharaman, M.R. and Nair, S.S., 2019. Magnetoelectric coupling in strained strontium titanate and Metglas based magnetoelectric trilayer. Journal of Alloys and Compounds, 789, pp.1056-1061.

[124]. Wu, G., Datar, R.H., Hansen, K.M., Thundat, T., Cote, R.J. and Majumdar, A., 2001. Bioassay of prostate-specific antigen (PSA) using microcantilevers. Nature biotechnology, 19(9), pp.856-860.

[125]. Nihtianov, S. and Luque, A. eds., 2018. Smart sensors and MEMS: intelligent sensing devices and microsystems for industrial applications. Woodhead Publishing.

[126]. Hui, Y. and Rinaldi, M., 2013. Fast and high-resolution thermal detector based on an aluminum nitride piezoelectric microelectromechanical resonator with an integrated suspended heat absorbing element. Applied Physics Letters, 102(9), p.093501.

[127]. Kumar, A. and Sekhar, B.M.A., 2017. Shape optimization of microcantilever beam used as biosensors using resonance frequency shift method. Indian J. Sci. Res, 15(2), pp.123-127.

[128]. Larin, A., Womble, P.C. and Dobrokhotov, V., 2018. Novel highly-integrated mems based solid state detectors for analytical gas chromatography. Sensors and Actuators B: Chemical, 256, pp.1057-1068.

[129]. Marino, A., Genchi, G.G., Mattoli, V. and Ciofani, G., 2017. Piezoelectric nanotransducers: The future of neural stimulation. Nano Today, 14, pp.9-12.

[130]. Sbrockey, N.M., Kalkur, T.S., Mansour, A., Khassaf, H., Yu, H., Aindow, M., Alpay, S.P. and Tompa, G.S., 2016. Switchable and tunable film bulk acoustic resonator fabricated using barium strontium titanate active layer and Ta_2O_5/SiO_2 acoustic reflector. Applied Physics Letters, 109(5), p.052902.

[131]. Dey, N., Ashour, A.S., Mohamed, W.S. and Nguyen, N.G., 2019. Acoustic wave technology. In Acoustic sensors for biomedical applications (pp. 21-31). Springer, Cham.

[132]. Hansen, K.M., Ji, H.F., Wu, G., Datar, R., Cote, R., Majumdar, A. and Thundat, T., 2001. Cantilever-based optical deflection assay for discrimination of DNA single-nucleotide mismatches. Analytical Chemistry, 73(7), pp.1567-1571.

[133]. Nikolaou, I., Hallil, H., Tamarin, O., Dejous, C. and Rebière, D., 2016, August. A three-dimensional model for a graphene guided SH-SAW sensor using finite element method. In 2016 31st Symposium on Microelectronics Technology and Devices (SBMicro) (pp. 1-4). IEEE.

[134]. Rocha-Gaso, M.I., March-Iborra, C., Montoya-Baides, Á. and Arnau-Vives, A., 2009. Surface generated acoustic wave biosensors for the detection of pathogens: A review. Sensors, 9(7), pp.5740-5769.

Chapter 2

Synthesis and Characterization


भारतीय प्रौद्योगिकी संस्थान रुड़की
INDIAN INSTITUTE OF TECHNOLOGY ROORKEE

CHAPTER 2

SYNTHESIS AND CHARACTERIZATION

2.1. Synthesis of thin films
  2.1.1. Magnetron sputtering technique
2.2. Basic structural characterization techniques
  2.2.1. X-ray Diffraction
  2.2.2. Field emission scanning electron microscopy
  2.2.3. Energy dispersive X-ray spectroscopy
  2.2.4. Atomic force microscopy
2.3. Electrical, mechanical and magnetic measurement techniques
  2.3.1. Piezo force microscopy (PFM)
  2.3.2. Semiconductor Characterization System (SCS-4200)
  2.3.3. Agilent Impedance Analyzer (4294A)
  2.3.4. Vector Network Analyzer (VNA)
  2.3.5. Vibrating Sample Magnetometer (VSM)
2.4. References

This chapter deals with the synthesis and characterization techniques employed for the fabrication of AlN/FSMA thin films structures. One specific technique, i.e. sputtering, has been used for the fabrication of AlN and FSMA thin films. The synthesized thin films were analysed by a variety of experimental techniques in terms of their structural, morphological, and electronic properties. Additionally, the fabricated heterostructures were used for applications such as tuneable resonator and magnetic sensors. In conclusion, this chapter provides the detailed processes of the synthesis and characterizations of the thin films used in the present thesis.

2.1. Synthesis of thin films

Thin film is one of the most researched areas in applications such as sensors, nanotechnology, solar, defence, aviation, photovoltaics, resistors, energy harvesters, semiconductor devices and space science technologies **[1,2]**. It is defined as a layer of materials extending in thickness from the nano-meter (monolayer) to few micro-meters, having a high surface to volume ratio. Synthesis of thin films is a process of deposition a thin film onto a substrate and is usually referred to as a thin film deposition process. Formation of the thin film is a diffusion process which starts with nucleation followed by coalescence and growth whereby various deposition parameters can alter all states. Usually, thin films growth depends strongly on the surface energy of both fabricated material as well as the underlying substrate **[3]**.

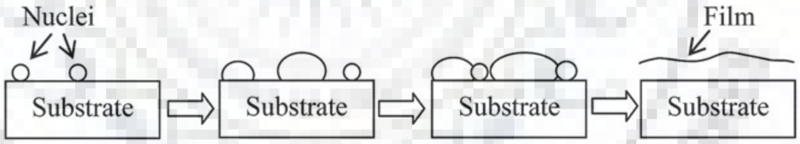

Figure 2.1. Thin film growth mechanism

Nucleation and accumulation processes of thin films depend upon the nature of the substrate. In the nucleation process, atoms or ions transfer its kinetic energy partially or fully to the substrate for adsorption onto the surface of the substrate via either Vander-Waals or covalent forces **[4-6]**. However, the condition for the adsorption of atoms is that the residual kinetic energy of these adsorbed atoms should be higher than the binding forces. Only at this stated condition, the atoms get diffused onto the surface of the substrate. During this process, the diffused atoms keep moving around on the surface depending upon the loss of energy or come across a state where the binding effects are robust to pin them down. Moreover, the mobility of the diffused atoms may occur for longer time (several seconds) depending on their surface energy. But some common regions are also existing there, where these diffused adatoms will bound generally, i.e. the surface defects such as grain boundaries, surface impurities or step edges. After that, these bounded adatoms starts the binding of other diffusing adatoms for the nucleation of grains, resulting in the formation of crystallites or grains. The interface of two grains are called grain boundaries, and the number of grain boundaries depends upon the size and shape of the grains, which can be determined by the distance between parent nucleation sites. The physical, electrical and other properties depend on the deposition parameters, microstructure and the substrate materials **[7]**. There are three growth modes of the thin film which depend on the interfacial energy and the surface energies of substrate and adsorbate.

- **Layer by layer growth mode:**

Stronger adatom-substrate interaction promotes layer by layer formations to render atomically smooth surface. This kind of growth is 2D growth, indicating the fabrication of complete film before the growth of successive layers. The growth of thin film specifically requires lattice-match between the substrate and the depositing material and hence considered as an ideal mechanism for thin film growth **[4]**.

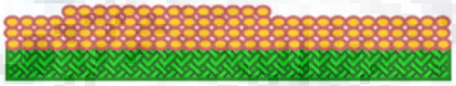

Figure 2.2. Layer-by -layer growth

- **Island growth mode:**

If the adatom-adatom interaction is stronger than that of adatom-substrate interaction, the formation of three-dimensional adatom clusters or island is promoted. The initial layers of atoms of the depositing material lead to the growth of islands like structures which are centred on the nucleation sites, which remain separated during the deposition **[4].**

Figure 2.3 Island growth

- **Layer-plus-Island growth mode:**

In layer-plus-island growth mode, initially, the adsorbate-surface interactions are much stronger than interactions between adsorbates. This mode of growth involves two major steps: In the first step, the adsorbate forms a complete film with a thickness of several monolayers grown by layer by layer growth mode on the substrate. In the second step, after reaching an optimum thickness, which depends on the strain and chemical potential of the thin film, the growth persists by following the island growth mode. This transformation takes place at a vital layer thickness which significantly depends on the characteristics of the film and substrate such as lattice constants and surface energy **[4].**

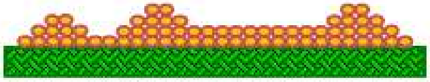

Figure 2.4 Layer-plus-Island growth

The adhesion quality of thin films is dependent on the substrate or underlying layer, which confirms the reliability of the thin film. It also depends significantly on the cleanliness of the substrate surface and also gets affected with optimum substrate roughness, because a very smooth substrate can also decrease the adhesion tendency of the grown films. The properties and quality of the films are influenced by the purity of material to be deposited, substrate nature, deposition temperature, deposition rate, and deposition technique. Thin film deposition must be performed in a controlled manner under extremely clean conditions for a smooth transfer of particles from the source to the substrate. In the synthesis of thin films, generally, two methods are used; chemical vapour deposition (CVD) and physical vapour deposition (PVD). PVD employs thermodynamic means to grow a thin film of high quality and includes magnetron sputtering **[8-11]**, pulsed laser deposition (PLD) **[12-14]**, thermal evaporation **[15],** molecular beam epitaxy (MBE) **[16]** etc. In CVD, the reaction or decomposition of volatile precursors on the surface of the substrate produces thin films, and it includes spray pyrolysis **[17, 18]**, sol-gel **[19, 20]**, chemical solution deposition **[21, 22],** photo-CVD **[23]** metal-organic chemical vapour deposition (MOCVD) **[24]** etc. Each synthesis technique has its plus and minus factors, and the choice of an appropriate technique is highly application and material specific.

Physical vapor deposition is highly effective for uniform thin films with moderate size distribution. The synthesis in PVD techniques is usually carried out by the same material whose film is to be synthesized, so the starting material purity decides the purity of the thin film. Physical vapour deposition techniques such as the laser ablation, sputtering and evaporation transfer of material atoms from one or more sources to the substrate surface in the form of a thin layer. In the case of evaporation deposition technique, it is isn't easy to maintain a constant rate of evaporation for all the materials. The issue with the plasma laser deposition (PLD) is its incapability in large area deposition. Among various physical deposition techniques, sputtering is in demand due to its simplicity, reliability and capability of usage in large area manufacturing for industrial productions. Further, the sputtering process makes it possible to synthesize nanocrystalline thin films with new physical and functional properties. Sputtering as deposition technique exhibits several advantages such as:

i. The operational conditions are steady and readily controllable.
ii. Thickness is controllable.
iii. Easy synthesis of high melting points and high reactive materials.
iv. The high flexibility of morphology
v. Desired complex geometry and roughness
vi. High uniformity at large area
vii. Good adhesion
viii. Better reproducibility.
ix. Large area manufacturing for commercialization

In the present work, DC magnetron sputtering has been employed to fabricate the Ferromagnetic shape memory alloy (NiMnIn) and Aluminum Nitride (AlN) thin films and their multiferroic heterostructures.

2.1.1. Magnetron Sputtering Technique

Magnetron Sputtering is a plasma-based PVD deposition technique. Magnetron sputtering has been an extensively used technique for the erosion of the surfaces and fabricating a variety of industrially important thin films and coatings [**25, 26**].

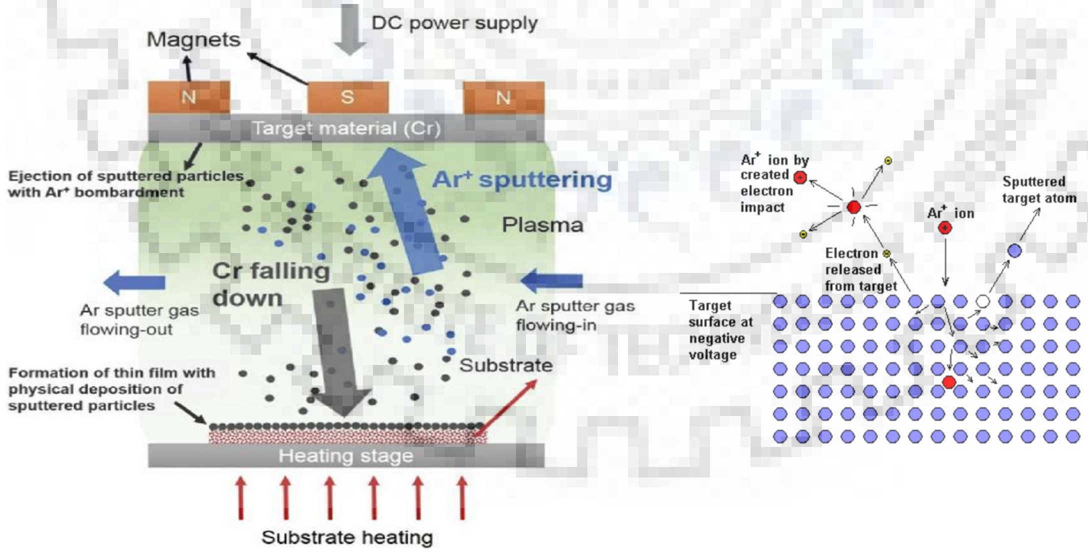

Figure 2.5 (a) Principal of magnetron sputtering **[27]**, (b): Sputtering at molecular level **[28]**.

The bombardment of the target material with energetic ions causes the removal of atoms from the target, which may then condense on a substrate leading thin film formation, as shown in **figure 2.5 (a)**. At the molecular level, fundamental particles involved in plasma during magnetron sputtering process are depicted in **figure 2.5 (b)**. Plasma is ignited by the inert gas fed into the chamber during the sputtering process. It is generated when secondary electrons, produced by the collision of positive ions with the target atoms, collide and ionize the inert gas atoms. The initial positive ions which are needed to trigger the generation of secondary electrons are thought to be either the stray ions always present in the atmosphere or the ions produced by field ionization of the inert gas atoms.

Secondary electrons originating from the target material in consequence of the ion bombardment helps in maintaining the continuous plasma. Magnets used in the sputtering process configure the magnetic field parallel to the target surface such that, it can constrain the motion of secondary electrons to the neighbourhood of the target. This trapping of electrons in an annular region near to the surface of the target extensively upsurges the possibility of ionizing inert gas atoms. The increased ionization efficiency leads to a cascade of electron-atom interaction resulting in dense plasma in front of the target. This accelerated process gives rise to enhance ion bombardment of the target surface resulting in higher sputtering rates and, consequently, elevated deposition rates at the substrate. The sputtering technique is broadly classified into three types:

i. DC Magnetron Sputtering: In DC sputtering, a DC voltage is applied to the target material. It is preferably used to sputter conducting targets.

ii. RF Magnetron Sputtering: In RF sputtering, an AC-voltage (13.56 MHz radio-frequency) is applied to the target for non-conducting and semiconductor targets. AC voltage is used because, in the case of insulators, the conduction bands do not allow free charge movement. As ions strike the target surface, their charge remains localized, and over the time it builds up, making it impossible to further bombard the surface and sputter process stops. AC voltage can be used to prevent the charge accumulation as ions are accelerated towards the surface of the target in one phase and charge neutrality is achieved in another phase.

iii. Reactive Sputtering: Reactive sputtering is used to deposit oxides and nitrides thin films. In reactive sputtering, a chemical interaction between the target material and gasses like nitrogen, oxygen or argon takes place. Nitride films can be produced by reactive sputtering in the presence of argon and nitrogen. With a combination of oxygen and argon, the oxides can also be deposited. The reaction usually occurs either on the substrate surface or on the target itself. In the present work, FSMA films, i.e. NiMnIn films were deposited using DC magnetron sputtering in a pure argon plasma while the piezoelectric film, i.e. AlN film, were prepared by reactive sputtering in a nitrogen environment.

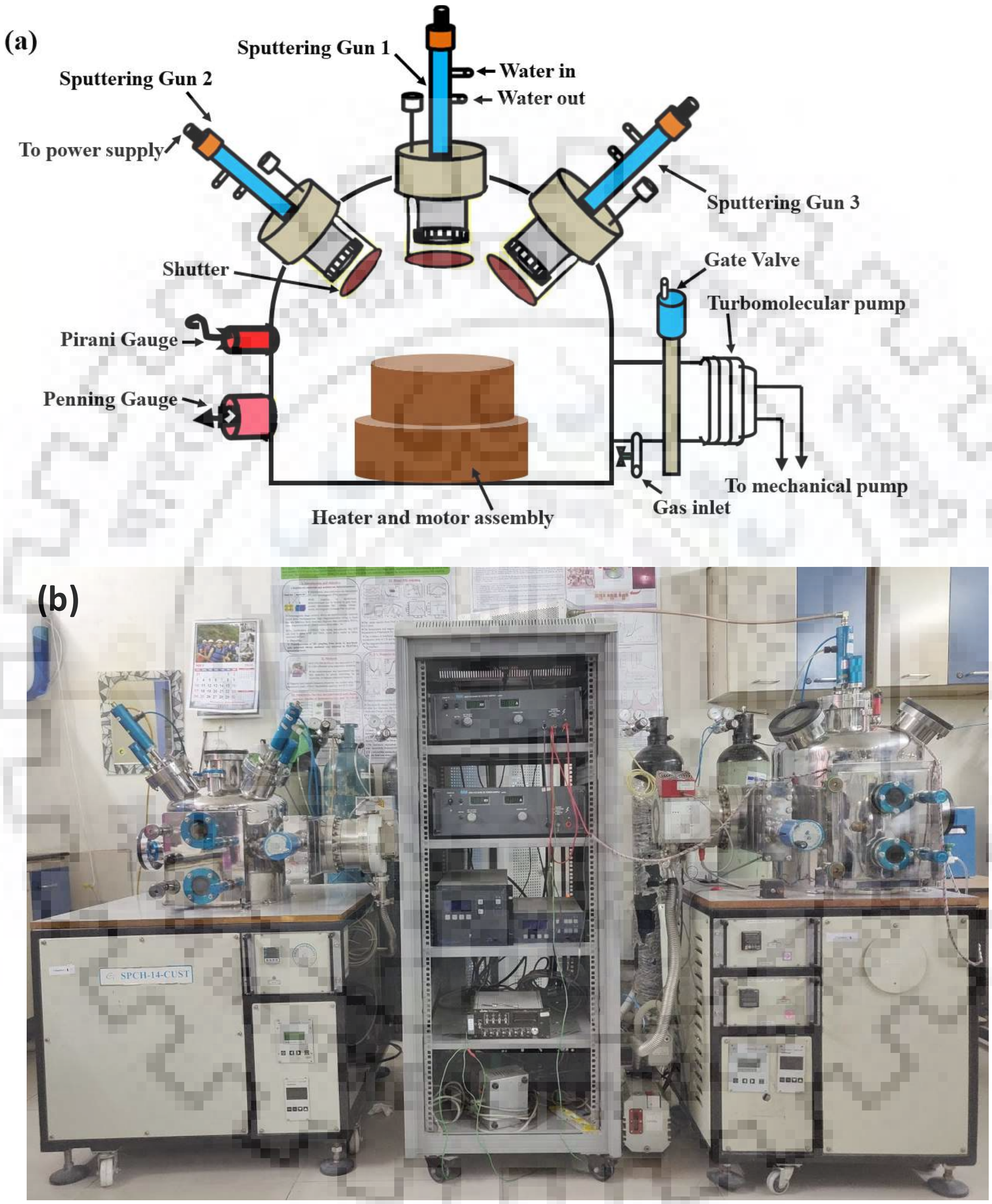

Figure 2.6 (a) Schematic diagram of sputtering chamber (b) Image of the sputtering chamber and power supplies.

Figure 2.6 (a) & 2.6 (b) shows the schematic drawing and photograph of DC/RF magnetron sputtering system for On-axis deposition in our research laboratory (Functional Nanomaterials Research Laboratory, Department of Physics, Roorkee). In this work, the custom-made magnetron sputtering system (Make-Excel instruments, Mumbai, India) was employed for the fabrication of proposed thin film structures. The system consists of several accessories: sputter target source (2" dia.), a rotating/fixed substrate heater with PID controller, gate valves, gas flow assemblage, gauge display, vacuum pumps (rotary & turbo pumps), reactive and sputtering gasses (Ar, O_2, N_2 etc.), chiller and DC/RF power supplies.

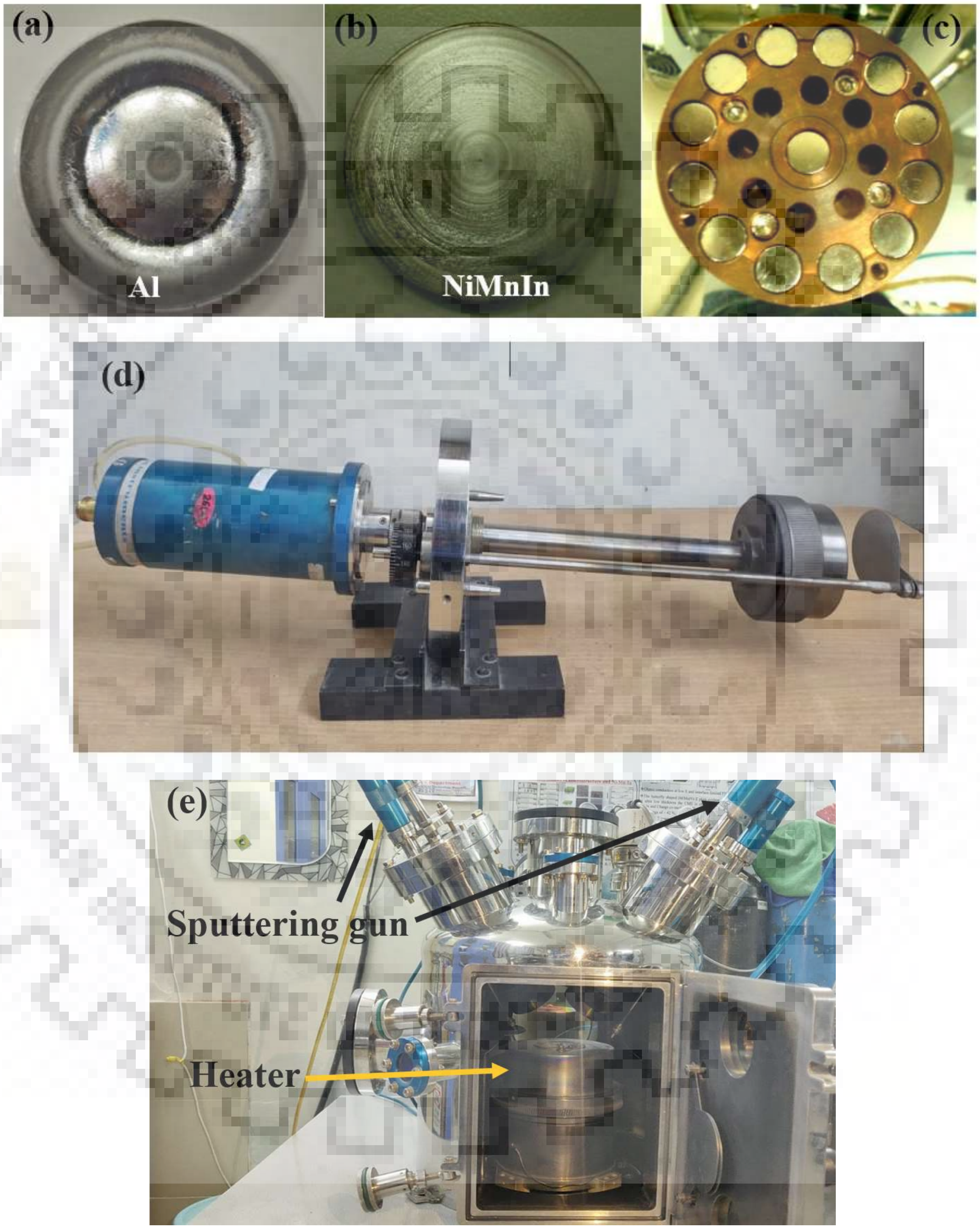

Figure 2.7 (a) Al target (b) NiMnIn target (c) Arrangement of magnets in sputtering gun (d) Image of Sputtering gun Assembly. (e) Close view of the sputtering chamber exhibiting position of heater and gun.

In brief, a circular disc of target material was attached to the magnetron guns consisting of an array of permanent magnets (**figure 2.7 (a- c)**). This manually designed system was specially developed for depositing thin films, composites, and heterostructures **(figure 2.7 (d, e)**. The substrates are mounted on a substrate holder using conducting adhesive (like a silver paste). After mounting the substrates, the sputtering chamber was initially evacuated to a base pressure of 2×10^{-6} Torr with the help of a rotary pump (Pfeiffer Vacuum, DUO Line, Germany) in series with a turbo molecular pump (Pfeiffer Vacuum, HIPace 700, Germany).

After the evacuation, a controlled flow of inert argon (Ar) gas was introduced into the chamber by a mass flow controller (make -MKS PR4000B, MKS Instruments, Germany. The Aplab DC power supply H10110 (50-1000V, 1 Amax. India) and Seren RF power supply (600W at 13.56 MHz) with a Seren MC-2 impedance matching network were employed as a voltage source for sputtering. The gas flow rate in the sputtering chamber was maintained by mass flow. Simultaneously, the throttling process could be done by adjusting the gate valve to match the gas influx and pumping-out rate. It is done to stabilize the pressure of the gas and its flow rate inside the chamber. Finally, the sputtering process can be started by applying a negative potential to the target. During this process, the sputtered atoms get deposited on the substrate leading to thin film formation. After deposition, the structural, electrical and mechanical characterization was done for their efficient application in magnetic field sensing devices applications.

2.2. Basic structural characterization techniques

2.2.1. X-ray diffraction (XRD)

X-ray diffraction is a powerful analytical instrument to produces unique fingerprint corresponding to Bragg reflections of crystalline materials. X-ray diffraction results from the interference of diffracted beams of a monochromatic X-ray source which are made to incidence on a crystalline structure. In a crystalline structure, the periodic arrangement of the atoms could be considered as scattering centres for X-rays.

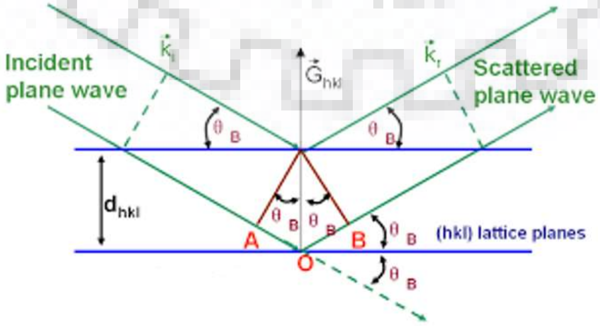

Figure 2.8. Schematic representation of Bragg equation.

Diffraction takes place between the waves when they encounter an obstacle whose size is comparable to their wavelength **[29]**. The X-rays easily gets diffracted by atomic planes as the wavelength X-ray is equal or comparable to the inter-planar spacing between the adjacent atomic planes which is of the order of few Å. If we consider a crystal structure with a periodic arrangement of atoms as shown in **figure 2.8**, then there are two geometrical factors which are to be considered: firstly, the incident beam, at right angles to the diffracting plane and the diffracted beam, all exists in the same plane, and secondly, the angle amid the incident and the diffracted beam (2θ), which is the diffraction angle usually measured experimentally. For an incident X-ray falling on a periodic structure making an angle θ with the plane, constructive interference for atomic planes of the crystal structure parallel to the sample plane takes place when the following condition is satisfied:

$$2dsin\theta = n\lambda \tag{2.1}$$

where, d is the spacing between the adjacent atomic planes, λ is the wavelength of the incoming X-ray, n is an integer signifying order of the reflection and θ, also called Bragg's angle, is the angle between the incident ray and reflecting plane. This equation for the diffraction of X-rays from atomic planes is known as Bragg's Law. The position of the peaks (2θ) is a measure of interplanar spacing, or d-spacing between planes of atoms in the structure X-ray diffraction is considered as the most extensively utilized technique for the identification of crystal structure, phase, orientation, lattice parameters and stress in a crystalline material. It is one of the oldest and non-destructive technique to analyze the samples and is still valid for all branches of solid-state physics. Every crystalline sample has its own exclusive XRD pattern where each peak relates to a unique and repeating set of parallel planes that are present and oriented in all the different directions of a three-dimensional lattice of crystals.

The X-ray diffraction pattern is analyzed with a 2θ value and relative intensities, which gives the information about the presence of exact phase. The area under the XRD peak is used to quantitative analyze the phases of the materials. The intensity of peaks mainly relies on the amount of material in the specimen. However, the qualitative analysis of the material is performed by the identification of the diffraction pattern of the material. The peak intensities tell us about the type of atoms present in the repeating crystal planes. The light atoms having a smaller number of electrons scatter X-rays weakly. On the other hand, heavy atoms having a large number of electrons scatter X-rays more effectively. In a nutshell, positions, and intensities of peaks, together define a unique fingerprint or identity of the material.

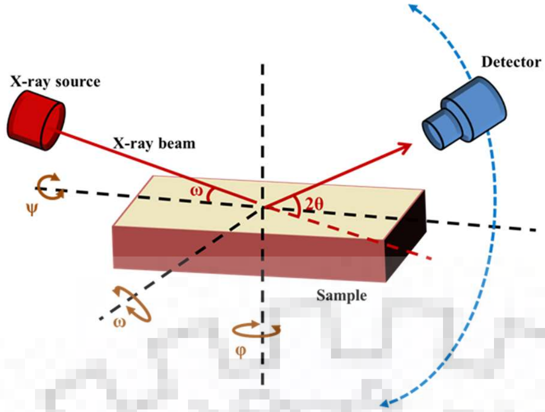

Figure 2.9 Schematic for angles involved in X-ray diffraction

Figure 2.9 shows the schematic diagram of all the angles involved in an X-ray diffraction measurement. Here, Ψ signifies tilt of the sample, φ relates the plane rotation and ω denotes the angle between the plane of the sample and the X-ray tube. For all the form of samples (powdered, pellet or bulk sample), the measurements were done in detector scan and locked coupled arrangement. In locked coupled scan, the tube and detector move simultaneously to cover the whole 2θ range (say 5 - 90°). This arrangement is therefore known as a θ-θ scan. Thus, angle ω and θ always remain same during the scan. While in detector scan, the tube remains to fix at a particular glazing angle (~0.5 or 1 or 2) and detector moves in the whole 2θ range (say 5 - 90°).

The operating power (voltage and current) for the X-ray tube were maintained at 40 kV×40 mA. The detector used in this characterization consists of a NaI scintillation counter, which works in the wavelength ranging from 0.5 to 3 Å. Monochromators are arranged in the path of X-rays to suppress the undesired portions of X-rays. The first aperture diaphragm is placed between the specimen and tube to restrict the irradiated specimen area. A second aperture diaphragm is used to suppress scattered radiation coming from the first aperture. The resolution of the signal is controlled by detector diaphragm. The peaks obtained in XRD diffractogram were indexed to identify the phase of the material and to estimate the lattice parameters and particle size.

In this present work, Bruker D8 Advance X-ray Diffractometer was used to analyze the crystal structure, phase, lattice parameters, orientation and any parasitic impurity phase present in the synthesized thin films. Schematic and photograph of Bruker D8 Advance X-ray Diffractometer are shown in **figure 2.10 (a) and (b)**, respectively.

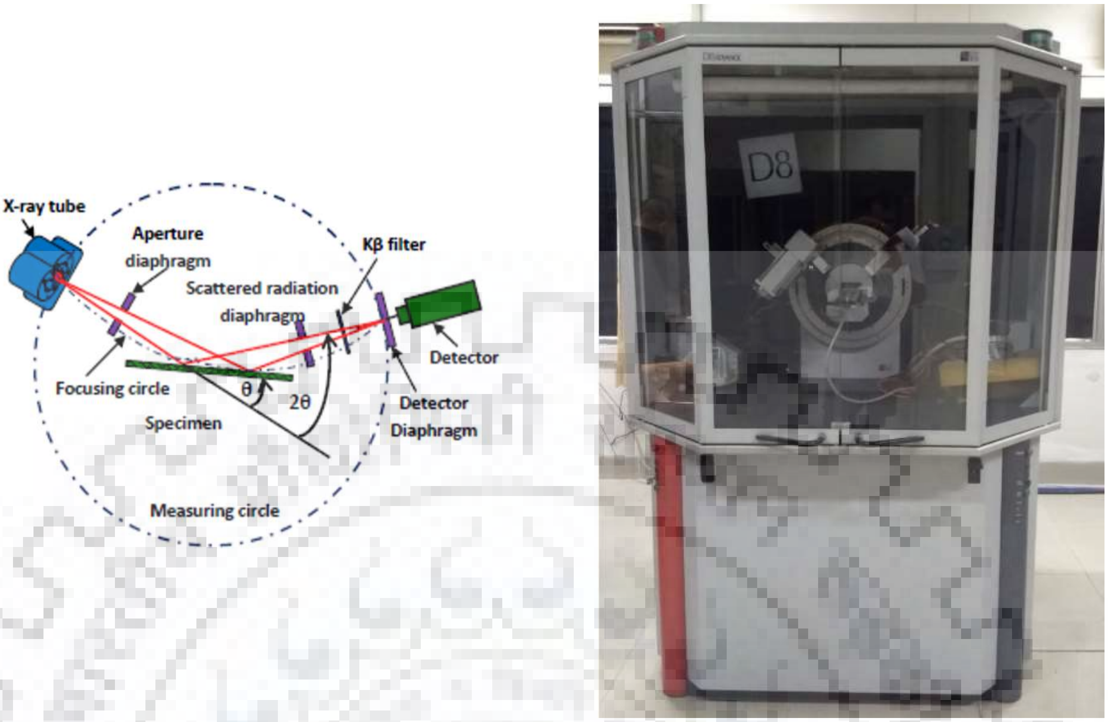

Figure 2.10. (a) Schematic and (b) Image of Bruker D8 Advance X-ray Diffractometer

Diffractometer, essentially, comprises an X-ray tube, an X-ray detector, and a sample holder. The radiation of λ =1.54 Å (Cu K_α) originating from the X-ray tube using a copper target are collimated and focused onto the sample. With the rotation of the detector, the intensity of the reflected X-rays is measured. The X-ray beam at the θ angle and the X-ray detector collects the signals and rotates at a 2θ angle relative to the direction of the incident X-ray beam. The hardware assembly used to control the angles and provide a mechanism for rotation to the detector is called a goniometer. Suitable detectors are employed to record diffracted X-ray that is further converted into an appropriate signal and sent to printer or monitor as an output.

2.2.2. Field emission scanning electron microscopy (FESEM)

The Scanning electron microscope is often the first analytical instrument required for "quick look" at a material. The field emission scanning electron microscopy (FESEM) is an incredible tool to produce images of high resolution; i.e. closely spaced features can be examined at high magnification. The scanning electron microscope has a large depth of field, which allows a large amount of sample to be in focus at one time. Conventional microscope generates the magnified image by using the series of glass lenses. While the FESEM generates with the help of electrons instead of light waves. Before discussing the details of FESEM technique, we need to understand the interaction between an electron and matter briefly. It is a beam-specimen interaction that makes electron microscopy possible. When an electron beam strikes the specimen, it undergoes a series of complex interactions with charge species (nuclei and electrons) of the atoms into the specimen **(figure 2.11)**. This interactions of electrons with matter produce a variety of products **[30]**, such as:

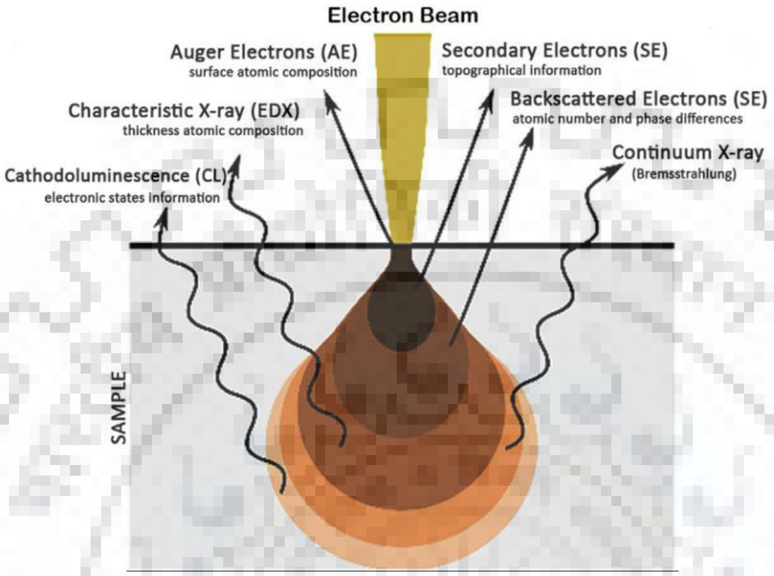

Figure 2.11 Schematic of an electron beam interaction.

i. Secondary electrons*:* Secondary electron (SE) are low energy electrons (0-50eV) that have been ejected from the outer electron shell of an atom on the surface of the specimen as a result of the impact from a highly energetic electron beam. The ejected electrons undergo a series of elastic and inelastic scattering until they reach the top of the specimen surface and would escape if they still have enough energy. Low energy SE are topography specific as only those SE can escape, which are produced very near to the surface (<10 nm). The SE yield means the number of SEs generated over each primary electron and it could be equal to or greater than 1. SEs are therefore large in numbers and are the most useful one for imaging purpose in scanning electron microscope.

ii. Backscattered electrons: *BSE* are high energy beam electrons that undergo sufficient elastic collisions on the sample surface with atomic nuclei to get scattered out of the interaction volume. They retain a significant percentage of the beam energy due to elastic collisions. Their dependence on the atomic number of the specimen is beneficial in the sense that apart from imaging topography, they can be used to improve material contrast and distinguish parts of the specimen with different atomic numbers. The regions on the surface of the sample having heavy elements and light elements, respectively, appear bright and dark on the screen. Backscattered electrons are not as large in number as secondary electrons, but most of them carry high energy and are useful for imaging, diffraction and analysis in FESEM.

iii. Elastic scattering*:* Elastic scattering results from Coulomb interactions between the primary electron (incident electron) and the positive potential cloud inside the electron cloud. Elastic scattering changes the direction of the primary electron without changing its energy. It is also known as Rutherford scattering and gives a strong forward peak distribution of scattered electrons. Elastic scattering is important for Transmission Electron Microscopy and also are main contributors for electron diffraction methods.

iv. Inelastic interactions: Inelastic scattering causes the primary electron to lose a detectable amount of energy as it collides with another electron or nucleus of the atom. The loss in the electron's energy should be more than 0.1 eV before it could be detected. There are many ways in which the primary electron could lose its energy and transfer it to another electron or atom of the specimen. During specimen beam interactions, inelastic scattering pumps the atoms in the sample to excited (unstable) state. Therefore, after some time, the atoms relax and return to their ground state, giving off the surplus energy. The production of X-rays, Auger electrons and cathodoluminescence are some of the prominent ways of relaxation. The analysis of relaxation energy can provide valuable information about each element present in the specimen. The electrons ejected from the atoms on the specimen's surface leaving behind vacancies which are filled by electrons from higher shells resulting into emission of X-rays. The energy dispersive spectroscopy (EDS) technique, based on measurement of the quantity of emitted X-rays, is usually used to carry out qualitative elemental analysis as X-ray energy is characteristic of the elements present in the specimen **[31,32]**.

v. Characteristic X-rays: As the primary electrons knock off the electrons from innermost orbits, holes are created and when an electron from a higher shell jumps to fill this vacancy an X-ray photon with energy equal to the difference between two states is emitted. These X-rays are characteristic property of the material and produced at a depth of 1-3 μm inside the sample. In SEM, these X-rays provide the data about the chemical composition of the active material.

vi. Auger electrons: When an electron jumps from a higher state to fill a vacancy in K shell, energy is released. This energy can eject an electron from external the M shell, which is termed as Auger electron. The kinetic energy of an Auger electron is characteristic of the emitting atom present in the material. The number of Auger electrons identified with specific energy corresponding to the concentration of the concerned element. Auger electrons are used in a highly sensitive surface analysis technique as they come from the depth of 5-75 Å of the specimen. After understanding the interaction of electrons with the specimen, the details of a FESEM are discussed here.

Field emission scanning electron microscopy (FE-SEM)

The *FESEM* system has a number of components, which can be seen in the block diagram of **figure 2.12.** In brief, a highly energetic monochromatic beam of electrons, needed for scanning microscopy, are produced from high-performance electron guns developed from single crystals of lanthanum hexaboride (LaB_6) or an ultra-fine tungsten tip (field emission guns) and accelerated towards anode at very high voltages of 2 to 50 kV **[33, 34]**. These electrons are called primary electrons. The controlled electron beam, required for proper column optics, needs an ultra-clean dust-free environment. Therefore, a very high vacuum of the order of 5x10^{-5} torr is created inside the electron column with the help of one or two vacuum pumps **[35]**.

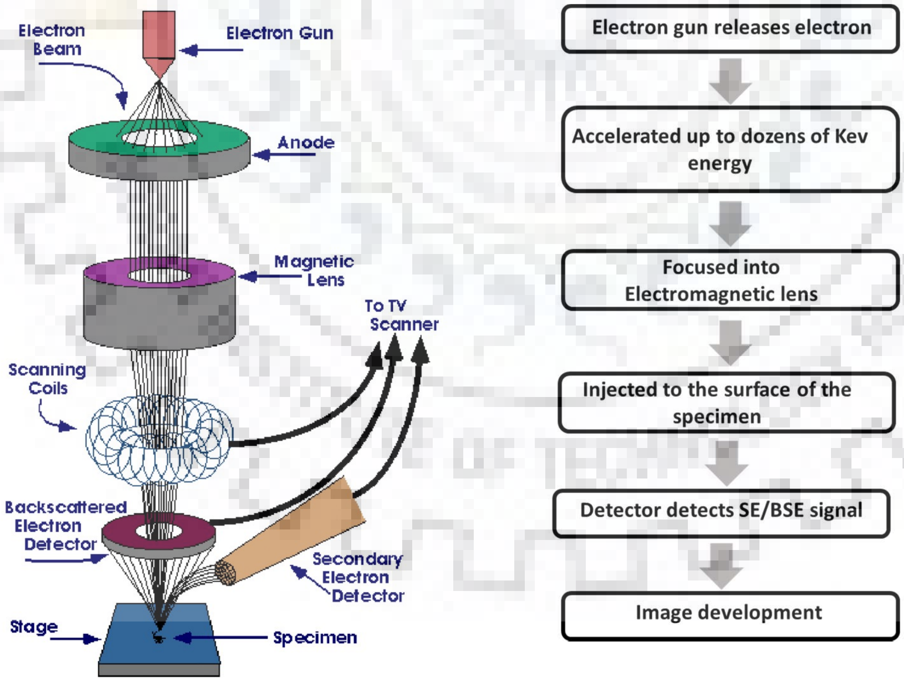

Figure 2.12. Schematic and working of a scanning electron microscope.

SEM utilizes a series of electromagnetic lenses and apertures to produce a focused electron beam that eventually renders an image of the surface of the specimen. The electron beam is converged and focused down to 1000 times its original size by condenser lenses. The accelerating voltage, applied at various stages in conjunction with condenser lenses, determines the intensity of the electron beam striking the specimen **[35].** In the electron column, one or more apertures are used to block electrons that are extraneous in the beam. The objective lens aperture placed just under the scanning coils does the final focusing of the beam and also determines the spot size of the beam on the surface of the specimen. The diameter of the electron beam used for scanning specimen is 5 nm to 2 μm. The electron beam in the presence of electronic lenses bombards on to the sample, resulting in the production of secondary electrons (*SEs*). The secondary electrons are emitted from each scan spot onto the sample (analyze material). Since the energy of the SEs is found to be penetration depth dependent, the electrons produced at the top surfaces are emitted out from the sample. On the other hand, the specimen itself rapidly absorbs those coming from the deep region of the specimen. It means that secondary electrons are found to be surface dependent.

A reasonable fraction of secondary and backscattered electrons is collected by suitable detectors due to beam-specimen interactions and converted into an electronic signal. This signal is amplified and converted to a video scan-image mode that can be perceived in the form of a digital image on a monitor, which can be saved and processed further. The voltages along x and y direction, used for rostering the electron beam, must be applied in perfect synchronism with x and y inputs to the CRT with the help of some feedback mechanism. As a result, for every point on the specimen hit by an electron beam, there is a corresponding point mapped straight on the screen to produce a vibrant image on CRT. The linear magnification (M) of the image is estimated as **[36]**:

$$M=L/l \tag{2.2}$$

where l is the length of the raster on specimen corresponding to L on CRT monitor. FESEM can produce very high-resolution images (about less than 1 to 5 nm in size) of a material surface. The main advantage of FESEM is their narrow electron beam, which produces a large depth of field, resulting in a characteristic *3D* appearance of the surface structure of the sample. Therefore, FESEM is a useful tool in research and development. The issue with SEM is that it works fine with conducting specimen only. For imaging insulating samples, they are made conductive by sputtering an extreme tiny layer (1.5 - 3.0 nm) of gold or gold-palladium to evade charging effect of the sample before imaging. Further, the system must sustain a good vacuum. A portable stage is used to move the samples in 5 direction such as horizontal, vertical and can also be rotated, tilted and translated.

In the present study, FESEM (Ultra Plus, 20 keV, Carl Zeiss, Germany) with a resolution of 2 nm and up to 80,000X magnification was employed to examine the surface morphology and cross-section of the samples, as shown in **figure 2.13.** FESEMs also have an excellent ability to observe the chemical composition of the analyzed sample with the help of EDX operation attached with FESEM

Figure 2.13. Photograph of FESEM (Carl Zeiss Ultra Plus) at IIC, IIT Roorkee.

2.2.3. Energy dispersive X-ray spectroscopy (EDX)

EDS or EDX is a chemical composition micro-analysis technique, which is attached with the FESEM system. In EDX, X-rays emitted from the sample surface are characteristic property of the atoms of the specimen. Each element has its own characteristic X-rays spectrum. Therefore, the X-rays can be utilized for detection of an element in the specimen **[30]**. Since X-rays can't be deflected, therefore, the detector should be aligned with the specimen and hence occupies the same position to the secondary electron detector. When the X-rays strike the detector, the electrons are excited to the conduction band leaving an equal number of holes in the outer shell. The generated electron-hole pairs are proportional to the energy of X-rays being produced. A fixed voltage is then applied transversely to the semiconductor, resulting in a flow of current with absorbing the X-rays by the detector. The magnitude of this current is found to be directly proportional to the energy of X-rays. The detector is partially coated with a layer of pure gold so that that bias potential can be applied.

This gold-coated outer surface is further protected by a Beryllium window (*Z=4*) to protect the contaminants from getting condensed on the cold surface of the detector. The current flow between the electrodes as the X-rays strike the detector for a very short period, called as a pulse. This pulse is then amplified and passed to a multichannel analyzer (*MCA*) which decides the particular channel for the pulse (Each channel represents different X-ray energy).

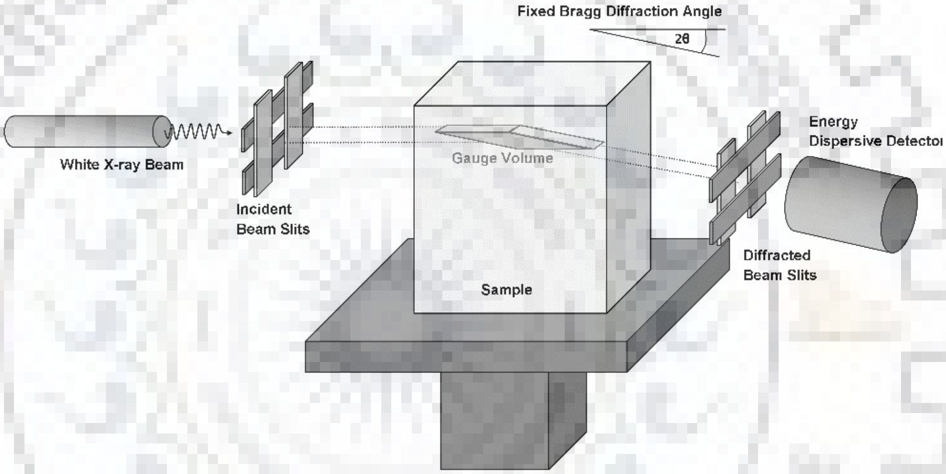

Figure 2.14. Processing schematic diagram of energy dispersive X-ray spectroscopy (EDX) (en.Wikipedia.org).

These charge pulses are transformed to a voltage pulse by a charge-sensitive pre-amplifier. After that, a multichannel analyzer is used to analyze these incoming signals, where these pulses are organized by voltage. The calculated energy of incident x-rays is referred to a computer for display and further process in data evaluation. Finally, a multifaceted spectrum of x-ray energy vs counts is observed to calculate the elemental chemical composition of the analyzed sample. The hardware and processing schematic of the EDX is shown in **figure 2.14**.

2.2.4. Atomic force microscopy (AFM)

Atomic force microscopy is the most commonly used form of scanning probe microscopy (SPM). The origin of this technique started with the progress of the scanning tunnelling microscopy (STM) in 1982 at the IBM, Zurich (by Binning and Roher) and got the Nobel Prize for this tremendous work in the field of material science. However, STM is used in conductive or semi-conductive materials. Therefore, to extend this kind of microscopy for non-conducting materials, the AFM was established. AFM maps out the topography of a surface by sensing the forces of interaction between the atoms of the sample surface and the probe tip. The basic AFM processing scanned over the sample is addressed in **figure 2.15**.

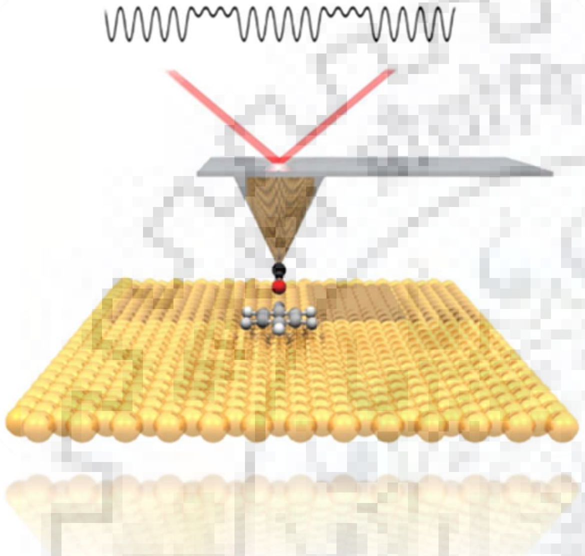

Figure 2.15. Basic AFM processing in which sample is scanned under the tip or tip is scanned over the sample. (nanohub.org)

To image the surface features, the sample is scanned by an atomically sharp tip, usually made of Si or Si_3N_4, attached to the lower side of a reflective cantilever. Light from a diode laser is focused on the cantilever and is reflected on to a segmented photodiode. As the sample is scanned below the tip, the cantilever moves up and down which changes the ratio of light falling on the four elements of the photodiode. The difference in the intensity falling on the four elements is converted into a proportional voltage by the photodiode. This voltage serves as a feedback signal enabling the tip to maintain either a constant force or a constant height above the sample. For most applications, the AFM is operated in one of the following three modes (**figure 2.16**):

i. ***Contact mode:*** In contact mode, the sample is scanned with the tip in close contact with the surface. A piezoelectric positioning element is used to exert a repulsive force on the tip to push the cantilever against the sample surface. The major problem during contact mode is that tip may scratch on the surface and change its intrinsic features.

ii. ***Non-contact mode:*** In this method, the tip is held at a distance of 50-150 Å from the sample surface. Attractive Van der Waals forces between tip and sample are detected in this mode to construct the image of the sample's surface below the tip. These attractive forces are significantly weaker than the repulsive forces used in contact mode. Therefore, tip produces small oscillation and change in amplitude, phase, or frequency of the oscillating cantilever; hence the image is no so good as compared to contact mode.

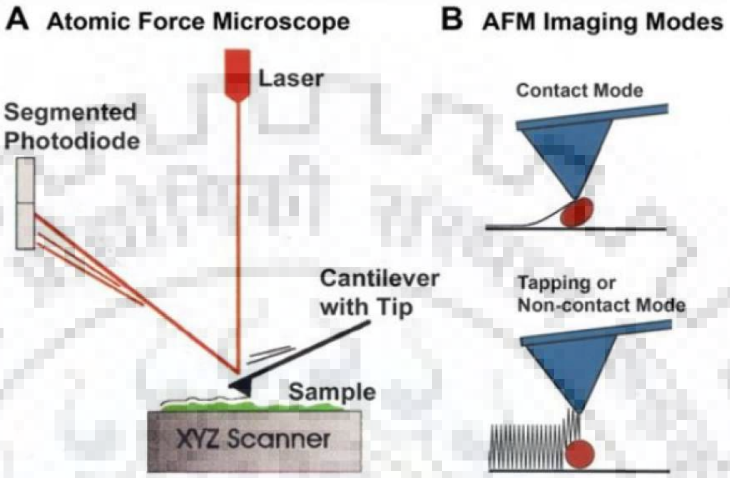

Figure 2.16. Schematic diagram of different modes in AFM.

iii. Semi-contact mode: Semi-contact mode sometimes called intermitted mode is developed to achieve high resolution avoiding destructive frictional forces on the sample surface. In this mode, a piezoelectric cantilever oscillating at its natural frequency is moved down near to the surface of the sample till its tip feels the surface and giving signals and then immediately lifted off. The sample is scanned continuously below the tip.

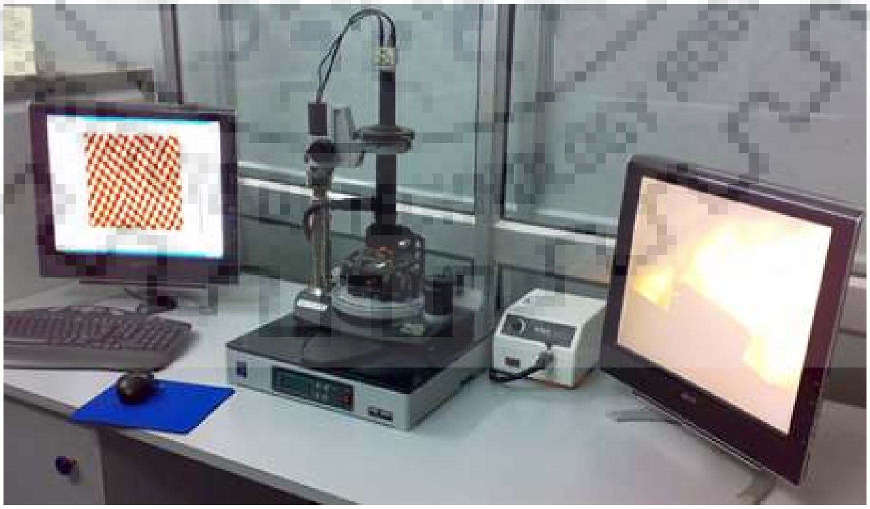

Figure 2.17 Photograph of Atomic Force Microscope (at IIC, IIT Roorkee, India)

In the present thesis, the Atomic Force Microscope (NATEGRA Prima, NT-MDT Spectrum Instruments, Russia) has been used for roughness measurement of the thin films and structures (**figure 2.17**).

2.2.5. X-ray photoelectron spectroscopy (XPS)

XPS is a non-destructive photo-emission technique for surface characteristics because it is a surface-sensitive technique, which can examine the valence-state of atom/ion species at the solid surface. The XPS spectrum is obtained by irradiating the sample with monochromatic X-rays of known energy, under ultra-high vacuum and analyzing the energies of the emitted electrons from the occupied energy levels of the atoms/ions in the sample **[37, 38]**. This technique is extensively utilized to study the chemical state, electronic state and atomic ratio of each element present in the test sample. In XPS analysis, the sample is irradiated by monochromatic soft X-rays which causes the emission of photoelectrons from the surface of the sample. To eject photoelectron, the energy (hν, where h is the Planck constant and ν is the photon frequency) should be larger than the binding energy (BE) of a certain state of the atom/ion (**figure 2.18**). The ejected electrons have kinetic energy, E_K.

$$E_B = h\nu - E_k - \phi \tag{2.3}$$

where ϕ the work function, i.e., the potential difference between the Fermi level of the solid and the vacuum level. A conventional approach for the analyze sample is to reference E_B to its Fermi level **[39]**.

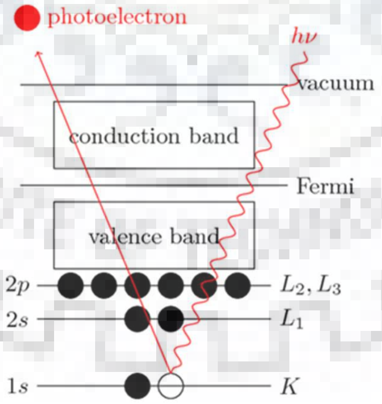

Figure 2.18. Core energy level diagram of X-ray photoelectron emission process (warwick.ac.uk).

XPS technique provides the spectra between BE and counts. The spectra are generally standardized using reference photo-emission peaks of the sample substrate. For example, carbon is used as a reference because the C1s peak is existing in every analyzed sample with BE equal to E_B=284.6 eV. X-ray photoelectron spectroscopy is a surface-sensitive technique, which can be used to determine the chemical composition of the material. Therefore, this is well-known as Electron spectroscopy for chemical analysis (ESCA). A block diagram of XPS is shown in **figure 2.19**.

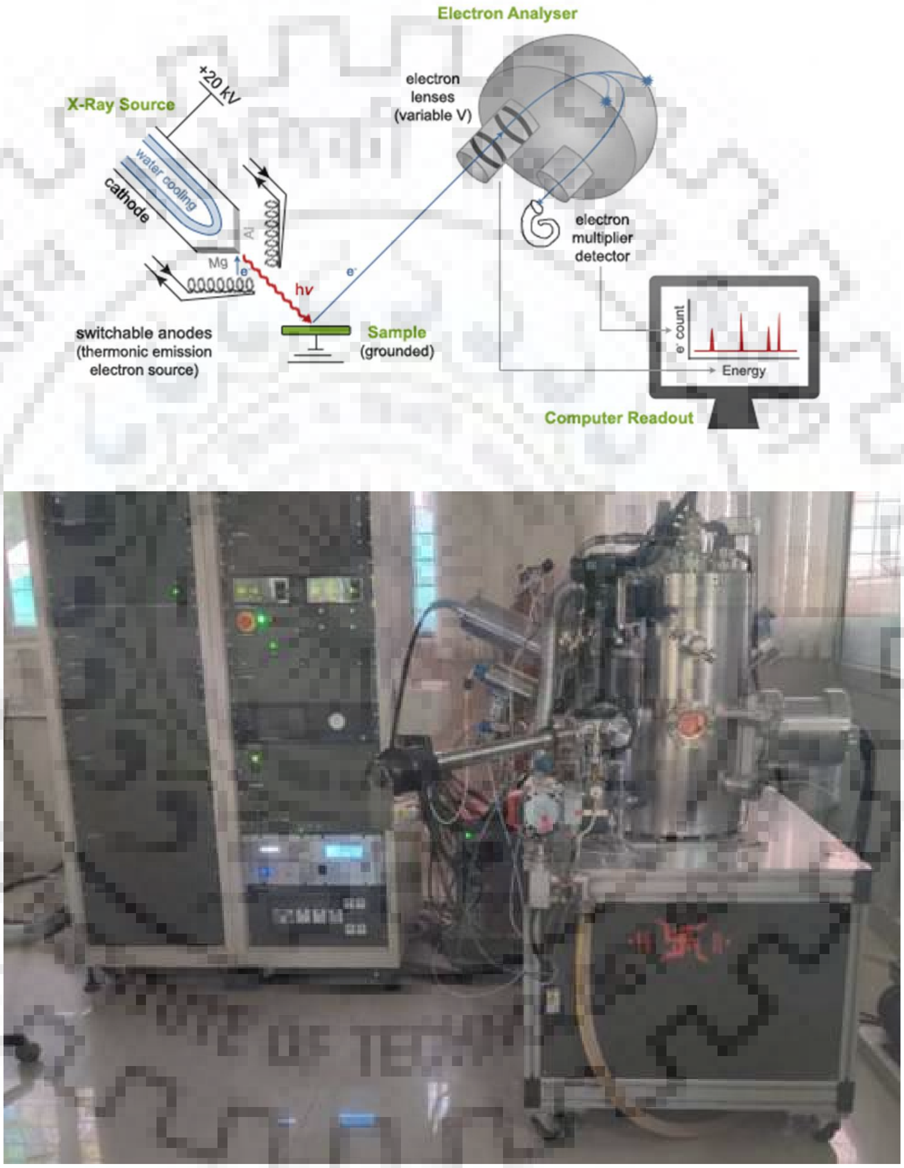

Figure 2.19. Schematic diagram (J. H. Horton 2009) and Photograph of the XPS measurement setup at IIC, IIT Roorkee

In the current study, the XPS measurement was executed on PHI, Versa probe III electron spectrometer using the following recipe (X-ray source Al K_α 1486.708 keV, step size = 0.05 eV), energy resolution = 0.5 eV, pass energy = 55 eV, and a base pressure 10^{-9} Pa, facilitated at

IIC, IIT Roorkee (**figure 2.19**). An Ar-ion gun was employed to neutralize the sample surface before acquiring the XPS spectra. The peak position of the C1s spectrum with a BE is equal to 284.6 eV is also used for calibration purpose because the adventitious carbon is present on the sample surface. Therefore, XPS is a dominant tool, which is widely employed for the surface investigation of the active materials **[40-42]**. It provides the information of electronic structure, chemical state and bonding of the elements present on the sample surface.

2.3. Electrical and magnetic characterization

2.3.1. Piezo-force Microscopy

Piezoelectric force microscopy (PFM) is a variant of Atomic force microscopy (AFM) that permits the detection of ferroelectric and piezoelectric properties at the nanoscale. PFM make use of coupling between the polarization and mechanical displacement for imaging as well as manipulation of ferroelectric/piezoelectric material domains. The PFM is performed with the help of conductive tip. The tip is then brought into contact with the surface of the material under test. **[43, 44]**

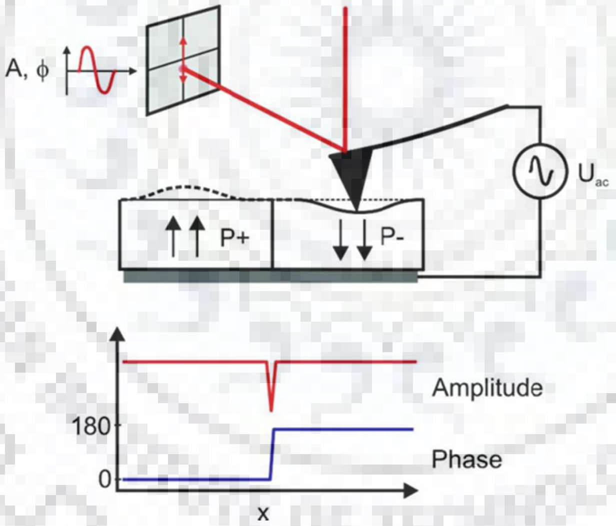

Figure 2.20 Principle setup of Piezo Force Microscopy

A voltage is applied between the conductive tip and the electrode below the piezoelectric material. As a result of the converse piezoelectric effect, the sample under observation will either get compressed or expanded under the applied voltage signal. Since the tip is in contact with the piezoelectric sample surface, the expansion/compression in the piezoelectric layer gets transferred to the PFM tip. If in the beginning, the domain polarization is anti-parallel to the applied *E*-field, the domain would shrink and in turn, leads to a reduced cantilever deflection (**figure 2.20**). The quantity of change in cantilever deflection, in such circumstances, is directly proportional to the amount of contraction or expansion of the sample ferroelectric (electric) domains, and hence related to the applied E-field.

When a DC voltage is applied to the piezoelectric material, the displacement on the surface of the piezo-layer developed is too small because the values of piezoelectric coefficients are relatively small. Therefore, a noise lock-in- amplifier is used to detect a low-level signal. A voltage (V_{tip}) is applied on the cantilever tip of the PFM.

$$V_{tip} = V_{dc} + V_{ac} \cos(\omega t) \tag{2.4}$$

where V_{ac} is the probing bias, V_{dc} is the switching bias and ω is the driving frequency. This supply gives birth to an oscillatory displacement of the sample surface,

$$A = A_o + A_1 \cos(\omega t + \varphi) \tag{2.5}$$

where A_o is the static surface displacement, A_1 is the voltage induced deformation, and a φ is the phase shift between V_{ac} and A_1. The photodiode measures the resulting change in the cantilever deflection, and so a vibrating surface displacement is transformed into an oscillating voltage.

2.3.2. Semiconductor Characterization System 4200

The semiconductor characterization System from Keithley (Model SCS 4200) is a complete solution for DC measurement of semiconductor devices, materials and test structures. The system is equipped with Windows NT based PC and Keithley Interactive Test Environment (KITE) to support a commanding single-box solution for unprecedented measurement speed with high accuracy. The interactive support helps the users to increase their familiarity with tasks such as handling tests and generating reports or results within a short period. The characterization system can be programmed to measure the C-V and I-V behaviour of the test structures and the semiconductor devices. The excellent low current performance of the semiconductor characterization makes it an ideal tool for leakage current measurements.

In the reported work, SCS was used to measure the current-voltage characteristics of the fabricated structure. The **figure 2.21** shows the block diagram and photograph of Keithley made SCS 4200 system **[45]**.

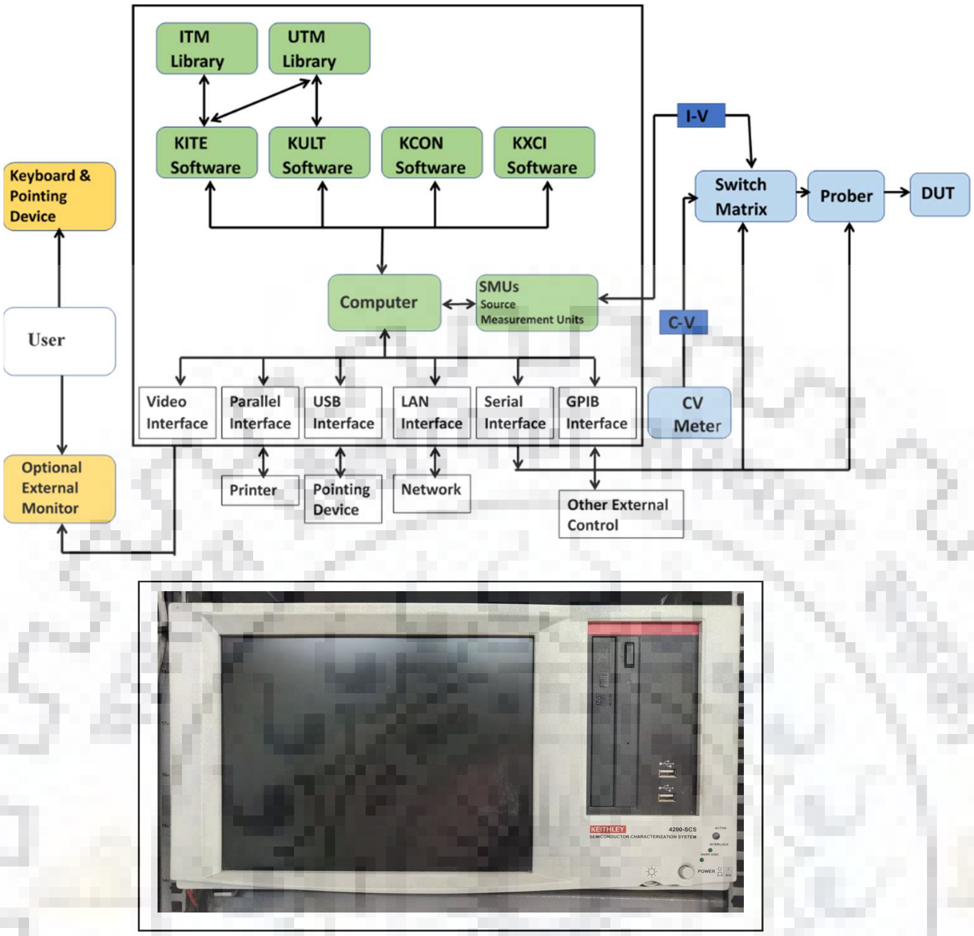

Figure 2.21 Block diagram and photograph of SCS 4200 in FNRL (Lab) at IIT Roorkee

2.3.3. Agilent Impedance Analyser 4294A

Dielectric measurements of the samples were carried out using Agilent 4294A Impedance Analyser attached to a computer and cryohead system via GPIB interface, measurement cables, and software. In Agilent 4294A, the measurement can be made over the wide frequency range from 40 Hz to 110 MHz with +/- 0.08 % basic impedance accuracy.

A signal source (microprocessor-controlled frequency synthesizer) sends high-resolution test signals with a maximum frequency resolution of 1 mHz. The test signal level range and DC bias range are, respectively, 5 mV to 1 V_{rms} (200 µA to 20 mArms) and 0 V to +/-40 V (0 mA to +/-100 mA) **[46,47]**. Some errors arising during measurements are eliminated by advanced calibration and error compensation functions.

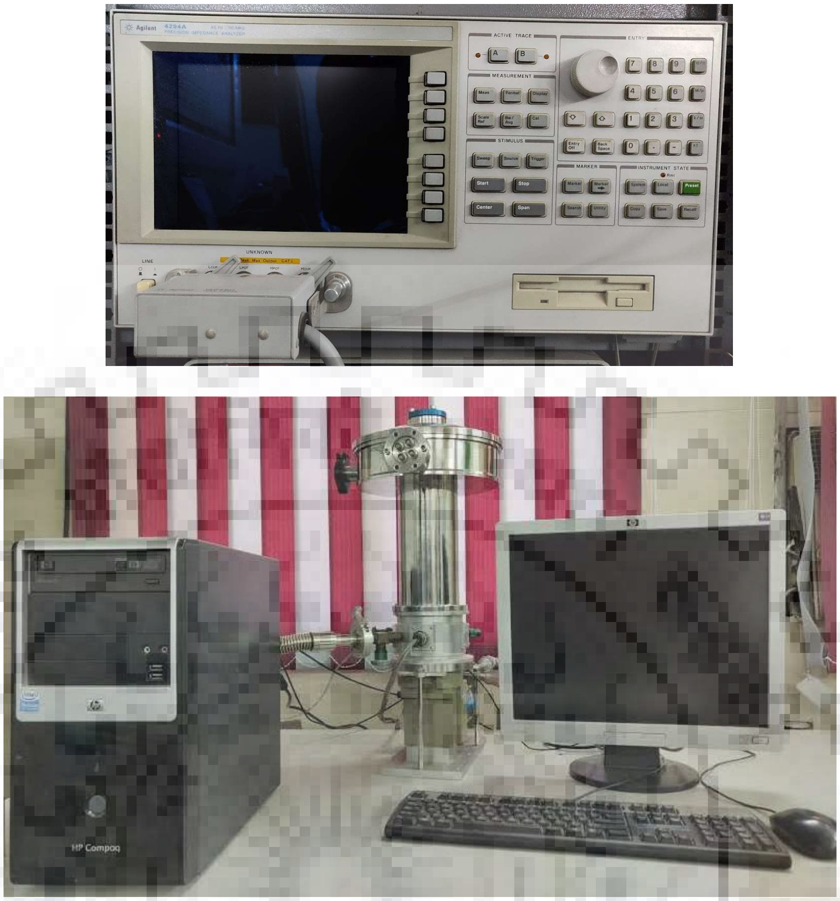

Figure 2.22 Photograph of impedance analyzer temperature variable assembly in FNRL Lab at IIT Roorkee.

In the reported work, impedance analyzer was used to measure the dielectric properties of the fabricated structure (**figure 2.22**). The variable temperature dielectric and current-voltage experiments were carried by connecting the SCS-4200 and impedance analyzer 4294A with a temperature variable assembly system (**figure 2.22**). The temperature variable assembly consists of heater and cryohead to work proficiently in the range from 40K to 500K efficiently.

2.3.4. Vector Network Analyzer

Vector network analyzer (VNA) is an electrical instrument to measure the performance of the components such as amplifiers, filters, antenna, cables, mixers, etc. VNA is also used for verification and troubleshooting of the specific component in RF and microwave systems **[48,49]**. VNA includes a source and a set of receivers, which are used for the generation of a known stimulus signal, and to measure changes to this stimulus caused by the material-under-test (MUT).

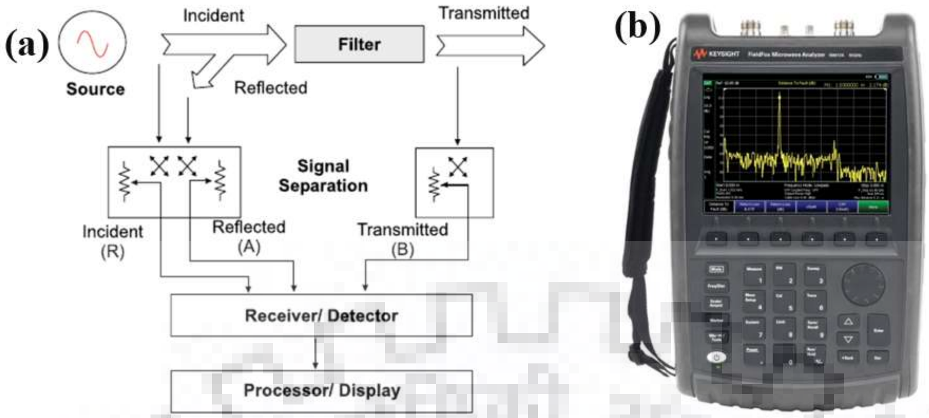

Figure 2.23 (a) Block diagram and (b) a photograph of a Vector Network Analyzer (VNA)

Figure 2.23 (a) displays the basic block diagram of a VNA. It shows that the signals are incident from the source on MUT. The stimulus signal that is injected into the MUT get reflected from the MUT and also get transmitted through it. Both the reflected as well as transmitted signals are then measured with the help of VNA. The resulting signal is then compared with the known stimulus signal by the receivers. Then either an internal or external computer processes the obtain data and send the results to a display.

With the increase in the bandwidth of today's electronics circuits, it is very important to characterize the response of individual components over a wide frequency range. Traditional low-frequency parameters such as capacitance, gain, resistances are frequency-dependent and hence cannot describe the performance of the system. Also, it is not possible to characterize every parameter of a complex system over a large frequency range, so system-level characterization using *S*-parameters are used for better verification of the system response.

The incident waves are excited in the system (reflected or transmitted) from the port to evaluate the multiport network. The ratio of the signals coming from different ports is known as the S-parameter. They are complex numbers and are stated in terms of both magnitude and phase and are the frequency domain description of the electrical response of a network. These parameters are used to characterize the network with different conditions of incidence and reflectance/transmittance. In the present work, the frequency response of the purposed bulk acoustic resonator was measured using a vector network analyzer (Keysight made) at CSIR-CEERI Pilani, India (**figure 2.23(b)**).

2.3.5. VSM

The vibrating sample magnetometer (VSM) is a sensitive and fast scientific instrument to study the magnetic properties of materials such as paramagnetic, ferrimagnetic, ferromagnetic, diamagnetic, etc. The working principle of VSM is Faraday's law of induction or generation of an electric field is with a change in magnetic flux. In this instrument, a constant magnetic field is first applied to the sample. This magnetic field aligns the magnetic spins or magnetic domains and finally magnetize the sample under observation. There is a creation of the magnetic field near the sample because of the magnetic dipole moment in the sample. Change in the magnetic field as a function of time is observed when a sample moves up and down. A pick-up coil is used to sense this change in a magnetic field. Due to variation in magnetic flux, a voltage is induced across this pick-up coil. The magnetization of the samples was carried out as a function of magnetic field and temperature using vibrating sample magnetometer.

The induced emf is a measure of the magnetization of the sample, and it results in electric current through the coil. This current is directly related to the magnetization in the sample. The current is higher for the sample, which is highly magnetized **[50, 51]**. The induced current is of very low amplitude for actual detection. So, a lock-in-amplifier and transimpedance are used to amplify the detected current from the pick-up coil. The measurement is achieved by moving the sample near the detection coil. The voltage is detected synchronously in the pick-up coils due to the simple harmonic motion of the sample in a magnetic field. The induced voltage is given by

$$V_{coil} = \frac{\partial \Phi}{\partial t} = \frac{\partial \Phi}{\partial z} \times \frac{\partial z}{\partial t} \tag{2.6}$$

Where t is the time, Φ denotes the magnetic flux bounded by the pick-up coil, and z is the displacement in the vertical direction of the sample from the centre of the coil. The system can detect a change in magnetic field up to a range of 10^{-9} emu with compact gradiometer pick-up coil configuration having a relatively large oscillation amplitude (typically 2mm) with a frequency of 20Hz. The vibrating sample magnetometer consists primarily of electronics for driving the linear motor transport for vibrating the sample, a pick-up coil, and software support for application and control **(figure 2.24 (a))**.

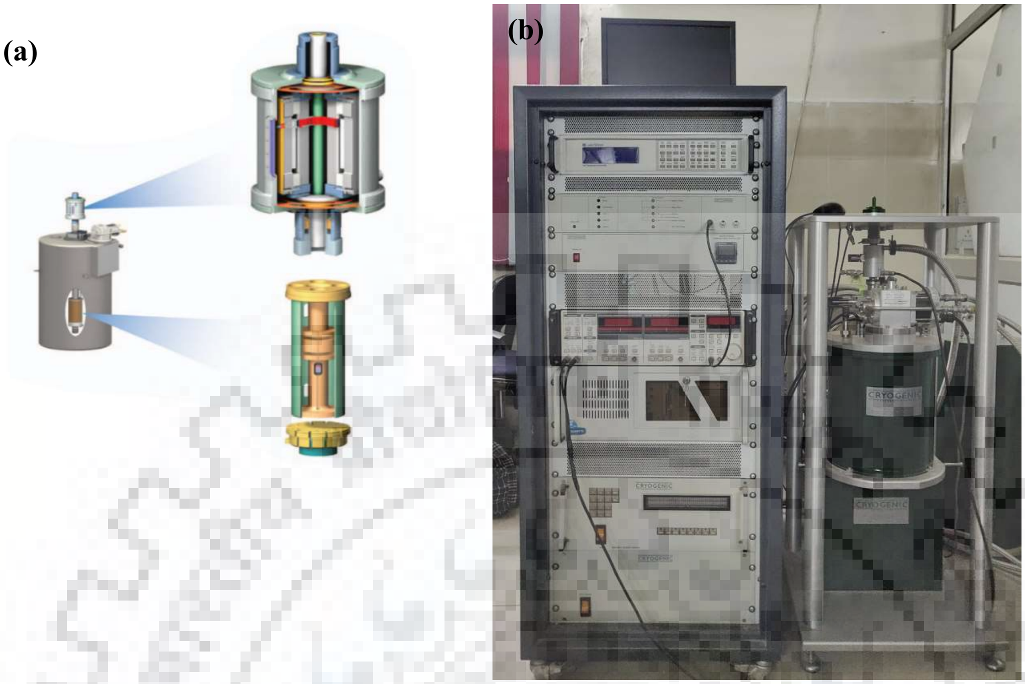

Figure 2.24 (a) Sample motor and detection coil set (b) Photograph of VSM (Cryogenic Ltd. UK) Functional Nanomaterials Research Laboratory, Department of Physics,

The temperature and field dependent magnetization (M-T and M-H) measurements of the samples were performed using SM (Cryogenic Ltd. UK). **Figure 2.24** (b) shows the photograph of the vibrating sample magnetometer in Functional Nanomaterials Research Laboratory, Department of Physics, IIT Roorkee used in carrying out the reported work.

2.4. References

[1]. Tadigadapa, West, A.R., 2003. ’Solid State Chemistry’ John willey & Sons.

[2]. Chopra, K.L. and Kaur, I., 1969. Thin film phenomena (Vol. 137). New York: McGraw-hill.

[3]. Ohring, M., 1992. The Materials Science of Thin Films. Inc.

[4]. Shah, H.N., Jayaganthan, R., Kaur, D. and Chandra, R., 2010. Influence of sputtering parameters and nitrogen on the microstructure of chromium nitride thin films deposited on steel substrate by direct-current reactive magnetron sputtering. Thin Solid Films, 518(20), pp.5762-5768.

[5]. Nayar, P., Khanna, A., Kabiraj, D., Abhilash, S.R., Beake, B.D., Losset, Y. and Chen, B., 2014. Structural, optical and mechanical properties of amorphous and crystalline alumina thin films. Thin Solid Films, 568, pp.19-24.

[6]. Chopra, K., 2012. Thin film device applications. Springer Science & Business Media.

[7]. Kaiser, N., 2002. Review of the fundamentals of thin-film growth. Applied optics, 41(16), pp.3053-3060.

[8]. Anders, A. and Brown, J., 2011. A plasma lens for magnetron sputtering. IEEE Transactions on Plasma Science, 39(11), pp.2528-2529.

[9]. Periasamy C, Prakash R and Chakrabarti P 2010 Effect of post annealing on structural and optical properties of ZnO thin films deposited by vacuum coating technique J. Mater. Sci. Mater. Electron. 21 309–15.

[10]. Singh, M., Singh, V.N. and Mehta, B.R., 2008. Synthesis and Properties of Nanocrystalline Copper Indium Oxide Thin Films Deposited by RF Magnetron Sputtering. Journal of nanoscience and nanotechnology, 8(8), pp.3889-3894.

[11]. Kumar, S., Kumar, C., Jesudasan, J., Bagwe, V., Parab, P., Raychaudhuri, P. and Bose, S., 2015. Origin of matching effect in anti-dot array of superconducting NbN thin films. Superconductor Science and Technology, 28(5), p.055007.

[12]. Mehta, B.R. and Ogryzlo, E.A., 1990. Deposition of diamond-like films by laser ablation. Surface and Coatings Technology, 43, pp.80-87.

[13]. Chattopadhyay S, Ayyub P, Palkar V R, Multani M S, Pai S P, Purandare S C and Pinto R 1998 Dielectric properties of oriented thin films of $PbZrO_3$ on Si produced by pulsed laser ablation J. Appl. Phys. 83 7808–12.

[14]. Raychaudhuri, P., Mukherjee, S., Nigam, A.K., John, J., Vaisnav, U.D., Pinto, R. and Mandal, P., 1999. Transport and magnetic properties of laser ablated $La_{0.7}Ce_{0.3}MnO_3$ films on $LaAlO_3$. Journal of applied physics, 86(10), pp.5718-5725.

[15]. Liu, H.D., Zhao, Y.P., Ramanath, G., Murarka, S.P. and Wang, G.C., 2001. Thickness dependent electrical resistivity of ultrathin (< 40 nm) Cu films. Thin Solid Films, 384(1), pp.151-156.

[16]. Ohtomo, A., Kawasaki, M., Sakurai, Y., Ohkubo, I., Shiroki, R., Yoshida, Y., Yasuda, T., Segawa, Y. and Koinuma, H., 1998. Fabrication of alloys and superlattices based on ZnO towards ultraviolet laser. Materials Science and Engineering: B, 56(2-3), pp.263-266.

[17]. Singh, P., Kumar, A. and Kaur, D., 2007. Growth and characterization of ZnO nanocrystalline thin films and nanopowder via low-cost ultrasonic spray pyrolysis. Journal of Crystal Growth, 306(2), pp.303-310.

[18]. Beri, R.K., Khanna, P.K., Singh, V. and Mehta, B.R., 2011. "Yellow emitting" magic-size cadmium selenide nanocrystals via a simplified spray pyrolysis method. Current Applied Physics, 11(3), pp.809-811.

[19]. Shukla M, Pramila, Dixit T, Prakash R, Palani I A and Singh V 2017 Influence of aspect ratio and surface defect density on hydrothermally grown ZnO nanorods towards amperometric glucose biosensing applications Appl. Surf. Sci. 422 798–808.

[20]. Sachdeva, A. and Tandon, R.P., 2012. Effect of sol composition on dielectric and ferroelectric properties of PZT composite films. Ceramics International, 38(2), pp.1331-1339.

[21]. Singh, S.K., Ishiwara, H. and Maruyama, K., 2006. Room temperature ferroelectric properties of Mn-substituted $BiFeO_3$ thin films deposited on Pt electrodes using chemical solution deposition. Applied Physics Letters, 88(26), p.262908.

[22]. Singh, S.K., Maruyama, K. and Ishiwara, H., 2008. Frequency-dependent polarization in $BiFeO_3$ thin films. Integrated Ferroelectrics, 98(1), pp.83-89.

[23]. Pandey R K, Tripathi A S M, Pandey S S and Prakash R 2019 Optoelectrical anisotropy in graphene oxide supported polythiophene thin films fabricated by floating film transfer Carbon N. Y. 147 252–61.

[24]. Torres-Huerta, A.M., Dominguez-Crespo, M.A., Onofre-Bustamante, E. and Flores-Vela, A., 2012. Characterization of ZrO_2 thin films deposited by MOCVD as ceramic coatings. Journal of Materials Science, 47(5), pp.2300-2309.

[25]. Ehiasarian, A.P., Anders, A. and Petrov, I., 2007. Combined filtered cathodic arc etching pretreatment–magnetron sputter deposition of highly adherent CrN films. Journal of Vacuum Science & Technology A: Vacuum, Surfaces, and Films, 25(3), pp.543-550.

[26]. Srivastava, P.K., Vankar, V.D. and Chopra, K.L., 1985. High rate reactive magnetron sputtered tungsten carbide films. Journal of Vacuum Science & Technology A: Vacuum, Surfaces, and Films, 3(6), pp.2129-2134.

[27]. http://ia.physik.rwth-aachen.de/research/ sputtering/www-sputter-eng.pdf.

[28]. http://www.unc.edu/~justink/RF DC_Sputtering .pdf (2007)

[29]. Cullity, B.D., 1956. Elements of X-ray Diffraction. Addison-Wesley Publishing.

[30]. Beanland, R., Goodhew, P.J. and Humphreys, J., 2001. Electron Microscopy and Analysis.

[31]. Parlinska-Wojtan, M., Meier, S. and Patscheider, J., 2010. Transmission electron microscopy characterization of TiN/SiN$_x$ multilayered coatings plastically deformed by nanoindentation. Thin Solid Films, 518(17), pp.4890-4897.

[32]. Egerton, R.F., 2011. Electron energy-loss spectroscopy in the electron microscope. Springer Science & Business Media.

[33]. Parlinska-Wojtan, M., Cancio, J.C., Meier, S. and Patscheider, J., 2007. TEM Characterisation of Indented TiN/SiN$_x$ Multilayered Coatings. Microscopy and Microanalysis, 13(S03), pp.384-385.

[34]. Voutou, B., Stefanaki, E.C. and Giannakopoulos, K., 2008. Electron microscopy: The basics. Physics of advanced materials winter school, 1(11).

[35]. Cheney, B., 2007. Introduction to scanning electron microscopy. Materials Engineering department San Jose State University.

[36]. Hafner, B., 2007. Scanning electron microscopy primer. Characterization Facility, University of Minnesota-Twin Cities, pp.1-29.

[37]. Hertz, H., 1887. On the influence of ultraviolet light on electrical discharge. Annals of Physics, 267 (8), pp.983-1000.

[38]. Einstein, A., 1965. Concerning a heuristic point of view toward the emission and transformation of light. American Journal of Physics, 33(5), p.367.

[39]. Moulder, J.F., 1995. Handbook of X-ray photoelectron spectroscopy. Physical electronics, pp.230-232.

[40]. Biswas, C., Banik, S., Shukla, A.K., Dhaka, R.S., Ganesan, V. and Barman, S.R., 2006. Surface composition and electronic structure of Ni$_{2+x}$Mn$_{1-x}$Ga studied by X-ray photoelectron spectroscopy. Surface science, 600(18), pp.3749-3752.

[41]. Winograd, N. and Gaarenstroom, S.W., 1980. X-ray photoelectron spectroscopy. Physical Methods in Modern Chemical Analysis, 2, pp.115-169.

[42]. Dhaka, R.S. and Barman, S.R., 2009. X-ray photoemission studies on rare gas bubbles in aluminium with annealing temperature. Surface and Coatings Technology, 203(17-18), pp.2380-2382.

[43]. Soergel, E., 2011. Piezoresponse force microscopy (PFM). Journal of Physics D: Applied Physics, 44(46), p.464003.

[44]. Zavala, G., Fendler, J.H. and Trolier-McKinstry, S., 1997. Characterization of ferroelectric lead zirconate titanate films by scanning force microscopy. Journal of Applied Physics, 81(11), pp.7480-7491.

[45]. Instruments, K., 2009. " Model 4200-SCS Semiconductor Characterization System Reference Manual. 4200-901-01 Rev. K/February 2009.

[46]. Haruta, H., 2000. Agilent Technologies Impedance Measurement Handbook. Agilent Technologies Co. Ltd.

[47]. Note, P., Agilent PN 4294A New Technologies for Accurate.

[48]. Henze, A., Monasterios, G., Ponce, F., Giordano, S. and Cecconi, J., 2014, May. 1 GHz automatic 2-Port Vector Network Analyzer using common laboratory instruments. In 2014 IEEE International Instrumentation and Measurement Technology Conference (I2MTC) Proceedings (pp. 170-174). IEEE.

[49]. Miller, N. and Piazza, G., 2013, July. Vector network analyzer measurements of frequency fluctuations in aluminum nitride contour-mode resonators. In 2013 Joint European Frequency and Time Forum & International Frequency Control Symposium (EFTF/IFC) (pp. 666-669). IEEE.

[50]. Gupta, S., Sharma, A., Tomar, M., Gupta, V., Pal, M., Guo, R. and Bhalla, A., 2012. Piezoresponse force microscopy and vibrating sample magnetometer study of single phased Mn induced multiferroic BiFeO3 thin film. Journal of Applied Physics, 111(6), p.064110.

[51]. Chen, Y.C., Prokleška, J., Xu, W.J., Liu, J.L., Liu, J., Zhang, W.X., Jia, J.H., Sechovský, V. and Tong, M.L., 2015. A brilliant cryogenic magnetic coolant: magnetic and magnetocaloric study of ferromagnetically coupled GdF_3. Journal of Materials Chemistry C, 3(47), pp.12206-12211.

Chapter 3

Growth assessment and scrutinize dielectric reliability of AlN thin films


भारतीय प्रौद्योगिकी संस्थान रुड़की
INDIAN INSTITUTE OF TECHNOLOGY ROORKEE

CHAPTER 3

GROWTH ASSESSMENT AND SCRUTINIZE DIELECTRIC RELIABILITY OF AlN THIN FILMS

3.1. Growth assessment and scrutinize dielectric reliability of AlN thin films

3.1.1. Introduction

The III-V group nitride materials are of substantial interest in the fields of microelectronics and nano/micro electro-mechanical systems (N/MEMS) **[1]**. Among them, aluminum nitride (AlN) is commonly used in the complementary metal-oxide-semiconductor (CMOS) industry because of its unique electronic and piezoelectric properties **[2]**. AlN has a wide bandgap (Eg ~ 6.2eV), a high thermal conductivity (320 $Wm^{-1}K^{-1}$), a high intrinsic resistance, a high dielectric strength and a high acoustic velocity ~ 8000 ms^{-1} **[3-5]**. Such diverse properties make AlN a suitable candidate for a highly efficient insulating layer capable of reducing the self-heating effect in microelectronics devices **[6]**. However, Low leakage current, dielectric reliability and high breakdown field strength are of utmost importance as they greatly influence the propagation velocity, signal degradation, cross talk effects in high-frequency integrated circuit **[7,8]**. Therefore, research is being undertaken to explore and enhance the dielectric and piezoelectric response of AlN thin films to meet the optimum demand. In the specific cases, the dielectric and piezoelectric properties of AlN films are reported to strongly depend on the crystal structure, preferential orientation of the c-axis, defects and polar distribution of the grains **[9,10]**. There are plentiful ways to enhance the transport properties of thin films. The process of fabrication is one of the parameters utilizing which improved electrical properties of AlN can be achieved. It is well reported that the dielectric properties of AlN thin films fabricated using the sputtering technique are superior compared to films grown using other techniques such as metal organic chemical vapour deposition and plasma-enhanced chemical vapor deposition **[11]**. Therefore, many researchers carried out various studies on the film grown by sputtering techniques **[12-14]**.

Several groups have attempted to advance the electrical properties of the AlN films by eliminating the structural defects and out-diffusion of impurities by post-deposition heat treatments **[15]**. Moreover, most of the devices, based on dielectric properties, requires the fabrication of conducting material which serves as an underlying electrode on which the insulating material is deposited. The AlN thin film properties strongly depend on the texture and smoothness of the substrate material, thus demand a study on the effect of different bottom electrodes **[16]**. There are several metals available as bottom electrodes for deposition of wurtzite structured AlN thin films, such as Al, Pt, Ti, Mo etc. But only limited work has been done on the study of dielectric behavior of AlN with Al or another bottom electrode. Al is used for its low resistivity and high-quality factors **[17,18]**. Ti and Pt exhibit many advantages for microelectronics such as excellent electric conductivity, thermal stability, high hardness, high melting point and extraordinary chemical resistivity **[19]**. However, to date, the effect of different underlying electrodes on the electrical properties such as dielectric reliability, dielectric breakdown strength and leakage current is not fully investigated.

Within this frame, our work aim is to investigate the impact of Al, Pt and Ti bottom electrodes on the dielectric properties and leakage current behavior of AlN thin films. These properties are crucial for the incorporation of this material in electronics devices, where the bilayer (electrode/AlN) films have to be implemented for electrical and piezoresponse application.

3.1.2. Experimental details

The AlN thin films (~200 nm) were deposited on prefabricated Al, Pt and Ti coated p-type Si (100) substrates by reactive DC magnetron sputtering system (Excel Instruments, India) using high purity Al (99.99%) target. The details of the fabrication of lower electrodes are provided as supplement details [S1]. Initially, the substrates were cleaned thoroughly using a mixture of trichloroethylene and distilled water in an ultrasonic bath and then washed in Isopropyl alcohol. Before to deposition of AlN layer, the sputtering chamber was evacuated for a duration of 5 h to obtain a base vacuum of 6×10^{-7} Torr using a series combination of rotary and turbo-molecular pump. The target was pre-sputtered for 10 min in pure Argon gas atmosphere to establish the same state of Al target in every run. AlN films were deposited with a 110W DC power over metal coated Si substrates for 15 min in 70% (Ar) and 30% (N_2) atmosphere. During the complete process, the substrate temperature was kept constant at 450° C. No post-annealing treatments were performed after deposition.

The phase formation and crystalline structure of fabricated AlN films were characterized by Grazing Angle X-ray diffraction (GIXRD, Bruker advanced D-8 tools). The surface morphology and interface study of these thin films were examined by high-resolution field emission electron microscope (FE-SEM, FEI quanta 200F). The piezoelectric response of AlN thin film was recorded using piezo force microscope (PFM), which is an atomic force microscope (AFM, Bruker). During PFM measurement, a platinum-iridium coated silicon tip of radius 25 nm is brought in contact with the insulating film (AlN) and is used as a top electrode. A pre-set DC voltage from -12V to +12V is then applied on the PFM cantilever tip to maintain a homogeneous external electric field within the insulator. For further electrical characterizations, the samples were transformed into thin-film capacitor geometry by making the top electrode. The nature of electrodes may affect the electrical properties of metal-insulator-metal (MIM) structure depending on the work function of electrode materials. It is also evident that electrode-film interfaces have a relative impact on the overall resistance of MIM nanostructure **[20]**. Cu metallization has received tremendous interest in its integration with high-performance digital circuits and high-speed analog circuits due to its low resistivity, high Q performance and feasibility of thick and fine patterning **[21]**. Therefore, Cu was sputter deposited on the surface of AlN thin film of all the samples through a 200 µm diameter shadow mask to make capacitor type geometry. The frequency and electric field dependent dielectric constant (ε_r) and dielectric loss (*tan δ*) of AlN thin films were recorded by Agilent 4294 impedance analyzer. Whereas, the polarization hysteresis loops of fabricated AlN thin films were measured using ferroelectric tester (Precision Premier II, Radiant Technology). Leakage current and breakdown voltage measurements were performed using Standard semiconductor characterization system (Keithley SCS 4200).

3.1.3. Results and discussion.

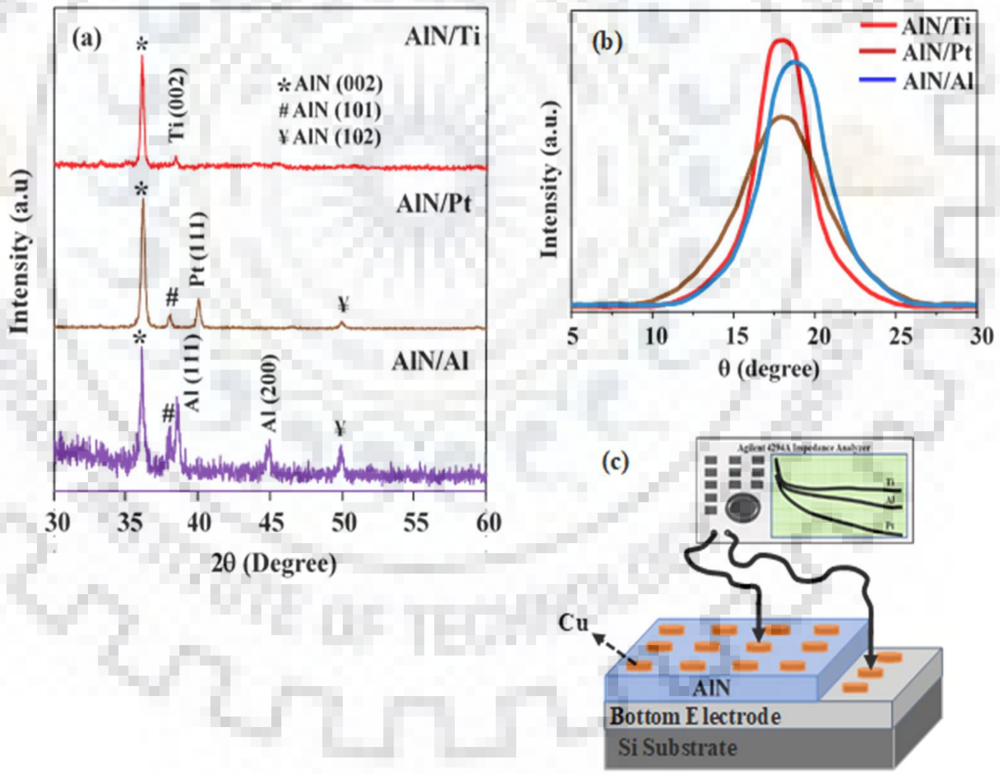

Figure 3.1 X-ray diffraction patterns of AlN/Al, AlN/Pt and AlN/Ti samples. (b) Rocking curves of AlN thin films. (c) Schematic of the methodology used for electrical characterization of the samples.

Figure 3.1(a) shows the room GAXRD pattern of AlN/Al, AlN/Pt and AlN/Ti samples. The measurements were performed in θ–2θ geometry over a 30-60˚ angular (2θ) range at a very slow scan speed of 0.5°/min using CuK$_\alpha$ (1.54 Å) radiations. The XRD pattern **[figure 3.1(a)]** of AlN/Al sample shows an appearance of (101) and (102) reflections along with dominant (002) reflection corresponding to AlN wurtzite phase. It also includes two more reflections at $2\theta \sim 38.4^\circ$ and 44.8˚, which corresponds to Al bottom electrode with (111) and (200) planes respectively. A similar diffraction pattern is observed for AlN/Pt sample, as shown in **figure 3.1(a)**. It also shows a reflection corresponding to (111) plane of Pt electrode at $2\theta \sim 40^\circ$. In contrast to AlN films deposited over Al and Pt electrodes, AlN/Ti sample shows only a single (002) reflection (c-axis) of AlN wurtzite structure [**figure 3.1(a)**]. The peak appearing at $2\theta \sim 38^\circ$ in AlN/Ti is related to (002) orientation of Ti lower electrode, which has promoted the c-axis growth of top AlN thin films.

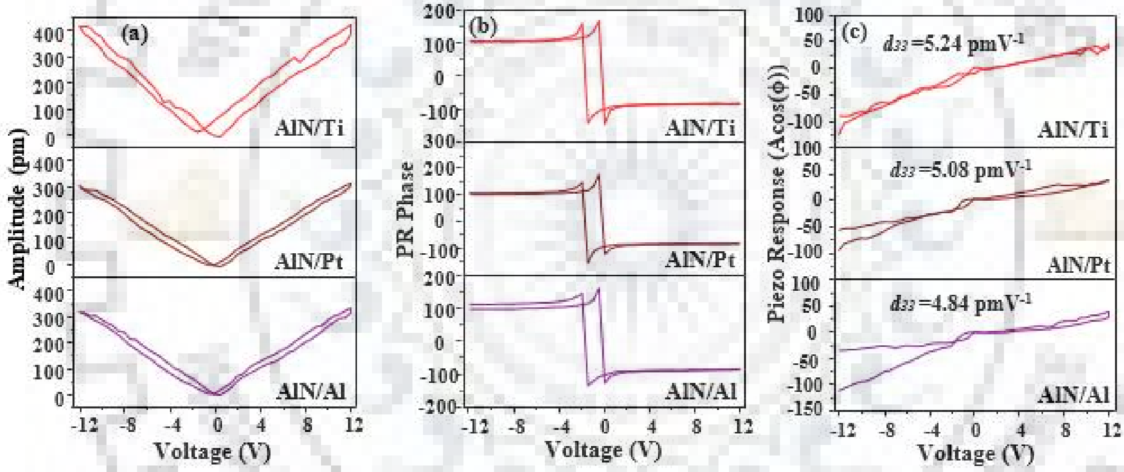

Figure 3.2 (a) electrical hysteresis, (**b**) mechanical hysteresis and (**c**) Piezoresponse vs bias voltage curves of AlN/Al, AlN/Pt and AlN/Ti samples.

The Ti metal is an ideal electrode due to close matching of its lattice parameters (a =2.951 Å, c = 4.683 Å) with top AlN layer (a = 3.113 Å, c = 4.979 Å), thus reducing the lattice mismatch. Ti serves not only as a good seed layer but also exhibits numerous advantages such as thermal stability, extraordinary chemical resistivity and high hardness **[22]**. The X-ray rocking curve analysis gives a window to determine the crystalline quality of the textured thin films. The rocking curves of the AlN films sputtered on Al, Pt and Ti, coated silicon substrate along (002) plane are shown in **figure 3.1(b)**. The full width at half maximum (FWHM) values for AlN films along c direction on Al, Pt and Ti coated silicon substrate are ~5.45°, ~7.70° and ~4.70°respectively. A lower value of FWHM implies the highly textured thin film with good crystalline perfection, and randomness in orientation distribution is less **[23]**. Therefore, the AlN/Ti sample exhibiting the lowest FWHM value is highly textured, well oriented and highly crystalline compared to other AlN films grown on Al and Pt coated Si substrates. **Figure 3.1 (c)** shows the cartoon diagram of AlN thin films and a setup utilized for measuring electrical properties.

The PFM technique was used for studying the piezoresponse of fabricated AlN thin films (**figure 3.2**). The AlN is piezo and pyro-electric material in its wurtzite state. A polarization bound surface charges get induced on the AlN surface whenever there is a divergence in the spontaneous polarization **[24]**. The graphical representation of PFM study, i.e. amplitude vs electric field and phase vs electric field graphs of samples AlN/Al, AlN/Pt and AlN/Ti are shown in **figure 3.2 (a)** and **figure 3.2 (b)**. The measurements were performed over the range of -12 V to +12 V. This piezoelectric amplitude (A), and piezoelectric phase (ϕ) variations are used for the calculation of longitudinal piezoelectric coefficient by plotting Acos(ϕ) versus bias voltage as shown in **figure 3.2(c)**. The slope ($(\Delta Acos(\phi))/\Delta V$) of **figure 3.2 (c)** gives the piezoelectric coefficient (d_{33}) of the thin AlN film. However, the calculated piezoelectric coefficient is not real as it includes the contribution of non-piezoelectric Si substrate also. Therefore, to remove the effect of the substrate, the real (effective) piezoelectric coefficient (d_{33eff}) was calculated using equation (eq. 1) **[25]**.

$$d_{33eff} = d_{33} - 2d_{31}\frac{s_{13}^{E}}{(s_{11}^{E} + s_{12}^{E})} \tag{3.1}$$

Where s_{ij} are the mechanical compliance coefficients of thin film and d_{31} is the value of the unclamped transverse piezoelectric coefficient of the film. The standard values of coefficients s_{11}, s_{21}, s_{31} and d_{31} for AlN thin film were taken from Lueng et al. **[26]** as 3.0, -0.9, -0.6, and -d_{33}/2 respectively. The value of d_{33eff} for AlN/Al, AlN/Pt and AlN/Ti were found to be ~4.84 pmV^{-1}, ~5.08 pmV^{-1} and ~5.24 pmV^{-1} respectively. These measurements were performed by using PFM cantilever tip as the top electrode. In PFM, the radius of the tip apex is in the range of tens of nanometers. Therefore, the measured piezoelectric response is grain dependent. Hence, films with larger grain size, i.e. AlN/Ti show better piezoelectric properties as compared AlN grown on other electrodes. High c-axis orientation and the absence of unwanted plane are other factors which affect the piezoresponse of films **[27]**. Thus, another reason for better response in case of AlN/Ti structure is its high c-axis orientation as compared to other electrodes.

Figure 3.3 (a) shows frequency dependent dielectric constant (ε_r) and dielectric loss (*tan δ*) of AlN/Al, AlN/Pt and AlN/Ti samples. The measurements were performed over the frequency range of 1kHz to 1MHz with an oscillation level of 500 mV. The dielectric constant (ε_r) of all the samples decreases with the increase in frequency. This decrement in dielectric constant is linked to the inertia possessed by charges which resist the instantaneous switching of polarization on an application of electric field as explained by Maxwell–Wagner and Koop's phenomenological theory **[28]**. The rapid decrement in the value of dielectric constant for lower frequency likened to higher frequency is ascribed to charge accumulation effect. A dielectric constant of ~ 8.32, ~ 8.25 and ~ 8.63, were observed for AlN/Al, AlN/Pt and AlN/Ti samples respectively at a frequency of 1MHz.

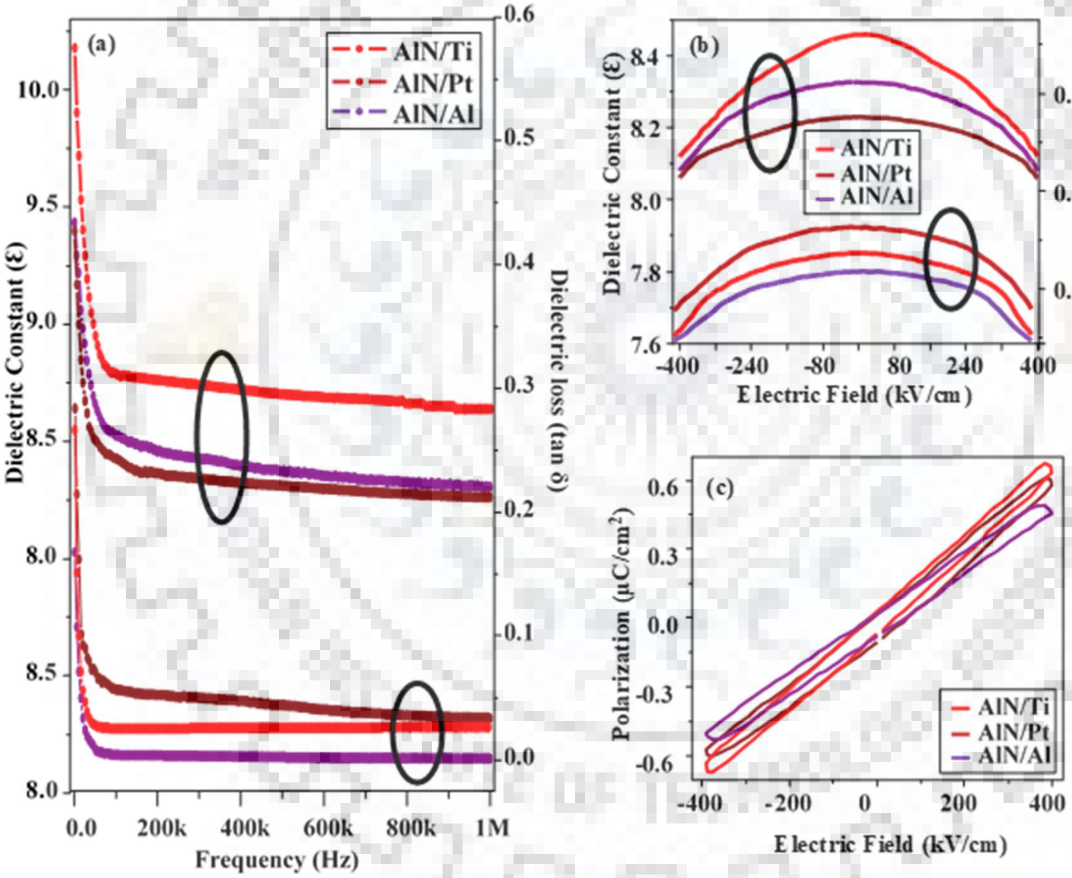

Figure 3.3. Variation of dielectric constant (ε) and dielectric loss (tan δ) of AlN/Al, AlN/Pt and AlN/Ti samples as a function of **(a)** frequency and **(b)** Electric field. **(c)** Room temperature measurement of the polarization hysteresis loop of fabricated samples.

Among all the films, AlN/Ti sample shows the highest value of dielectric constant. In general, the dielectric constant of a material depends on several factors. These factors can be classified as intrinsic and extrinsic contributions **[29, 30]**. The film orientation, dielectric behavior of a single domain and grain size contribute majorly to intrinsic factors. Whereas, Extrinsic contribution includes (i) the interface that existed between piezoelectric and electrode. (ii) mechanical stress/strain from the substrate. However, a large section of researchers suggests that high c-axis orientation along with a smooth, uniform, and crack-free microstructure plays a key role in deciding the dielectric constant of a piezoelectric thin film **[31]**. Hence, larger grain size and highly c-axis orientation are responsible for a high dielectric constant in AlN/Ti sample. To further explore the dielectric properties of AlN/Al, AlN/Pt and AlN/Ti samples, the variation of dielectric constant and dielectric loss with an electric field (E) are measured at 1 MHz (**figure 3.3 (b)**). In contrast to previous reports, our AlN samples show the non-linear variation in the dielectric response with applied electric field **[32]**. This behavior of our AlN samples is quite similar to ε-E response of ferroelectric thin films. Thus, this non-linearity can also be linked with the occurrence of polar nano regions (PNRs). The small polar nano regions are few nm or less in size and locally polarized. These PNRs are embedded in the matrix of the AlN structure. The dipole moments of PNRs are randomly different, and it may be difficult to observe it on the macroscopic scales, and the whole crystal remains in its state. However, these PNRs are affected by the electric field and cause some change in the dielectric constant, as shown in **figure 3.3 (b) [33-35]**.

Figure 3.3 (c) shows the polarization hysteresis loop evolution of AlN thin films at room temperature. A bipolar sinusoidal waveform of magnitude 400 kV/cm and frequency 1 MHz was used for analyzing the electrical hysteresis loops. The non-saturated and almost zero remnant polarization characteristic again validates the dielectric nature of all AlN thin films. The difference in the hysteresis behavior of AlN/Al, AlN/Pt and AlN/Ti is associated with the difference in leakage PNR current, variation in grain size and c-axis growth **[29]**. It is well known that grain size dependent on domain nucleation, domain structure and domain mobility greatly influence the polarization behavior. The grain boundaries act as a pinning centre for polarization and become a hindrance for polarization switching. Therefore, polarization switching is much easier for larger grains. A remnant polarization ($2P_r$) ~ 0.09 μC/cm^2, 0.11 μC/cm^2 and 0.10 μC/cm^2 and coercive field ($2E_c$) ~ 80.7 kV/cm, 79.6 kV/cm and 58.4 kV/cm are obtained for AlN/Al, AlN/Pt and AlN/Ti respectively.

Leakage current can play a valuable role in the practical application of devices for reducing the dielectric loss to a large extent **[36]**. **Figure 3.4 (a)** shows the variation of current density (J) with an applied electric field (E), plotted in semi-logarithmic scale. The J-E curves of all the samples were recorded in ± 600 kV/cm electric field range. The close examination of semi-logarithmic *J-E* curves, reveals that there is symmetry in the graph for both forward and reverse bias which suggests the creation of ohmic contact with mostly bulk limited conduction current in all fabricated samples [37].

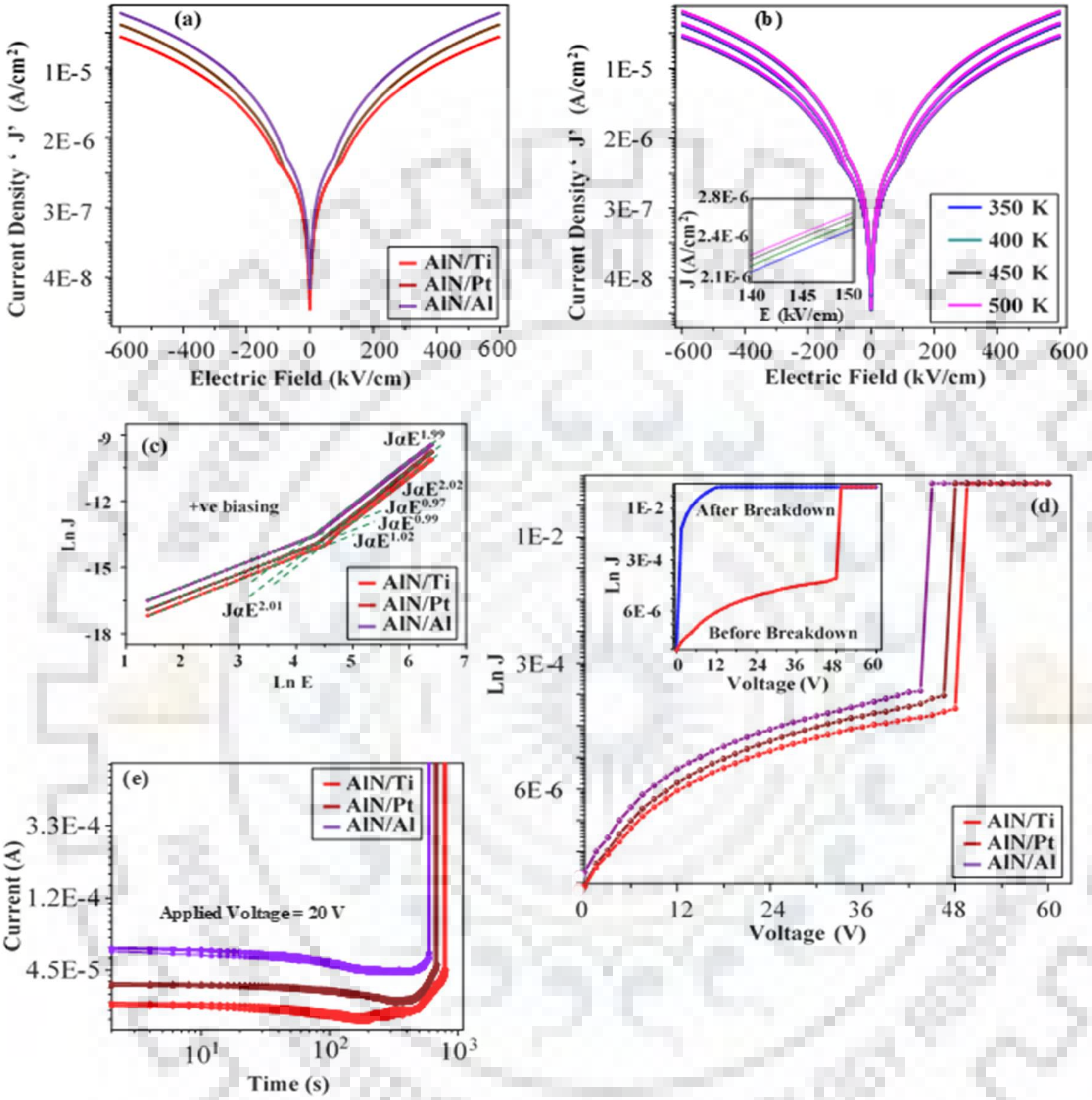

Figure 3.4. Semi logarithmic plots of current density (*J*) as a function of an applied electric field (a) At a constant temperature and **(b)** At different temperatures. **(c)** Log (*J*) vs log (*E*) plots of samples. **Inset (b)**: Enlarged *J-E* curve of AlN/Ti Structure. **(d)** Measurement characteristic of breakdown events of fabricated samples. **Inset (d)**: *I-V* characteristic of before and after the breakdown of the AlN/Ti sample. **(e)** Current vs time curves under the same electric fields for different samples.

The current-voltage (*J-E*) characteristic of all three samples was measured at different temperatures **(figure 3.4(b))** in the same electric field range to confirm the conduction mechanism in all AlN thin films. Inset of **figure 3.4(b)** shows the enlarged view of *J-E* characteristics of AlN/Ti structure. The invariability of *J-E* curves with temperature eliminates the possibility of any thermally activated process such as interface governed Poole-Frenkel emission and bulk controlled Schottky conduction **[38]**. To further investigate the conduction mechanism in AlN thin films, the *J-E* curves were fitted according to power law $J \propto E^n$. **Figure 3.4 (c)** shows the *J-E* curves of all samples in logarithmic scale. In **figure 3.4(c)** almost every *J-E* curve can be divided into two different regions according to their slopes. For low field region (< 70 kV/cm), the slopes are close to 1, which is a reflection of Ohmic conduction. For high field region (> 70kV/cm), the slopes of curves correspond to space charge limited conduction (*SCLC*) (de-trapped carriers and/or free charges from the electrode) as slopes become ~2. For films with deep traps, the SCLC equation provides the *J-E* relation with an ohmic behavior ($J \propto E$) at lower fields. When the electric field is increased beyond the trap free level, the current injection is mainly due to the excess charges present in the conduction band and the current density at the trap free limit is governed by the Child's law **[39]**, described as:

$$J = \frac{9\mu\varepsilon\varepsilon_0 E^2}{8L} \tag{3.2}$$

where, L is the total thickness of the film, μ is the mobility of the charge carriers, ε and ε_o are the optical dielectric constant and static dielectric constant respectively. Traps in the bandgap can act as a source for space-charge regions. Space charge limited effects take place when the injected free carrier density, n_i, from the electrodes to the dielectric is higher than the volume generated free carrier density (n_o), in the dielectric. The value of exponential 'y' were found to be ~ 0.97, ~ 0.99 and ~ 1.02 for AlN/Al, AlN/Pt and AlN/Ti samples respectively for low electric field regime (E < 70 Vcm^{-1}) whereas for higher E-field regime (E > 70Vcm^{-1}) the value of y was found to be ~ 1.99, ~ 2.01, ~ 2.02 for AlN/Al, AlN/Pt and AlN/Ti structures respectively.

On comparing all the samples, a minimum leakage current density of ~10^{-8}A/cm^2 at 0 kV/cm was observed for AlN/Ti sample. The (i) extent of preferential c-axis growth, (ii) formation of highly dense uniform grains and (iii) low surface roughness usually causes low leakage current. Also, researchers have observed that as the roughness of the bottom electrode is increased, the leakage current in the thin film also increases. It could be ascribed to the fact that the rougher surface has a spike-like surface which shows a more positive effect on the injection of charge carriers **[40]**. Moreover, the variation in grain size (grain boundaries) could be a reason for dissimilarity in the current density in our samples. However, it is difficult to finalize whether the flow of charge carrier is through grains or grain boundaries, but researchers suggest that the large fraction of the current flow through the grain boundaries **[41]**.

The electrical breakdown property is a very crucial factor in deciding the long-term device reliability and life. Commonly, the breakdown voltage is defined as the voltage (U_b) just above which there is a sharp increase in current (several orders of magnitude). Accordingly, the current corresponding to U_b is known as breakdown current (I_b). The breakdown characteristics of fabricated AlN thin film on Al, Pt and Ti bottom electrodes are summarized in **figure 3.4 (d)**. The complete breakdown mechanism can be divided into three modes. The first mode is attributed to the intrinsic breakdown in a defect-free dielectric thin film. The second mode is caused by microscopic defects such as trapped charges or local inhomogeneities in the thickness of the film and third mode of breakdown occurs due to macroscopic defects such as pinholes or crack in the thin film **[42]**. Since the FE-SEM images (**figure 3.4 (a-c)**) revealed the pinhole-free and dense microstructure of our thin films so it is justified to conclude that the first and second modes may be responsible for breakdown phenomenon. Moreover, it is well reported in the literature that the breakdown voltage of films deposited using sputtering is generally more when compared with films grown using other techniques **[43]**. In our case, the breakdown voltage of AlN/Al, AlN/Pt and AlN/Ti was found about ~2.1 MV/cm, ~ 2.3 MV/cm and ~ 2.4 MV/cm respectively. The images in the inset of **figure 3.4 (d)** show the *I-V* characteristic before and after the breakdown of AlN/Ti thin films. The films showed a pure ohmic nature of current below the compliance current after the breakdown.

To further explore the dielectric reliability of the deposited AlN thin films, the time dependent dielectric breakdown (TDDB) characteristics of these thin films is also studied. **Figure 3.4 (e)** depicts the TDDB characteristics of AlN thin films on different substrates under the same electric field (1MV/cm) at room temperature. Initially, all samples show small variation in the current with time but then current increased abruptly during the breakdown. The cause of this variation could be trapped charges or vacancies in the AlN thin film **[44,45]**. The obtained breakdown time was different for all the samples. The dielectric breakdown time for AlN films on Al, Pt and Ti substrate is shown in **figure3.4(e)**.

3.1.4. Conclusion

In conclusion, AlN thin films were successfully fabricated on underlying Al, Pt and Ti electrodes using reactive DC magnetron sputtering technique. It was found that the degree of orientation of top insulating AlN films strongly depends on the crystallographic structure and texture of the bottom electrodes. To be precise, Ti electrode having the least mismatch with AlN is found to be the best option for the growth of (002) oriented AlN film. A PFM technique was used to measure the polarity distribution of AlN thin films. The magnitude of the d_{33eff} is found to be ~ 5.24 pm/V^{-1} for AlN/Ti structure. It was also found that dielectric properties and leakage current strongly depends on the texture and grain size of the AlN film. The AlN thin film grown on Ti exhibits better dielectric properties and low leakage current compared to films grown on Al and Pt. These findings along open a new window for the application of AlN thin films in tunable microwave devices.

3.2. References

[1]. Tadigadapa, S. and Mateti, K., 2009. Piezoelectric MEMS sensors: state-of-the-art and perspectives. Measurement Science and technology, 20(9), p.092001.

[2]. Ambacher, O., 1998. Growth and applications of group III-nitrides. Journal of Physics D: Applied Physics, 31(20), p.2653.

[3]. Mednikarov, B., Spasov, G. and Babeva, T., 2005. Aluminum nitride layers prepared by DC/RF magnetron sputtering. Journal of Optoelectronics and Advanced Materials, 7(3), pp.1421-1427.

[4]. Hahn, B.D., Kim, Y., Ahn, C.W., Choi, J.J., Ryu, J., Kim, J.W., Yoon, W.H., Park, D.S., Yoon, S.Y. and Ma, B., 2016. Fabrication and characterization of aluminum nitride thick film coated on aluminum substrate for heat dissipation. Ceramics International, 42(16), pp.18141-18147.

[5]. Deger, C., Born, E., Angerer, H., Ambacher, O., Stutzmann, M., Hornsteiner, J., Riha, E. and Fischerauer, G., 1998. Sound velocity of $Al_xGa_{1-x}N$ thin films obtained by surface acoustic-wave measurements. Applied Physics Letters, 72(19), pp.2400-2402.

[6]. Heo, Y.J., Kim, H.T., Kim, K.J., Nahm, S., Yoon, Y.J. and Kim, J., 2013. Enhanced heat transfer by room temperature deposition of AlN film on aluminum for a light emitting diode package. Applied Thermal Engineering, 50(1), pp.799-804.

[7]. Pecht, M., Agarwal, R., McCluskey, F.P., Dishongh, T.J., Javadpour, S. and Mahajan, R., 1998. Electronic packaging materials and their properties. CRC press.

[8]. Kaletta, U.C., Wolansky, D., Wipf, M.F.C. and Wenger, C., 2014. Crosstalk suppression of CMOS compatible AlN based SAW devices on low resistive Si (100). physica status solidi (c), 11(2), pp.249-252.

[9]. Chang, C.T., Yang, Y.C., Lee, J.W. and Lou, B.S., 2014. The influence of deposition parameters on the structure and properties of aluminum nitride coatings deposited by high power impulse magnetron sputtering. Thin Solid Films, 572, pp.161-168.

[10]. Kamohara, T., Akiyama, M., Ueno, N., Nonaka, K. and Kuwano, N., 2007. Influence of aluminum nitride interlayers on crystal orientation and piezoelectric property of aluminum nitride thin films prepared on titanium electrodes. Thin Solid Films, 515(11), pp.4565-4569.

[11]. Song, X., Fu, R. and He, H., 2009. Frequency effects on the dielectric properties of AlN film deposited by radio frequency reactive magnetron sputtering. Microelectronic Engineering, 86(11), pp.2217-2221.

[12]. Acharya, J., Goul, R., Romine, D., Sakidja, R. and Wu, J., 2019. Effect of Al_2O_3 Seed-Layer on the Dielectric and Electrical Properties of Ultrathin MgO Films Fabricated Using In Situ Atomic Layer Deposition. ACS applied materials & interfaces, 11(33), pp.30368-30375.

[13]. Panda, P., Ramaseshan, R., Ravi, N., Mangamma, G., Jose, F., Dash, S., Suzuki, K. and Suematsu, H., 2017. Reduction of residual stress in AlN thin films synthesized by magnetron sputtering technique. Materials Chemistry and Physics, 200, pp.78-84.

[14]. Singh,, R. and Kaur, D., 2017. Bipolar resistive switching behavior in Cu/AlN/Pt structure for ReRAM application. Vacuum, 143, pp.102-105.

[15]. Pandey, A., Dutta, S., Prakash, R., Dalal, S., Raman, R., Kapoor, A.K. and Kaur, D., 2016. Growth and evolution of residual stress of AlN films on silicon (100) wafer. Materials Science in Semiconductor Processing, 52, pp.16-23.

[16]. Ragnarsson, L.Å., Bojarczuk, N.A., Copel, M., Gusev, E.P., Karasinski, J. and Guha, S., 2003. Physical and electrical properties of reactive molecular-beam-deposited aluminum nitride in metal-oxide-silicon structures. Journal of applied physics, 93(7), pp.3912-3919.

[17]. Akiyama, M., Nagao, K., Ueno, N., Tateyama, H. and Yamada, T., 2004. Influence of metal electrodes on crystal orientation of aluminum nitride thin films. Vacuum, 74(3-4), pp.699-703.

[18]. Felmetsger, V.V. and Mikhov, M.K., 2012, May. Deposition of smooth and highly (111) textured Al bottom electrodes for AlN-based electroacoustic devices. In 2012 IEEE International Frequency Control Symposium Proceedings (pp. 1-4). IEEE.

[19]. Doll, J.C., Petzold, B.C., Ninan, B., Mullapudi, R. and Pruitt, B.L., 2009. Aluminum nitride on titanium for CMOS compatible piezoelectric transducers. Journal of Micromechanics and Microengineering, 20(2), p.025008.

[20]. Tseng, Z.L., Chen, L.C., Li, W.Y. and Chu, S.Y., 2016. Resistive switching characteristics of sputtered AlN thin films. Ceramics International, 42(8), pp.9496-9503.

[21]. Lin, C.C., Hsu, H.M., Chen, Y.H., Shih, T., Jang, S.M., Yu, C.H. and Liang, M.S., 2001, June. A full Cu damascene metallization process for sub-0.18 μm RF CMOS SoC high Q inductor and MIM capacitor application at 2.4 GHz and 5.3 GHz. In Proceedings of the IEEE 2001 International Interconnect Technology Conference (Cat. No. 01EX461) (pp. 113-115). IEEE.

[22]. Signore, M.A., Taurino, A., Catalano, M., Kim, M., Che, Z., Quaranta, F. and Siciliano, P., 2017. Growth assessment of (002)-oriented AlN thin films on Ti bottom electrode deposited on silicon and kapton substrates. Materials & Design, 119, pp.151-158.

[23]. Pandey, A., Dutta, S., Prakash, R., Raman, R., Kapoor, A.K. and Kaur, D., 2018. Growth and comparison of residual stress of AlN films on silicon (100), (110) and (111) substrates. Journal of Electronic Materials, 47(2), pp.1405-1413.

[24]. Rodriguez, B.J., Gruverman, A., Kingon, A.I. and Nemanich, R.J., 2002. Piezoresponse force microscopy for piezoelectric measurements of III-nitride materials. Journal of crystal growth, 246(3-4), pp.252-258.

[25]. Kim, I.D., Avrahami, Y., Tuller, H.L., Park, Y.B., Dicken, M.J. and Atwater, H.A., 2005. Study of orientation effect on nanoscale polarization in $BaTiO_3$ thin films using piezoresponse force microscopy. Applied Physics Letters, 86(19), p.192907.

[26]. Lueng, C.M., Chan, H.L., Surya, C. and Choy, C.L., 2000. Piezoelectric coefficient of aluminum nitride and gallium nitride. Journal of applied physics, 88(9), pp.5360-5363.

[27]. Tonisch, K., Cimalla, V., Foerster, C., Romanus, H., Ambacher, O. and Dontsov, D., 2006. Piezoelectric properties of polycrystalline AlN thin films for MEMS application. Sensors and Actuators A: Physical, 132(2), pp.658-663.

[28]. Maxwell, J.C., 1954. Electricity and magnetism (Vol. 2). New York: Dover.

[29]. Pérez de la Cruz, J., Joanni, E., Vilarinho, P.M. and Kholkin, A.L., 2010. Thickness effect on the dielectric, ferroelectric, and piezoelectric properties of ferroelectric lead zirconate titanate thin films. Journal of Applied Physics, 108(11), p.114106.

[30]. Xu, F., Trolier-McKinstry, S., Ren, W., Xu, B., Xie, Z.L. and Hemker, K.J., 2001. Domain wall motion and its contribution to the dielectric and piezoelectric properties of lead zirconate titanate films. Journal of Applied Physics, 89(2), pp.1336-1348.

[31]. Zeng, H., Wu, Y., Zhang, J., Kuang, C., Yue, M. and Zhou, S., 2013. Grain size-dependent electrical resistivity of bulk nanocrystalline Gd metals. Progress in Natural Science: Materials International, 23(1), pp.18-22.

[32]. Sergeeva, O.N., Bogomolov, A.A., Solnyshkin, A.V., Komarov, N.V., Kukushkin, S.A., Krasovitsky, D.M., Dudin, A.L., Kiselev, D.A., Ksenich, S.V., Senkevich, S.V. and Kaptelov, E.Y., 2015. SEM, dielectric, pyroelectric, and piezoelectric response of thin epitaxial AlN films grown on SiC/Si substrate. Ferroelectrics, 477(1), pp.121-130.

[33]. Leu, C.C., Chen, C.Y., Chien, C.H., Chang, M.N., Hsu, F.Y. and Hu, C.T., 2003. Domain structure study of $SrBi_2Ta_2O_9$ ferroelectric thin films by scanning capacitance microscopy. Applied physics letters, 82(20), pp.3493-3495.

[34]. Yang, J., Chu, J. and Shen, M., 2007. Analysis of diffuse phase transition and relaxorlike behaviors in $Pb_{0.5}Sr_{0.5}TiO_3$ films through DC electric-field dependence of dielectric response. Applied physics letters, 90(24), p.242908.

[35]. Kumari, S., Ortega, N., Pradhan, D.K., Kumar, A., Scott, J.F. and Katiyar, R.S., 2015. Effect of thickness on dielectric, ferroelectric, and optical properties of Ni substituted $Pb(Zr_{0.2}Ti_{0.8})O_3$ thin films. Journal of Applied Physics, 118(18), p.184103.

[36]. Ke, G., Tao, Y., He, Z., Guo, H., Chen, Y., Dibattista, J., Chan, E. and Yang, Y., 2016. Influence of sputtering atmosphere on crystal quality and electrical properties of zirconium aluminum nitride thin film. Surface and Coatings Technology, 290, pp.87-93.

[37]. Singh, K., Singh, S.K. and Kaur, D., 2014. Strain mediated coupling in magnetron sputtered multiferroic PZT/Ni-Mn-In/Si thin film heterostructure. Journal of Applied Physics, 116(11), p.114103.

[38]. Singh, K. and Kaur, D., 2015. Quantification of charge-to-strain mediated interface coupling transfiguration in FE/FSMA multiferroic heterostructures. Journal of Physics D: Applied Physics, 49(3), p.035004.

[39]. Liu, M., Abid, Z., Wang, W., He, X., Liu, Q. and Guan, W., 2009. Multilevel resistive switching with ionic and metallic filaments. Applied Physics Letters, 94(23), p.233106.

[40]. Zhao, Y.P., Wang, G.C., Lu, T.M., Palasantzas, G. and De Hosson, J.T.M., 1999. Surface-roughness effect on capacitance and leakage current of an insulating film. Physical review B, 60(12), p.9157.

[41]. Likovich, E.M., Jaramillo, R., Russell, K.J., Ramanathan, S. and Narayanamurti, V., 2011. Scanning tunneling microscope investigation of local density of states in Al-doped ZnO thin films. Physical Review B, 83(7), p.075430.

[42]. Schneider, M., Bittner, A. and Schmid, U., 2014. Temperature dependent dielectric breakdown of sputter-deposited AlN thin films using a time-zero approach. Microsystem technologies, 20(4-5), pp.751-757.

[43]. An, Z., Men, C., Xu, Z., Chu, P.K. and Lin, C., 2005. Electrical properties of AlN thin films prepared by ion beam enhanced deposition. Surface and Coatings Technology, 196(1-3), pp.130-134.

[44]. Noguchi, J., Miura, N., Kubo, M., Tamaru, T., Yamaguchi, H., Hamada, N., Makabe, K., Tsuneda, R. and Takeda, K.I., 2003, March. Cu-ion-migration phenomena and its influence on TDDB lifetime in Cu metallization. In 2003 IEEE International Reliability Physics Symposium Proceedings, 2003. 41st Annual. (pp. 287-292). IEEE.

[45]. Loke, A.L., Wetzel, J.T., Townsend, P.H., Tanabe, T., Vrtis, R.N., Zussman, M.P., Kumar, D., Ryu, C. and Wong, S.S., 1999. Kinetics of copper drift in low- κ polymer interlevel dielectrics. IEEE Transactions on Electron Devices, 46(11), pp.2178-2187.

Chapter 4

ME coupling in AlN/FSMA heterostructures


भारतीय प्रौद्योगिकी संस्थान रुड़की
INDIAN INSTITUTE OF TECHNOLOGY ROORKEE

CHAPTER 4

MAGNETOELECTRIC RESPONSE IN AlN/NiMnIn THIN FILM HETEROSTRUCTURE.

4.1. High magnetoelectric effect in AlN/NiMnIn bilayer thin film

- **4.1.1 Introduction.**
- **4.1.2 Experimental Details.**
- **4.1.3 Results and discussion**
- **4.1.4 Conclusion**

4.2. Magneto-Dielectric response in ME multilayer encapsulating magnetostrictive film.

- **4.2.1. Introduction.**
- **4.2.2. Experimental Details.**
- **4.2.3. Results and discussion**
- **4.2.4. Conclusion**

4.3. References

4.1. High magnetoelectric coupling in Si-integrated AlN/NiMnIn thin film double layers

4.1.1. Introduction

In the current era, artificial magnetoelectric (ME) composites consist of piezoelectric and magnetostrictive materials, which are gaining more attention as they exhibit preeminent ME coupling and room temperature working as compared to single-phase natural multiferroics **[1,2]**. In these kinds of composites, the ME response is a product tensor property, i.e., the outcome of the mechanical interaction between magnetostrictive effect (magnetic/mechanical effect) occurring in the magnetic phase and the piezoelectric effect (mechanical/electrical effect) present in piezoelectric phase. The ME coupling is observed in diverse structures such as bulk ceramic, two, and three phases ME composites and nanostructured thin films **[3]**. However, the ME composite thin films have attracted enormous attention because different phases can be attached and designed at the atomic level with higher precision and sharp interface **[3,4]**. Furthermore, nanostructured thin film composites enable the researchers to investigate the physical cause of the ME coupling effect at the nanoscale level. The strength of the ME coupling depends on many factors, such as interface quality, high anisotropy magnetostriction, lattice mismatching, and functional characteristics of the individual piezoelectric and magnetostrictive layers **[5]**.

Ferromagnetic shape memory alloys (FSMAs) are a promising candidate as a magnetic layer for practical application in ME devices because they exhibit large applied magnetic field and temperature-induced strain as compared to leading magnetostrictive materials such as Trefnol-D and metglas **[6,7]**. It shows a strong magnetic field generated strain in the temperature region during martensite to the austenite phase transition. Earlier, we have reported large ME coupling in PZT/FSMA based multiferroics heterostructures **[8,9]**. Various researchers have observed ME coupling in composites based on ferromagnetic layers with ferroelectric materials such as barium titanate, polyvinylidene fluoride, lead zirconate titanate (PZT), Lead Zinc Niobate- Lead Titanate (PZN-PT), Lead Magnesium Niobate Lead Titanate (PMN-PT) **[10-14]**.

However, during their possible incorporation with functional electronic devices, these ferroelectrics based multiferroic composites have specific limitations such as significant hysteresis loss, temperature-dependent functional parameters, pyroelectric effects. In particular, research is being focused on strong ME response in AlN based structures **[15-17]**. Aluminum nitride (AlN) is found to be superior considering all factors, including its piezoelectric properties (g_{33}= ~50 mV m/N and d_{33} = ~5 pm/V), better process stability, power handling, thermal drift [**18-20**]. The deposition process of AlN is also well reproducible, and its chemical compatibility is well suited with semiconductor fabrication technology. For strong coupling between ferromagnetic and piezoelectric layers in the artificial ME heterostructure, it is desirable to fabricate high-quality thin films with a sharp interface that can be attained by several growth techniques such as MBE, PLD, MOCVD, sputtering. Among these mentioned techniques, magnetron sputtering is the simplest and best way to obtain heterostructure of these two layers, i.e., NiMnIn and AlN. Therefore, we have sputtered deposited and investigated the high ME coupling in AlN/$Ni_{50}Mn_{35}In_{15}$ ME heterostructure. Such ME heterostructure with high ME response can be useful in magnetic field sensing applications at room temperature.

4.1.2. Experimental Details

The AlN/NiMnIn thin-film heterostructures were fabricated using a DC magnetron sputtering system. Initially, Si (100) p-type substrates were cleaned with standard RCA I and RCA II methods [9]. Before thin film deposition, the system was evacuated to a base pressure of about 10^{-7} torr using a series combination of turbomolecular and rotary pumps. Initially, $Ni_{50}Mn_{35}In_{15}$ (NiMnIn) thin film with thickness ~550 nm was grown on Si substrate with pure argon working pressure of 10 mTorr at a temperature of 550 ˚C. After that, AlN thin film of thickness ~600 nm was grown ex-situ using reactive sputtering in a mixture of argon and nitrogen with a 3:2 gas ratio on pre-deposited NiMnIn underlayer. A step mask was used in such a way that the capped NiMnIn is available as a bottom electrode. The crystallographic structure and phase formation of the heterostructure were analyzed using Bruker advanced D8 X-ray diffractometer with Cu Kα (1.54 Å) source in θ-2θ geometry at a slow scan speed of 0.5 ˚/min. The cross-sectional microstructure of the AlN film and the interface quality between the AlN film and NiMnIn layer was observed using Field Emission Scanning Electron Microscope (FESEM, Carl Zeiss, Ultra Plus). For the measurement of dielectric and magnetic properties of AlN/NiMnIn heterostructure, Ag dots were sputtered on the top of the AlN layer through a stencil mask with a 0.2 mm diameter pattern. The variation in dielectric constant with frequency and temperature was measured using HP 4294 impedance analyzer. The thermomagnetic (M-T) and isothermal magnetic properties (M-H) measurements of the heterostructure was performed using a vibrating sample magnetometer (VSM, cryogenic). The VSM was interfaced with Keithley 4200 source meter and nano-voltmeter to measure the induced ME voltage for calculating the ME coupling coefficient.

4.1.3. Results and discussion

Systematic room-temperature X-ray diffraction patterns of NiMnIn, AlN, and AlN/NiMnIn samples deposited over Si substrate are summarized in **figure 4.1 (a).** The presence of dominant (220) fundamental peak with a minor (311) reflection suggests the cubic structure of NiMnIn thin film on Si substrate [**21**]. On the other hand, a single (002) reflection of AlN film grown over Si authenticate its c-axis wurtzite structure. The XRD pattern of AlN/NiMnIn heterostructure consists of (220) reflection corresponding to the cubic austenite phase of NiMnIn and (002) reflection of AlN wurtzite structure. No peaks corresponding to any impure phase are detected, which confirm the formation of pure bilayer structure in AlN/NiMnIn heterostructure.

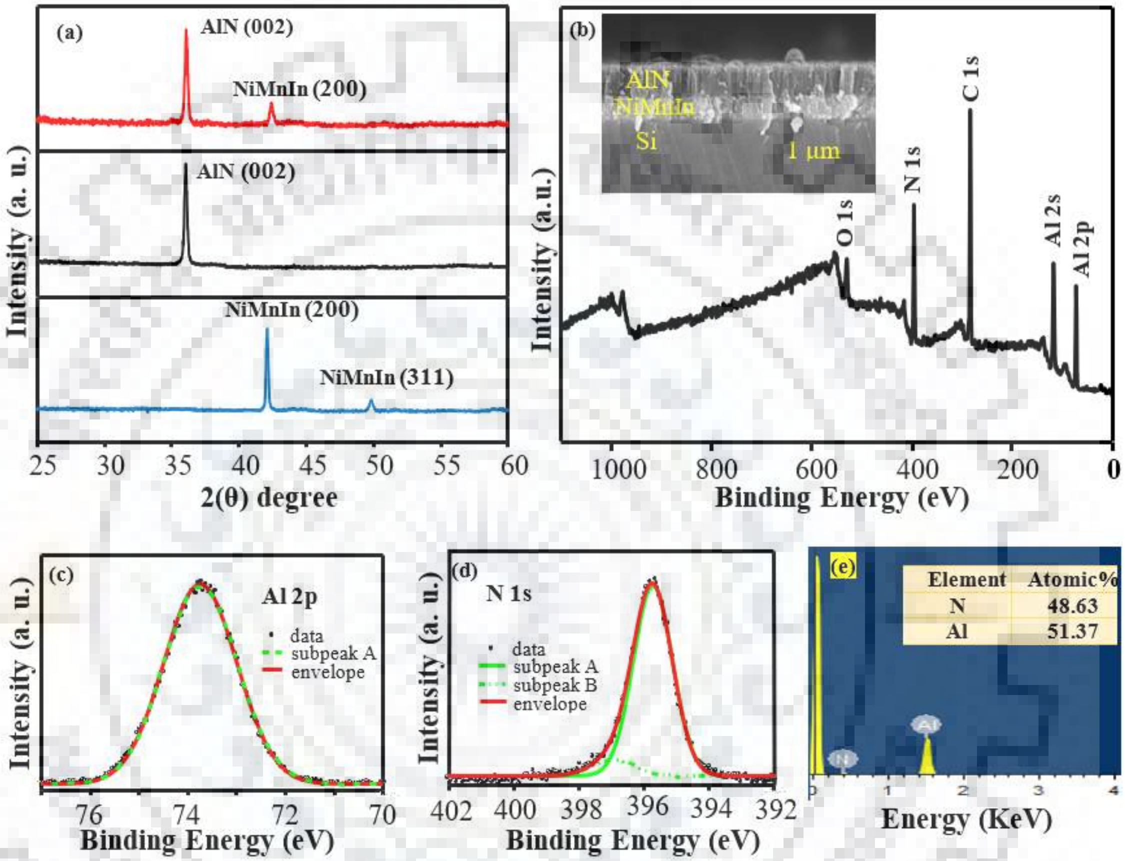

Figure 4.1 (a) Room temperature XRD pattern of NiMnIn, AlN, and NiMnIn/ AlN heterostructures fabricated on Si (100) substrates. (b) Surface scanning XPS full spectra for the NiMnIn/AlN heterostructure. The inset shows the cross-sectional FeSEM image of the Si-integrated NiMnIn/AlN heterostructure. (c) Al 2p and (d) N 1s core-level XPS spectra for the fabricated ME heterostructure. (e) EDS spectra for atomic concentration.

The preferred (002) orientation of AlN grown over NiMnIn underlayer indicates that most of the AlN crystalline grains are perpendicular to the NiMnIn surface. The cross-sectional FESEM image of NiMnIn/AlN heterostructure shows an almost clear interface between AlN and NiMnIn layers (**inset figure 4.1 (b)**). The rms value of surface roughness of NiMnIn and AlN measured by atomic force microscopy (AFM) images are about 2.7 nm and 7.3 nm, respectively.

The SEM image also depicts the columnar growth of the AlN layer over dense micro-structured NiMnIn layer. Such highly c-axis oriented columnar AlN film having a clear interface with NiMnIn exhibits excellent piezoelectric properties [**19**].

To further study the chemical states and the surface components of the AlN layer, X-ray photoelectron spectra (XPS, model PHI 5600 Versa Probe III Multi-technique system) was recorded, with Al Kα (1486.708 keV) radiation as monochromatic X-ray source with a step width, pass energy and base pressure of 0.05 eV, 55 eV and 10^{-7} mbar respectively. Initially, the system was calibrated using C-1s peak at binding energy position 284.8 eV as a reference. **Figure 4.1 (b)** displays the survey scan spectrum indicate that the surface component of AlN film consists of elements like nitrogen (N-1s), aluminum (Al-2p), oxygen (O-1s), and carbon (C-1s). No other elements were observed in the survey scan, which confirms the absence of any impurity on the surface and authenticates only the AlN growth of the material. For further analysis of existing bonding, high-resolution XPS was also performed. As exhibited in **figure 4.1 (c)**, the high-resolution Al 2p XPS spectrum of the sample presents a single peak centred at 73.8 eV on the surface, which is attributed to the Al-N bonding state [**22,23**]. Also, the N-1s spectra analysis gives the added information about the chemical structure and bonding on the surface of the AlN thin film (**figure 4.1 (d)**). The high-resolution XPS spectra of N-1s contains two sub-peaks with a binding energy of 397 eV and 395.8 eV, which are the characteristics of N-Al-O and Al-N bond, respectively [**22,24**]. This XPS analysis suggests that most of the N occurs in the form of the AlN phase. With the help of the subpeak area, the calculated results of element atomic concentration for aluminum and nitrogen were found to be ~ 52.7 and ~ 47.3, respectively, which suggests the proper stoichiometry of the material.

The dielectric constant (ε) and dielectric loss (tan δ) measurement as a function of frequency by applying a small AC signal of 500 mV amplitude were carried out at room temperature. **Figure 4.2 (a)** shows the logarithmic frequency dependence of ε and tan δ of AlN/NiMnIn heterostructure in the frequency range of 1 kHz to 1 MHz. The dielectric constant exhibits a decrement with the increase in frequency. This behavior is linked to the inertia possessed by the charges which resist the instantaneous polarization switching on the application of the electric field, as explained by Maxwell-Wagner theory [**25**]. Moreover, the dielectric value decreases more quickly at a lower frequency and with a slow rate at a higher frequency, which can be ascribed to charge accumulation effect [**26**]. The NiMnIn/AlN heterostructure shows a dielectric constant of ~7.8 at 1 MHz. The variation in dielectric constant (ε) of ME heterostructure as a function of temperature has been plotted in **figure 4.2 (b)** at 1 MHz frequency with 500 mV amplitude of the oscillating electric field.

A typical hump like behavior in the dielectric constant over the temperature range between ~270 K and ~294 K is observed. This hump could be related to the fact that dislocation produced during the nucleation and growth of the martensite phase may lead to variations in the dielectric constant of the AlN layer during the transition region and ultimately settle down soon after the martensite transformation is complete.

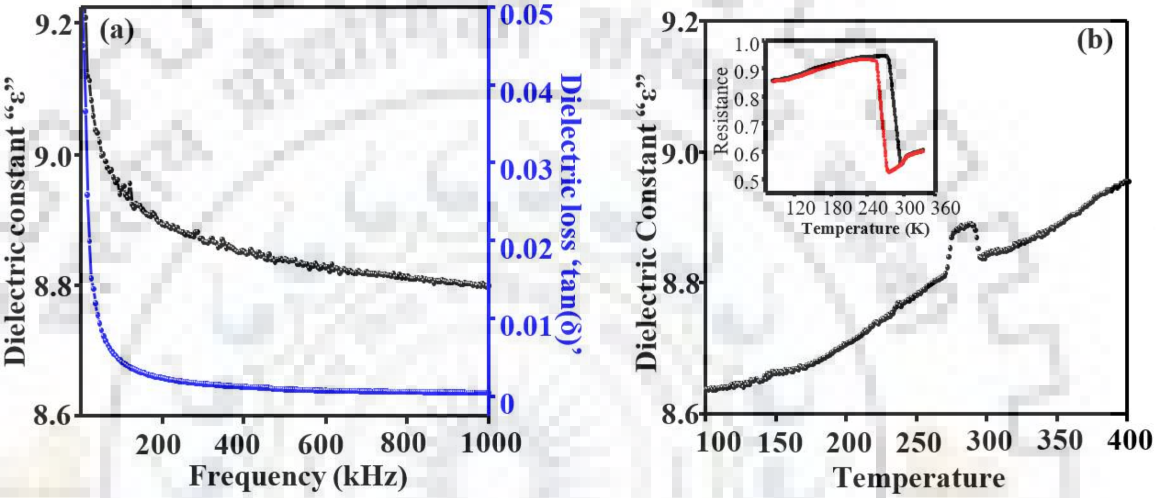

Figure 4.2. (a) Dielectric constant and dielectric loss vs frequency characteristics of the device in the logarithmic scale. (b) Temperature dependence of the dielectric constant of the ME heterostructure and (inset) resistivity behaviour of the bare NiMnIn thin film.

To further examine the martensite and austenite temperature regions, resistance versus temperature behavior of NiMnIn layer is also plotted along with dielectric constant variation in **figure 4.2 (b)**. The values for austenite start (A_s), austenite finish (A_f), martensite start (M_s), and martensite finish (M_f) were observed to be nearly 278 K, 295 K, 288 K, and 273 K respectively. These values are in accordance with the dielectric hump observed during dielectric vs temperature measurement of the AlN/NiMnIn ME heterostructure.

Figure 4.3 (a) shows the setup schematic adapted for ME measurements of AlN/NiMnIn heterostructure and the transfer of magnetic field induced strain to the piezoelectric layer. **Figure 4.3 (b)** displays the temperature dependence of magnetization (M vs T curves) at a fixed magnetic field strength of 0.05 tesla over a temperature range of 25 K to 300 K in field cooled cooling (FCC), as well as field cooled warming (FCW) modes using VSM system (Cryogenic USA). Both FCC and FCW shows decrease in the magnetization with the increase in temperature up to ~ 272 K. This decrement in the value of saturation magnetization with increment in temperature can be related to the fact that increment in the temperature gives rise to change in entropy that hampers the ferromagnetic tendency of the dipole to get align along the magnetic field direction.

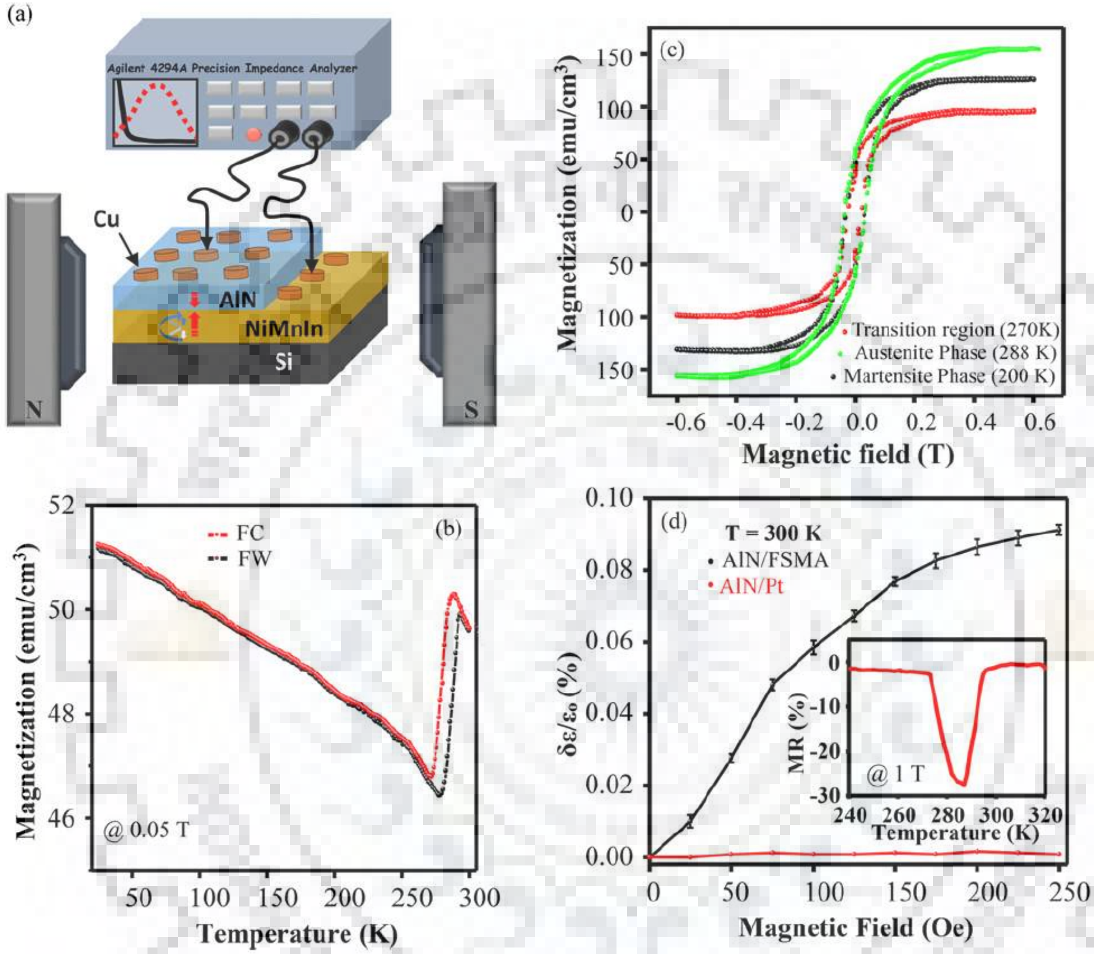

Figure 4.3. (a) Schematic diagram with a methodology adapted to perform magnetoelectric coupling measurements of the AlN/NiMnIn structure. (b) Magnetization vs temperature plots during field heating and field cooling modes. (c) Magnetic hysteresis loops of NiMnIn/AlN at the martensite phase (200 K), transition region (270 K), and austenite phase (288 K). (d) Magnetodielectric tunability as a function of the external magnetic field at room temperature and the inset shows the temperature-dependent magnetoresistance (MR) of the NiMnIn thin film.

A small hysteresis formed by FCC and FCW curve over the range of 272 K to 296 K reflects the first order martensite transformation. The lower saturation magnetization in the martensite state leads to the characteristic step type behavior in the measured M vs T curve. This sudden variation in the magnetization curve can be related to the change in Mn-Mn interatomic distance resulting in the weakening of the exchange interaction **[27]**. **Figure 4.3 (c)** summarizes the in-plane isothermal magnetic hysteresis loops of AlN/NiMnIn layered composite measured at 1 Tesla magnetic field in martensite phase (200 K), transition region (270 K) and austenite phase (288 K). The well saturated M-H hysteresis loops confirm the ferromagnetic nature of AlN/NiMnIn heterostructure at these temperatures. The ME heterostructure shows maximum saturation magnetization at 288 K compared to other measured M-H loops. These results are in complete agreement with the M-T measurement.

The combination of piezoelectric AlN and ferromagnetic NiMnIn layers gives rise to the ME effect in the fabricated heterostructure. Dielectric tunability measurements were performed in the presence of magnetic field to depict the direct ME coupling and its origin in AlN/NiMnIn heterostructure (figure **4.3 (d)**) at 300 K. The dielectric constant of AlN/NiMnIn heterostructure is altered with the applied magnetic field and shows a tunability of 0.09 at 250 Oe magnetic field. The contribution of magnetoresistance is minor because NiMnIn exhibits a small value of magnetoresistance at measurement temperature (300 K) (**Inset 4.3 (d)**) [**28**]. Therefore, this dielectric tunability can be ascribed to the magnetic field induced strain in the NiMnIn layer is transferred to the AlN coating and causes an alteration in the dielectric constant of AlN/NiMnIn heterostructure. A sample of Pt/AlN/Pt is also prepared and tested for its dielectric response in the presence of a magnetic field. The independency of the dielectric constant of Pt/AlN/Pt on the magnetic field further confirms the strain mediated ME coupling in our AlN/NiMnIn heterostructure.

To further validate the presence of ME coupling in AlN/NiMnIn heterostructure, the ME coupling coefficient ($\alpha_{ME}=dE/dH$) is measured. For α_{ME} measurement, the heterostructure was subjected to an in-plane magneto-static field (H_{dc}) with a small alternating magnetic field (H_{ac}). **Figure 4.4 (a)** shows the room temperature ME coupling coefficient as a function of H_{dc} measured at fixed H_{ac}= 2 Oe and frequency of 5 kHz. As the H_{dc} increases, α_{ME} shows a linear increase up to H_{dc} ~ 300 Oe with a maximum value of ~99.2 V/cm Oe and then decreases on further increment in H_{dc}. The ME coupling response with H_{dc} is consistent with the dependence of the piezo-magnetic coefficient q_{33} ($d\lambda/dH$) on H_{dc} [**29**]. It can be ascribed to the fact that the magnetic field induced strain in the ferromagnetic NiMnIn layer due to magnetostriction is transferred to the AlN layer through the interface and produce a ME voltage in AlN/NiMnIn heterostructure. The high value of α_{ME} in the present NiMnIn/AlN system as compared to earlier reported multiferroic heterostructure could be ascribed to the fact that the ME coupling coefficient primarily depends on piezoelectric voltage coefficient (g_{33}) instead of piezoelectric coefficient (d_{33}) [**9, 30**]. The almost linear response of α_{ME} till 300 Oe indicates the possibility of AlN/NiMnIn heterostructure application in magnetic field sensing.

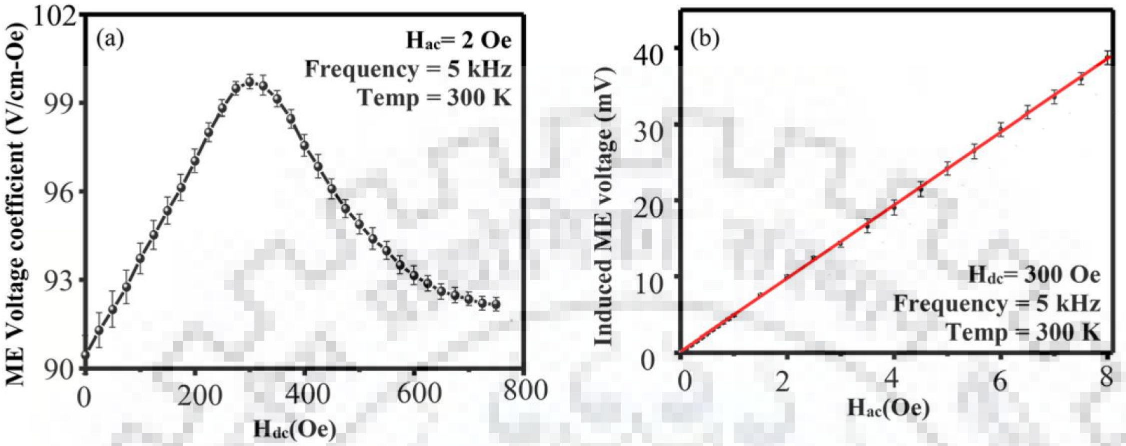

Figure 4.4. Magnetoelectric coupling coefficient **(a)** as a function of the bias field H_{dc} and **(b)** magnetoelectric voltage vs ac magnetic field (H_{ac}) plot at 5 kHz frequency and 300 Oe bias field measured at 300 K.

Furthermore, for evaluation of AC magnetic field sensitivity of the AlN/NiMnIn heterostructure, the induced ME voltage (V_{ME}) was plotted in **fig 4.4 (b)** as a function of an AC magnetic field (H_{ac}) superimposed on a DC magnetic field of 300 Oe. The curve of the V_{ME} with the AC magnetic field in the range of 8 Oe is almost linear with α_{ME} of about ~ 97 V/cm Oe at 300 K. It opens up a window for the use of AlN/NiMnIn thin-film composites for AC magnetic field detection.

4.1.4. Conclusion

In summary, Si-integrated NiMnIn/AlN magnetoelectric heterostructures were fabricated using DC magnetron sputtering. The c-axis wurtzite growth of AlN thin film over $L2_1$ structured NiMnIn under layer is revealed by the X-ray diffraction pattern and FESEM images of AlN/NiMnIn heterostructure. The presence of typical hump in dielectric value of ME heterostructure over ~ 270 K to 294 K temperature regime could be ascribed to the transfer of strain generated during the first-order structural transformation of the NiMnIn layer. The magnetoelectric measurements of AlN/NiMnIn heterostructure show a high ME coupling coefficient of ~99.2 V/cm Oe at 300 Oe bias field due to the large magnetic field induced strain in NiMnIn layer and higher piezoelectric voltage coefficient of the AlN layer. These results suggest the potential of AlN/NiMnIn ME heterostructure in magnetic field sensing and energy harvesting applications.

4.2. Magneto-Dielectric response in ME multilayer encapsulating magnetostrictive film.

4.2.1. Introduction

In recent years, magnetoelectric composites have fascinated the researchers for their applications in numerous fields such as memory devices, resonators, sensors **[31]**. These composites can be fabricated in various structures such as layered thin films, two and three-phase ME composites, bulk ceramics **[32, 33]**. Among aforesaid, layered ME structures are of great interest because they offer high degrees of freedom to control the interaction between different ferric orders with higher precision at the atomic level **[34]**. Also, the conveyance of magnetostriction across the ferromagnetic/piezoelectric (FM/PE) interface is of great technical importance because it offers fabrication of ultra-fast, power-efficient, and novel devices like miniaturized magnetic sensors and energy harvesters. There are plentiful ways to monitor magnetic field controlled electrical response such as (i) amendment in dielectric constant, (ii) variation in polarization, (iii) change in resistance due to the interfacial lattice strain at structural phase transitions of the polar phase **[35-37]**.

The dependence of dielectric properties of layered ME heterostructure on the externally applied magnetic field is termed as magneto-dielectric (MD) effect **[38]**. MD effect contributes new perspectives in the fundamental understanding of novel materials along with an extra edge for making future multifunctional devices and robust systems capable of healthy integration into existing technologies. In layered composites, the MD effect is based on the product tensor property between a piezoelectric phase and a magnetic phase by strain transfer **[39]**. Recently, MD response in LSMO and PZT layered structure was demonstrated by Kang et al. **[40]**. Greve et al. reported coupling in 2-2 structures comprising of $(Fe_{90}Co_{10})_{78}Si_{12}B_{10}$ layers and AlN **[16]**. Koo et al. reported a room temperature MD response in $BaTiO_3/\gamma\text{-}Fe_2O_3$ **[41]**. Despite significant research, the reported change in the dielectric constant lacks practical room temperature applications. Therefore, significant research is required for designing futuristic MD nanostructures for magnetic field sensing devices capable of working at room temperature. The substrate clamping can suppress the overall magnetostriction of the ME structure and hamper the device response to a large extent. One efficient way to achieve improved magnetic field modulated permittivity is by utilizing a combination of a high room temperature magnetostrictive FM layer with excellent PE materials. Another methodology to enhance the MD response in layer structures is to grow a stacked multilayered structure (FM/PEn, n>2). This approach also disentangles the substrate clamping effect **[42]**. Therefore, a combined strategy with more interfaces and incorporation of strong piezoelectric and magnetostriction materials capable of working at room temperature is an immediate remedy to obtain enhanced MD effect **[43]**. The ideal candidates for FM and PE layers are ferromagnetic shape memory alloys (like-NiMnIn, NiMnSb, etc.) and AlN, respectively. The NiMnIn exhibits giant magnetostriction coefficient at room temperature with multiple degrees of freedom to tune its magnetostriction, i.e., by varying temperature, magnetic field, stress **[44,45]**. On the other hand, Aluminum Nitride (AlN) is a lead-free complementary metal-oxide-semiconductor (CMOS) compatible piezoelectric material with a high value of voltage piezoelectric coefficient (e_{33}) **[46]**. NiMnIn, in combination with AlN, has documented strong ME coupling at room temperature **[47]**. One can expect improved dielectric constant with an enormous magneto-dielectric response, which can be valuable for practical magnetic sensors and tunable microwave devices.

In present work, we have prepared a lead-free ME 2-2 composite system with NiMnIn/AlN/NiMnIn/AlN/NiMnIn (MIMIM) multilayered heterostructure. Initially, the structural, chemical and electrical properties of the fabricated multilayered heterostructure have been investigated. Subsequently, magnetostrictive and magneto-dielectric measurements are performed on the application of an external applied magnetic field at room temperature.

4.2.2. Experimental Details

The AlN and NiMnIn thin films were sequentially deposited on a p-type Si (100) substrate using a DC magnetron sputtering system to form NiMnIn/AlN/NiMnIn/AlN/FSMA multilayered structure. Commercial targets of $Ni_{50}Mn_{35}In_{15}$ and Al (99.999% purity) were used for the deposition. Before the fabrication, the Si wafers were cleaned using the RCA method. The target was pre-sputtered for 5 min before every deposition to ensure high purity of the film. Initially, a NiMnIn layer was sputtered at 550 ˚C with a deposition pressure of 10 mTorr and power of 100 W on top of Si substrate for 4 mins. Subsequently, an AlN film was sputtered on previously deposited NiMnIn layer in a mixture of argon and nitrogen gases (ratio 14:6 sccm) with DC power supply, working pressure, and deposition temperature of 110 W, 5 mTorr and 450 ˚C respectively. This process is repeated alternatively to obtain the complete MIMIM structure that can be represented as NiMnIn (180 nm) / AlN (180 nm) / NiMnIn (50 nm) / AlN (180 nm) / NiMnIn (180 nm). All NiMnIn layers were fabricated at the same deposition parameters except the deposition time through which the thickness of the middle layer was controlled. The middle NiMnIn layer (50 nm) was deposited for a short duration of 60 secs. On the other hand, the deposition parameters for both the layers of AlN were kept the same.

X-ray diffractometer (Bruker advanced D8) was used to explore the phase formation and crystallographic structure of the fabricated multilayer structure with Cu K_{α} (1.54 Å) source. Field emission scanning electron microscopy (FESEM) imaging was used to analyze the cross-sectional interface of the fabricated heterostructure. The electrical characterization of the fabricated multilayered structure was carried out using the semiconductor characterization system (SCS-4200) and HP 4294 impedance analyzer. The surface components and chemical states were studied using X-ray photoelectron spectra (PHI 5600 Versa Probe III MT system) with Al K_α radiation as the monochromatic source. The pass energy, step width, and base pressure of Al K_α source were 55eV, 0.05eV, and 10-7 mbar, respectively. The binding energy of C-1s peak (284.8 eV) was used as a reference for the system calibration. Piezoelectric measurement of the fabricated structures was carried out with the help of a double beam laser interferometer. The backside of both the substrate was cleaned to make it highly reflecting surface for the measurement. The magnetostriction coefficient of the ferromagnetic NiMnIn layer was calculated using the cantilever method. For this, a 200 nm magnetostrictive NiMnIn film was deposited on silicon MEMS cantilever (580μm × 200μm), and imaging was performed with white light interferometry under different magnetic environment. The magnetic hysteresis (M-H) loops were recorded by cryogenic 2T vibrating sample magnetometer (VSM). The magneto dielectric measurements were performed using HP 4294 impedance analyzer interfaced with VSM in such a way that the magnetic field is applied parallel to the device surface.

4.2.3. Results and discussion

To evaluate the crystalline structure of fabricated MIMIM structure, ex-situ grazing angle X-ray diffraction (XRD) was performed in the 25˚ -70˚ range. The XRD pattern reflects two peaks located at nearly $2\theta = 36.2^\circ$ and 42.2˚, as shown in **figure 4.5(a).** The reflection at 36.2˚ corresponds to (002) plane of wurtzite AlN layer [20], and on the other hand, reflection at $2\theta \sim 42.2^\circ$ corresponds to (220) plane of cubic structured NiMnIn thin films [**8**]. These results suggest the highly textured growth of each layer in the multilayered heterostructure. In the case of AlN, this could be due to the low roughness of the underlying layers (NiMnIn), which is a crucial parameter in the orientation of AlN film growth. The (002) peak authenticate the wurtzite growth of AlN thin film normal to the NiMnIn surface.

Absence of any other peaks advocates the fabrication of pure NiMnIn/AlN/NiMnIn/AlN/NiMnIn multilayered heterostructure. **Inset figure 4.5(a)** shows the root mean square surface (RMS) roughness of about 10.14 nm for the top AlN layer. Low roughness leads to very sharp interfaces in the heterostructure and reduction in dielectric losses. To further evaluate the interface quality and thickness of the individual layers, the cross-sectional FESEM image of the fabricated multilayered structure was captured, as shown in **figure4.5 (b).** Two distinct 180 nm thick AlN layers separated by a thin layer (~50 nm) of NiMnIn can be easily observed with a visible interface.

A smooth and crack-free surface is essential for advancement in the functional properties of thin films and can influence parameters such as piezoelectric coefficient, dielectric loss, leakage current [**48**]. Also, adhesion between films and substrate can improve the stress transfer mechanism in the heterostructure.

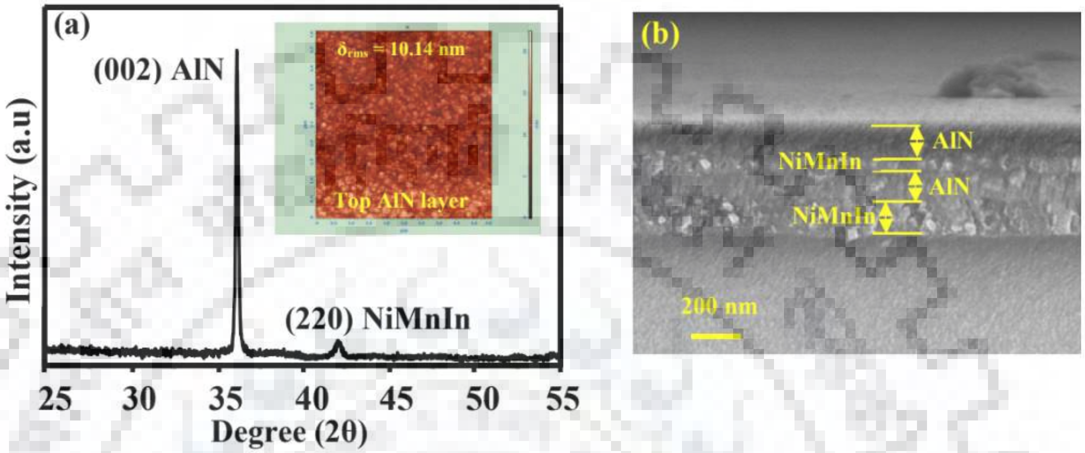

Figure 4.5 Room temperature XRD pattern of AlN/NiMnIn/AlN/NiMnIn heterostructure fabricated on Si (100) substrates. Inset shows the AFM image of the top AlN layer. (b) Cross-sectional FESEM image of the Si-integrated multilayered heterostructure.

Leakage current is a critical factor for practical applications where low leakage current is beneficial in reducing the dielectric loss of a device. For this, **figure 4.6 (a)** depicts the behavior of leakage current density (*J*) with an applied electric field (*E*) on a semi-log scale. The fabricated MIMIM layer exhibits low leakage current value in the order of 10^{-7}A under an applied voltage of 15 V, which could be associated with small roughness in the fabricated structure. The reported data reflects the use of fabricated MIMIM structure for practical electronics device applications with lower losses. **Figure 4.6 (b)** shows the variation in the dielectric constant of MIMIM structure as a function of frequency from 1 kHz to 1 MHz with a small AC signal of 500 mV at 300 K. A decline in the dielectric constant was observed with the increment in frequency. This decrement in dielectric constant can be explained by the fact that the polarization is trailed behind the applied electric field frequency [**49**].

The AlN insulator multilayered structure with an encapsulated layer shows a dielectric constant of 22.3, which is much higher (~300%) as compared to a single layer of AlN. The dielectric constant of a single layer of AlN (600 nm) deposited on the FSMA electrode is ~ 7.4 [19]. This significant value of dielectric constant for multilayers structure compared to a single layer could be related to the redistribution of negative and positive charges on the interface, which permits an improvement in polarization [**50**].

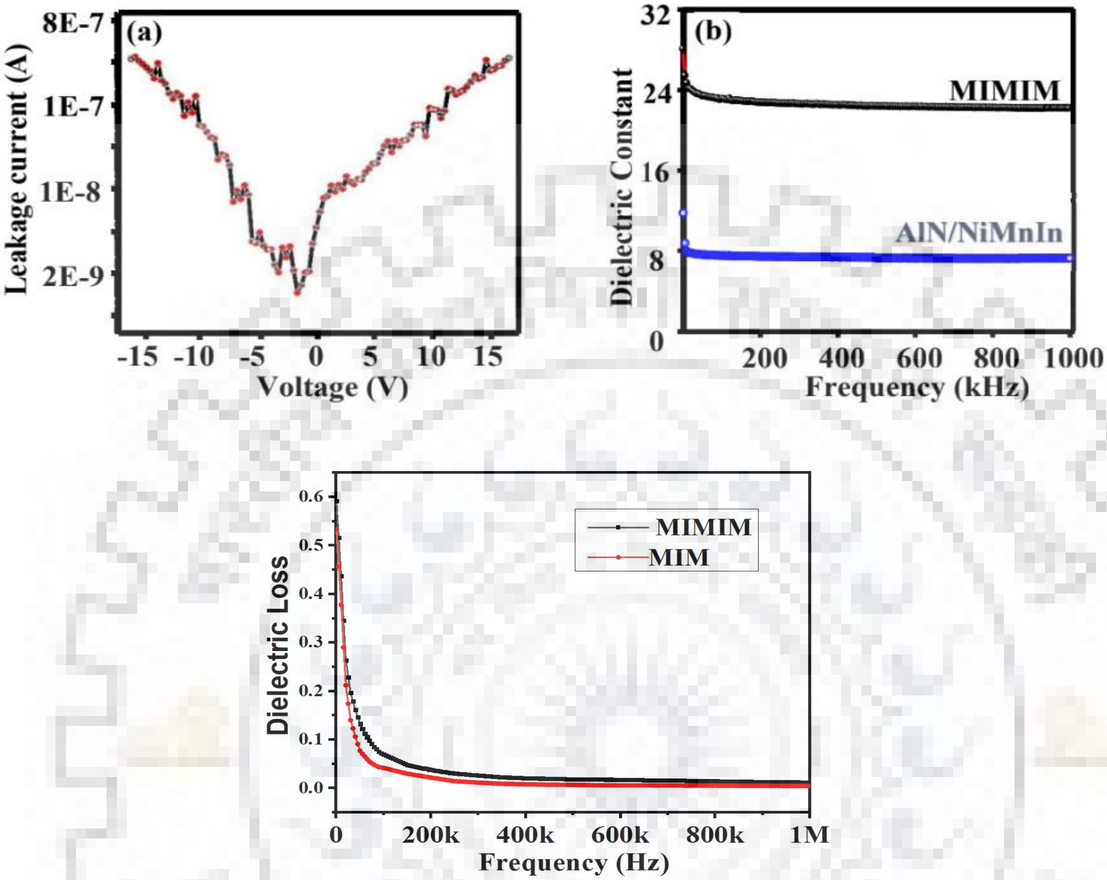

Figure 4.6 (a) Shows the leakage current measurement of the device on a logarithmic scale. (b) Dielectric constant and (c) Dielectric loss vs frequency characteristic of MIMIM and AlN/NiMnIn structure respectively.

In multilayer composites, extra charge accumulations and polarizations occur at the interfaces between adjacent layers, which leads to extra enhancement of permittivity [**51**]. Such structures can also be used to achieve higher capacitance by stacking multiple capacitors on top of each other. Also, it offers freedom for 3-D integration with an extreme large integration density by increasing capacitance density of the Metal insulator multilayer integrated capacitors in parallel configuration [**52**].

A full range XPS spectrum of NiMnIn layer was performed to understand the dielectric behavior of the fabricated structure. The survey scan XPS spectra exhibit the characteristic peaks corresponding to Ni2p, Mn2p, C1s, In3d, and O1s, as shown in **figure 4.7(a)**. The deficiency of any other contamination peak in the survey scan suggests the high purity of NiMnIn film in the structure. The C-1s peak is the instrumental peaks, and its binding energy (284.8 eV) is used as a reference for the system calibration. Furthermore, high-resolution XPS spectra of Ni2p, In3d and Mn2p were done for their corresponding individual electronic states and also used to assign the type of bonds formed.

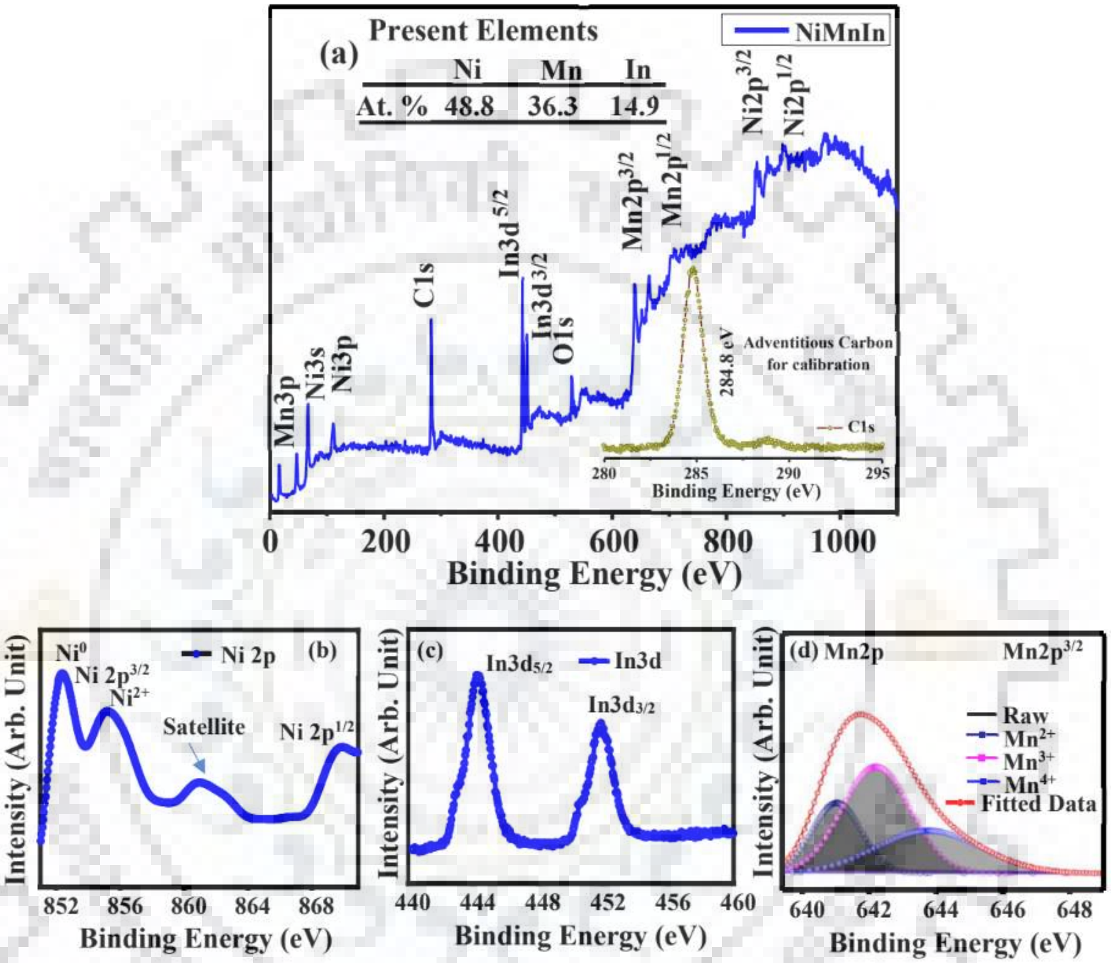

Figure 4.7. (a) Surface scanning XPS full spectra for NiMnIn (middle layer) of the heterostructure. (b), (c) and (d) Mn 2p, Ni and In core level XPS spectra for NiMnIn layer in the heterostructure.

Figure 4.7(b) depict core-level spectra of Ni2p, which contains characteristic peaks attributed to Ni2p$_{3/2}$ and Ni2p$_{1/2}$ states. The Ni2p$_{3/2}$ reflects the two states of nickel ions, i.e. Ni2+ and metallic Ni positioned at 855.6 eV and 852.1 eV respectively. The other component located at binding energy 861 eV indicates the satellite peak of Ni. The two intense peaks in HR spectra of In3d located at 444.06 eV and 451.61 eV corresponds to In3d$_{5/2}$ and In3d$_{3/2}$ states, respectively, indicated In^{+3} oxidation state of In [**figure 4.7 (d)**]. Furthermore, high resolution (HR) spectra of Mn2p was deconvoluted using Gaussian function to identify the oxidation states of Mn. The single peak of Mn2p positioned at 653.4 eV, can be deconvoluted into three sub-peaks of positioned at 640.8 eV, 642.2 eV, and 644.2 eV, which indicates the existence of Mn with chemical states Mn^{2+}, Mn^{3+} and Mn^{4+} respectively as observed in **fig 4.7(e)** [**53**].

These multiple oxidation states of Mn at the interface can be beneficial for many functional properties such as dielectric behavior, magnetodielectric behavior, piezoelectric coefficient etc. due to enhancement in polarization. This alteration of Mn ions could be the reason for variation in dielectric constant due to charge ordering at the interface of the fabricated multilayer structure. Previous results also suggest that magnetodielectric coupling can be influenced by a non-centrosymmetric interfacial charge ordering in layered structure [**54, 55**].

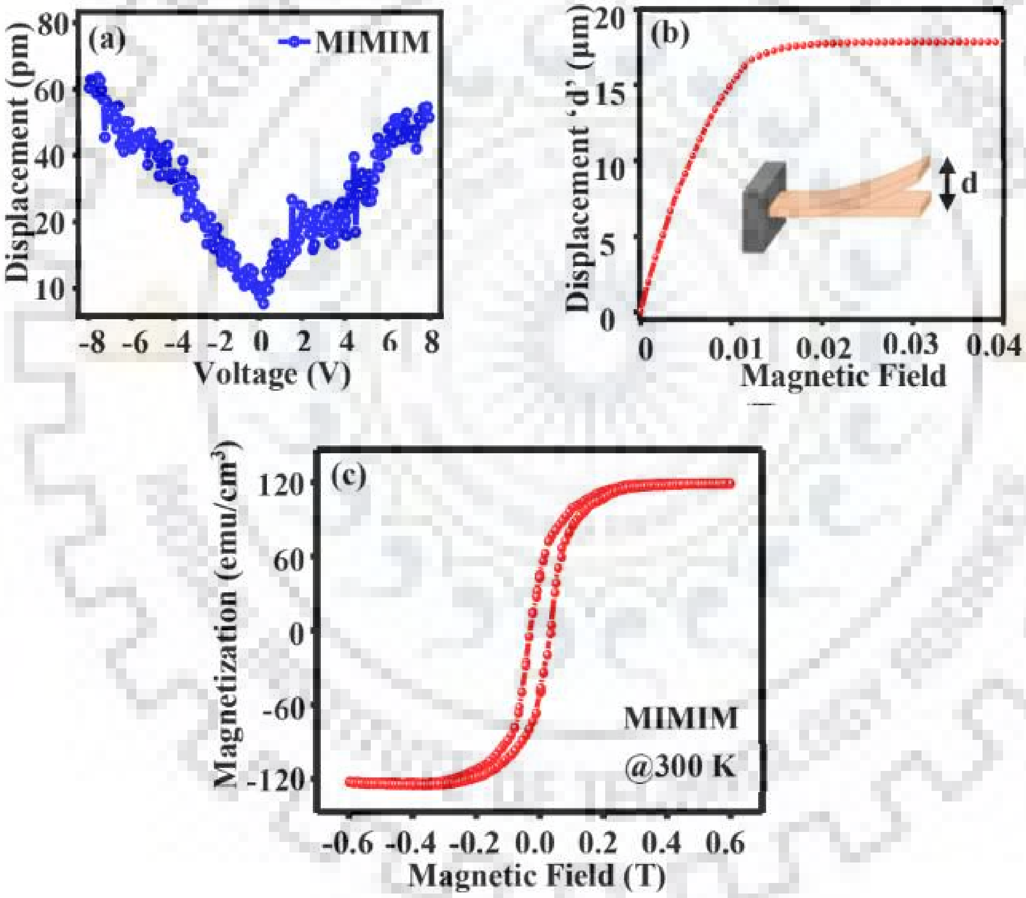

Figure 4.8. (a) Piezoelectric measurement of MIMIM structure using DBLI method. (b)A plot of the tip displacement (μm) versus magnetic field for 50 nm $Ni_{50}Mn_{35}In_{15}$ deposited on Si cantilever. Inset shows schematic of cantilever deflection with an applied magnetic field (c) Magnetic hysteresis loops of MIMIM heterostructure at room temperature.

The fabricated multilayered structure is suitable for actuator-based applications due to the incorporation of stacked piezoelectric AlN layers. **Figure 4.8 (a)** shows the piezoelectric response of the fabricated heterostructure at 1 kHz under increasing voltage levels [**56**]. The piezoelectric coefficient of MIMIM was measured at about 7.49 pm/V. This increment of piezoelectric response in MIMIM can be linked to increased polarized states of Mn ion at the interfaces. Previous studies also relate the piezoelectric coefficient with the reduction in dead layers at electrode interfaces [**57**]. This amended piezoelectric coefficient (d_{33}) of heterostructure can be very crucial in the overall transfer of strain in the fabricated heterostructure.

Most of the transducer applications require maximum movements as output [**58**]. Therefore, a large value of magnetostriction plays a vital role in the overall response of ferromagnetic alloys based layered magnetic field sensors. The magnetostrictive coefficient of NiMnIn was evaluated with the help of the micro-cantilever deflection method [**59**]. For this, a thin layer (50 nm) of NiMnIn layer was deposited on SiO_2/Si cantilever, and the deflection of cantilever tip was monitored on the application of magnetic field (inset of **figure 4.8 (b)**). A maximum deflection of ~17.7 µm was observed, as shown in **figure 4.8 (b)**. The magnetostrictive coefficient (λ) for the ferromagnetic film was found to be about ~ 1268 ppm. Such a high value of magnetostriction can be the decisive parameter for the transfer of strain in laminate ME structure. A room temperature in-plane isothermal magnetization (M-H) measurements were carried out with a DC magnetic field up to 1 T to confirm the ferromagnetic nature, as depicted in **figure 4.8 (c)**. The maximum saturation magnetization of 120 emu/cm^3 was observed at room temperature with a well saturated M-H hysteresis loop.

The schematic of the fabricated MIMIM heterostructure structure and magneto-dielectric measurements setup is shown in **figure 4.9 (a)**. The magneto-dielectric effect imitates the dielectric tunability of the MIMIM structure with the variation in the magnetic field. **Figure 4.9 (b)** shows a maximum change of 8.5% in dielectric constant for the fabricated MIMIM heterostructure at room temperature.

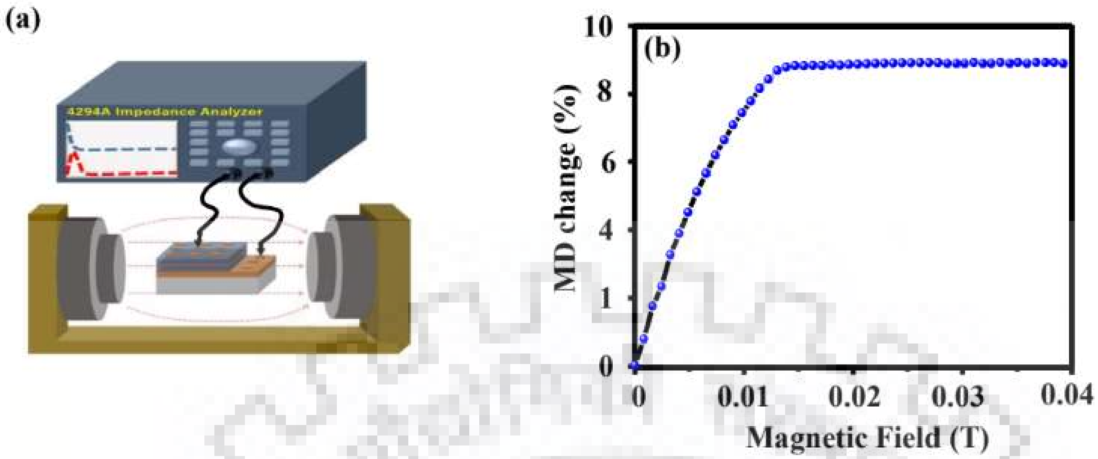

Figure 4.9. (a) Schematic diagram with a methodology adapted to perform magneto-dielectric measurements of MIMIM structure. (b) Magnetodielectric response of MIMIM heterostructure as a function of the external magnetic field at room temperature.

When a magnetic field is applied, there is a variation in young's modulus of the magnetostrictive layer. This alteration in Young's modulus produces a strain in the magnetic sensing NiMnIn layer, and this strain is transferred to the piezoelectric AlN layers. This transferred strain may also lead to the change in the dielectric permittivity of the structure [**60, 61**]. This improved magneto-dielectric response could be attributed to (i) the large magnetostriction in NiMnIn layer (ii) improved piezoelectric coefficient of the complete heterostructure and (iii) stacked multilayered heterostructure reducing the clamping effect from the substrate. Such novel structure opens a window for highly efficient magnetic field sensing applications.

4.2.4. Conclusion

The NiMnIn and AlN based magnetoelectric heterostructure having NiMnIn/AlN/NiMnIn/AlN/FSMA (MIMIM) stack configuration were fabricated. It exhibits a dielectric constant of 22.3 at 1MHz frequency is much higher compared to single-layer AlN structure. This increment in dielectric constant could be ascribed to the redistribution of interface charges which enhances the polarization. The fabricated structure exhibits a piezoelectric coefficient of 7.49 pm/V with a magnetostrictive coefficient of 1268 ppm for NiMnIn layer. The maximum magnetodielectric behavior of 8.5% was observed for multilayered structure due to large magnetoelectric coupling in the fabricated device. This work illustrates that magnetic field controlled dielectric constant in AlN based multilayered structure is useful for magnetic field sensing applications.

4.3. References

[1]. Fiebig, M., Lottermoser, T., Meier, D. and Trassin, M., 2016. The evolution of multiferroics. Nature Reviews Materials, 1(8), p.16046.

[2]. Khomskii, D., 2009. Trend: Classifying multiferroics: Mechanisms and effects. Physics, 2, p.20.

[3]. Nan, C.W., Bichurin, M.I., Dong, S., Viehland, D. and Srinivasan, G., 2008. Multiferroic magnetoelectric composites: Historical perspective, status, and future directions. Journal of applied physics, 103(3), p.1.

[4]. Martin, L.W., Crane, S.P., Chu, Y.H., Holcomb, M.B., Gajek, M., Huijben, M., Yang, C.H., Balke, N. and Ramesh, R., 2008. Multiferroics and magnetoelectrics: thin films and nanostructures. Journal of Physics: Condensed Matter, 20(43), p.434220.

[5]. Kimura, T., Tomioka, Y., Asamitsu, A. and Tokura, Y., 1998. Anisotropic magnetoelastic phenomena in layered manganite crystals: Implication of change in orbital state. Physical review letters, 81(26), p.5920.

[6]. Faran, E. and Shilo, D., 2015. Ferromagnetic shape memory alloys—challenges, applications, and experimental characterization. Experimental Techniques.

[7]. Ullakko, K., Huang, J.K., Kantner, C., O'handley, R.C. and Kokorin, V.V., 1996. Large magnetic-field-induced strains in Ni_2MnGa single crystals. Applied Physics Letters, 69(13), pp.1966-1968.

[8]. Singh, K. and Kaur, D., 2015. Direct and converse magneto-electric coupling in ferromagnetic shape memory alloys based thin film multiferroic heterostructures. Applied Physics Letters, 107(26), p.262901.

[9]. Singh, K. and Kaur, D., 2017. Room-temperature giant magneto-mechanical-electric cross-coupling in Si-integrated $PbZr_{0.52}Ti_{0.48}O_3/Ni_{50}Mn_{35}In_{15}$ multiferroic heterostructures. Journal of Physics D: Applied Physics, 50(14), p.145002.

[10]. Onuta, T.D., Wang, Y. and Long, C.J., Takeuchi 2011 Appl. Phys. Lett, 99, p.203506.

[11]. Jedrecy, N., Von Bardeleben, H.J., Badjeck, V., Demaille, D., Stanescu, D., Magnan, H. and Barbier, A., 2013. Strong magnetoelectric coupling in multiferroic $Co/BaTiO_3$ thin films. Physical Review B, 88(12), p.121409.

[12]. Li, S., Xue, Q., Duh, J.G., Du, H., Xu, J., Wan, Y., Li, Q. and Lü, Y., 2014. Driving ferromagnetic resonance frequency of FeCoB/PZN-PT multiferroic heterostructures to Ku-band via two-step climbing: composition gradient sputtering and magnetoelectric coupling. Scientific reports, 4(1), pp.1-7.

[13]. Zhang, Y., Liu, M., Zhang, L., Zhou, Z., Peng, B., Wang, C., Lin, Q., Jiang, Z.D., Ren, W. and Ye, Z.G., 2017. Multiferroic heterostructures of Fe_3O_4/PMN-PT prepared by atomic layer deposition for enhanced interfacial magnetoelectric couplings. Applied Physics Letters, 110(8), p.082902.

[14]. Zuo, Z., Zhan, Q., Dai, G., Chen, B., Zhang, X., Yang, H., Liu, Y. and Li, R.W., 2013. In-plane anisotropic converse magnetoelectric coupling effect in FeGa/polyvinylidene fluoride heterostructure films. Journal of Applied Physics, 113(17), p.17C705.

[15]. Yarar, E., Salzer, S., Hrkac, V., Piorra, A., Höft, M., Knöchel, R., Kienle, L. and Quandt, E., 2016. Inverse bilayer magnetoelectric thin film sensor. Applied Physics Letters, 109(2), p.022901.

[16]. Greve, H., Woltermann, E., Quenzer, H.J., Wagner, B. and Quandt, E., 2010. Giant magnetoelectric coefficients in $(Fe_{90}Co_{10})_{78}Si_{12}B_{10}$-AlN thin film composites. Applied Physics Letters, 96(18), p.182501.

[17]. Shi, J., Yin, L., Lu, C. and Zhu, J., 2017. Spatial angles sensitivity of Fe83Ga17/AlN/Mo/Si magnetoelectric device. AIP Advances, 7(5), p.055207.

[18]. Zheng, L., Ramalingam, S., Shi, T. and Peterson, R.L., 1993. Aluminum nitride thin film sensor for force, acceleration, and acoustic emission sensing. Journal of Vacuum Science & Technology A: Vacuum, Surfaces, and Films, 11(5), pp.2437-2446.

[19]. Mayrhofer, P.M., Riedl, H., Euchner, H., Stöger-Pollach, M., Mayrhofer, P.H., Bittner, A. and Schmid, U., 2015. Microstructure and piezoelectric response of YxAl1− xN thin films. Acta Materialia, 100, pp.81-89.

[20]. Fei, C., Liu, X., Zhu, B., Li, D., Yang, X., Yang, Y. and Zhou, Q., 2018. AlN piezoelectric thin films for energy harvesting and acoustic devices. Nano Energy, 51, pp.146-161.

[21]. Kumar, A., Pawar, S., Sharma, S. and Kaur, D., 2018. Bipolar resistive switching behavior in MoS_2 nanosheets fabricated on ferromagnetic shape memory alloy. Applied Physics Letters, 112(26), p.262106.

[22]. Rosenberger, L., Baird, R., McCullen, E., Auner, G. and Shreve, G., 2008. XPS analysis of aluminum nitride films deposited by plasma source molecular beam epitaxy. Surface and Interface Analysis: An International Journal devoted to the development and application of techniques for the analysis of surfaces, interfaces and thin films, 40(9), pp.1254-1261.

[23]. Duez, N., Mutel, B., Dessaux, O., Goudmand, P. and Grimblot, J., 2000. AlN formation by direct nitrogen implantation using a DECR plasma. Surface and Coatings Technology, 125(1-3), pp.79-83.

[24]. Alevli, M., Ozgit, C., Donmez, I. and Biyikli, N., 2012. Structural properties of AlN films deposited by plasma-enhanced atomic layer deposition at different growth temperatures. physica status solidi (a), 209(2), pp.266-271.

[25]. Yu, S., Hing, P. and Hu, X., 2002. Thermal conductivity of polystyrene–aluminum nitride composite. Composites Part A: applied science and manufacturing, 33(2), pp.289-292.

[26]. Babcock, J.A., Balster, S.G., Pinto, A., Dirnecker, C., Steinmann, P., Jumpertz, R. and El-Kareh, B., 2001. Analog characteristics of metal-insulator-metal capacitors using PECVD nitride dielectrics. IEEE Electron Device Letters, 22(5), pp.230-232.

[27]. Khovaylo, V.V., Kanomata, T., Tanaka, T., Nakashima, M., Amako, Y., Kainuma, R., Umetsu, R.Y., Morito, H. and Miki, H., 2009. Magnetic properties of Ni 50 Mn 34.8 In 15.2 probed by Mössbauer spectroscopy. Physical Review B, 80(14), p.144409.

[28]. Catalan, G., 2006. Magnetocapacitance without magnetoelectric coupling. Applied Physics Letters, 88(10), p.102902.

[29]. Vopson, M.M., Fetisov, Y.K., Caruntu, G. and Srinivasan, G., 2017. Measurement techniques of the magneto-electric coupling in multiferroics. materials, 10(8), p.963.

[30]. Bichurin, M.I., Petrov, V.M., Leontiev, V.S., Ivanov, S.N. and Sokolov, O.V., 2017. Magnetoelectric effect in layered structures of amorphous ferromagnetic alloy and gallium arsenide. Journal of Magnetism and Magnetic Materials, 424, pp.115-117.

[31]. Ciomaga, C.E., Avadanei, O.G., Dumitru, I., Airimioaei, M., Tascu, S., Tufescu, F. and Mitoseriu, L., 2016. Engineering magnetoelectric composites towards application as tunable microwave filters. Journal of Physics D: Applied Physics, 49(12), p.125002.

[32]. Wang, Y. and Weng, G.J., 2015. Magnetoelectric coupling and overall properties of multiferroic composites with 0-0 and 1-1 connectivity. Journal of Applied Physics, 118(17), p.174102.

[33]. Jeon, N., Rout, D., Kim, I.W. and Kang, S.J.L., 2011. Enhanced multiferroic properties of single-phase $BiFeO_3$ bulk ceramics by Ho doping. Applied Physics Letters, 98(7), p.072901.

[34]. Mundy, J.A., Brooks, C.M., Holtz, M.E., Moyer, J.A., Das, H., Rébola, A.F., Heron, J.T., Clarkson, J.D., Disseler, S.M., Liu, Z. and Farhan, A., 2016. Atomically engineered ferroic layers yield a room-temperature magnetoelectric multiferroic. Nature, 537(7621), pp.523-527.

[35]. Zurbuchen, M.A., Wu, T., Saha, S., Mitchell, J. and Streiffer, S.K., 2005. Multiferroic composite ferroelectric-ferromagnetic films. Applied Physics Letters, 87(23), p.232908.

[36]. Fiebig, M., 2005. Revival of the magnetoelectric effect. Journal of physics D: applied physics, 38(8), p.R123.

[37]. Lee, M.K., Nath, T.K., Eom, C.B., Smoak, M.C. and Tsui, F., 2000. Strain modification of epitaxial perovskite oxide thin films using structural transitions of ferroelectric $BaTiO_3$ substrate. Applied Physics Letters, 77(22), pp.3547-3549.

[38]. Yin, L.H., Zou, Y.M., Yang, J., Dai, J.M., Song, W.H., Zhu, X.B. and Sun, Y.P., 2016. Colossal magnetodielectric effect and spin flop in magnetoelectric $Co_4Nb_2O_9$ crystal. Applied Physics Letters, 109(3), p.032905.

[39]. Wang, Y., Hasanyan, D., Li, J., Viehland, D. and Luo, H., 2012. Shear-mode magnetostrictive/piezoelectric composite with an enhanced magnetoelectric coefficient. Applied Physics Letters, 100(20), p.202903.

[40]. Kang, M.G., Kang, H.B., Clavel, M., Maurya, D., Gollapudi, S., Hudait, M., Sanghadasa, M. and Priya, S., 2018. Magnetic field sensing by exploiting giant nonstrain-mediated magnetodielectric response in epitaxial composites. Nano letters, 18(5), pp.2835-2843.

[41]. Koo, Y.S., Bonaedy, T., Sung, K.D., Jung, J.H., Yoon, J.B., Jo, Y.H., Jung, M.H., Lee, H.J., Koo, T.Y. and Jeong, Y.H., 2007. Magnetodielectric coupling in core/shell $BaTiO_3$/ γ-Fe_2O_3 nanoparticles. Applied Physics Letters, 91(21), p.212903.

[42]. Tiwari, S. and Vitta, S., 2018. Magnetoelectric and magnetodielectric coupling and microwave resonator characteristics of $Ba_{0.5}Sr_{0.5}Nb_2O_6/CoCr_{0.4}Fe_{1.6}O_4$ multiferroic composite. Scientific reports, 8(1), pp.1-12.

[43]. Bai, Y., Jiang, N. and Zhao, S., 2018. Giant magnetoelectric effects in pseudo 1–3 heterostructure films with FeGa nanocluster-assembled micron-scale discs embedded into $Bi_5Ti_3FeO_{15}$ matrices. Nanoscale, 10(21), pp.9816-9821.

[44]. Singh, K. and Kaur, D., 2015. Manifestation of martensitic phase transformation and magneto-caloric properties in high quality magnetron sputtered Ni–Mn–In//Si ultra-thin films. Sensors and Actuators A: Physical, 236, pp.247-256.

[45]. Akiyama, M., Ueno, N., Nonaka, K. and Tateyama, H., 2003. Flexible pulse-wave sensors from oriented aluminum nitride nanocolumns. Applied physics letters, 82(12), pp.1977-1979.

[46]. Pawar, S., Kumar, A., Singh, K. and Kaur, D., 2018. High magnetoelectric coupling in Si-integrated AlN/NiMnIn thin film double layers at room temperature. Applied Physics Letters, 113(24), p.242902.

[47]. Pawar, S., Singh, K., Sharma, S., Pandey, A., Dutta, S. and Kaur, D., 2018. Growth assessment and scrutinize dielectric reliability of c-axis oriented insulating AlN thin films in MIM structures for microelectronics applications. Materials Chemistry and Physics, 219, pp.74-81.

[48]. Pradhan, D.K., Kumari, S., Vasudevan, R.K., Strelcov, E., Puli, V.S., Pradhan, D.K., Kumar, A., Gregg, J.M., Pradhan, A.K., Kalinin, S.V. and Katiyar, R.S., 2018. Exploring the magnetoelectric coupling at the composite interfaces of FE/FM/FE heterostructures. Scientific reports, 8(1), pp.1-11.

[49]. Fumagalli, L., Ferrari, G., Sampietro, M. and Gomila, G., 2007. Dielectric-constant measurement of thin insulating films at low frequency by nanoscale capacitance microscopy. Applied Physics Letters, 91(24), p.243110.

[50]. Balma, D., Mazzalai, A., Chidambaram, N., Sandu, C.S., Neels, A., Dommann, A., Hess, P., Binz, D. and Muralt, P., 2014. High piezoelectric longitudinal coefficients in sol–gel PZT thin film multilayers. Journal of the American Ceramic Society, 97(7), pp.2069-2075.

[51]. Maity, N., Mandal, A. and Nandi, A.K., 2017. High dielectric poly (vinylidene fluoride) nanocomposite films with MoS_2 using polyaniline interlinker via interfacial interaction. Journal of Materials Chemistry C, 5(46), pp.12121-12133.

[52]. Mikhelashvili, V., Thangadurai, P., Kaplan, W.D. and Eisenstein, G., 2008. High capacitance density metal-insulator-metal structures based on a high-κ Hf N_xO_y–SiO_2–Hf TiO_y laminate stack. Applied Physics Letters, 92(13), p.132902.

[53]. Chen, Z., Yang, Q., Li, H., Li, X., Wang, L. and Tsang, S.C., 2010. Cr–MnO_x mixed-oxide catalysts for selective catalytic reduction of NOx with NH_3 at low temperature. Journal of Catalysis, 276(1), pp.56-65.

[54]. Ikeda, N., Ohsumi, H., Ohwada, K., Ishii, K., Inami, T., Kakurai, K., Murakami, Y., Yoshii, K., Mori, S., Horibe, Y. and Kitô, H., 2005. Ferroelectricity from iron valence ordering in the charge-frustrated system $LuFe_2O_4$. Nature, 436(7054), pp.1136-1138.

[55]. Vaz, C.A.F. and Staub, U., 2013. Artificial multiferroic heterostructures. Journal of Materials Chemistry C, 1(41), pp.6731-6742.

[56]. Sivaramakrishnan, S., Mardilovich, P., Mason, A., Roelofs, A., Schmitz-Kempen, T. and Tiedke, S., 2013. Electrode size dependence of piezoelectric response of lead zirconate titanate thin films measured by double beam laser interferometry. Applied Physics Letters, 103(13), p.132904.

[57]. Pérez de la Cruz, J., Joanni, E., Vilarinho, P.M. and Kholkin, A.L., 2010. Thickness effect on the dielectric, ferroelectric, and piezoelectric properties of ferroelectric lead zirconate titanate thin films. Journal of Applied Physics, 108(11), p.114106.

[58]. Ekreem, N.B., Olabi, A.G., Prescott, T., Rafferty, A. and Hashmi, M.S.J., 2007. An overview of magnetostriction, its use and methods to measure these properties. Journal of Materials Processing Technology, 191(1-3), pp.96-101.

[59]. Singh, J., Kumar, A. and Chelvane, J.A., 2019. Stress compensated MEMS magnetic actuator based on magnetostrictive $Fe_{65}Co_{35}$ thin films. Sensors and Actuators A: Physical, 294, pp.54-60.

[60]. Pawar, S., Singh, J. and Kaur, D., 2019. Magnetic field tunable Ferromagnetic Shape Memory Alloy based Piezo-Resonator. IEEE Electron Device Letters.

[61]. Arritt, B., Adomanis, B., Khraishi, T. and Smith, D., 2010. Parametric analysis of the strain-dependent behavior of a metamaterial electric resonator. Applied Physics Letters, 97(19), p.191907.

Chapter 5

Magnetic field tunable piezo-resonator

CHAPTER 5

MAGNETIC FIELD TUNABLE FERROMAGNETIC SHAPE MEMORY ALLOY BASED PIEZO-RESONATOR


भारतीय प्रौद्योगिकी संस्थान रुड़की
INDIAN INSTITUTE OF TECHNOLOGY ROORKEE

5.1. Introduction

In the current era, Bulk Acoustic Wave (BAW) devices have practically substituted Surface Acoustic Wave (SAW) devices due to a wide range of applications of BAW in the wireless domain for modern electronics. BAW resonators also play a crucial role in RF components in various kinds of sensors and communication devices operating at a higher frequency. With recent developments and advancement in technology, there is a need to tune the resonant frequency with some external parameters like the electric field, temperature, magnetic field etc **[1, 2]**. This increase the importance of the BAW device without altering the complicated fabrication process. The frequency tuning is highly crucial for filters, phase shifter, and resonators as it prevents any deviation in their standard resonant frequency due to ageing, environmental factors, thermal mismatch etc. **[3]**. Magnetoelectric composites-based BAW resonators have achieved substantial research owing to its ability to control the reflection spectrum by an external magnetic field **[4, 5]**.

Magnetoelectric is the class of materials in which magnetic and electric responses are interlinked [6]. In layered structures, the strain transfer mechanism is responsible for the coupling between ferromagnetic and piezoelectric films. They are a strong candidate for the design and development of innovative electronic devices **[7-9]**. The strength of magnetodielectric coupling in these structures depends on factors such as interface quality, morphology, and functional properties of individual layers **[10]**. Therefore, these layered structures require attention for their use in futuristic magnetic field tunable microwave devices like filters, resonators, phase shifters.

Ferromagnetic Shape memory alloys (FSMAs) are the class of materials used in magnetic actuation applications because of their giant magnetostrictive response **[11]**. But little work is reported on the combination of FSMAs alloy with piezoelectric materials **[12, 13]**. Our previous results show excellent ME coupling between NiMnIn alloy and AlN piezoelectric layers **[6]**. Furthermore, BAW devices based on AlN are in more demand due to its high acoustic velocity, high stiffness and CMOS compatibility **[14, 15]**.

In this work, we have studied the effect of magnetic field on the resonant frequency of AlN/NiMnIn layered based BAW resonator. The resonant frequency, acoustic velocity, coupling coefficient and circuit components were related to the change in young modulus of the ferromagnetic layer. Such tunable devices can be vital in the applications of magnetic field sensing at room temperature.

5.2. Experimental Details

The NiMnIn/AlN thin film-based BAW device was fabricated on a (100) p-type silicon substrate using DC magnetron sputtering. Initially, a ferromagnetic $Ni_{50}Mn_{35}In_{15}$ layer of thickness ~750 nm was sputtered on a silicon substrate at 500℃ for 6 min with deposition pressure of 10 mTorr. For the excitation of the longitudinal/ transversal BAW resonator, a c-axis wurtzite structured layer of AlN (~800 nm) were grown on NiMnIn at an elevated temperature of 400℃. The sputtering pressure of 4 mTorr was maintained in a mixed nitrogen and argon atmosphere with flow rates of 6 sccm and 14 sccm respectively. The top electrode (NiMnIn) of the BAW resonator was deposited through a stencil mask with circular patterns of radius 300 μm. The films were grown ex-situ, and no annealing process was employed.

The phase formation and crystallographic structure of the layered structure were explored by X-ray diffractometer (Bruker advanced D8) using Cu Kα (1.54 Å) source. The Field Emission Scanning Electron Microscopy (FESEM) imaging was performed for cross-sectional and interface study of the layered BAW device. The complete frequency spectra of the layered BAW resonator were measured with the preferential excitation of a magnetic field. The strength of the magnetic field is changed by adjusting the distance between the permanent magnets. The device was fixed between the poles of permanent rare-earth-based magnets with field parallel to the plane of the resonator. The electrical RF measurement of the BAW device was performed with a coplanar probe station coupled with the Vector Network Analyser (VNA). The reflectivity $|S_{11}|$ with and without magnetic field was inspected using a calibrated probe station connected to network analyzer in the range of 0-18 GHz.

5.3. Results and discussion.

To investigate the crystalline structure of AlN/NiMnIn coated Si substrate, at a grazing angle of 2˚with a slow scan rate of 2˚/min, as shown in **figure 5.1 (a)**. The observed dominant (002) peak centred at $2\theta \sim 36.22^\circ$ can be assigned to c-axis wurtzite AlN. On the other hand, a small (220) peak positioned at $2\theta \sim 42.22^\circ$ corresponds to the cubic structure of the NiMnIn alloy **[16]**. Absence of any undesired peaks reflects a highly crystalline and good quality of fabricated thin films. The low surface roughness (~3.24 nm) of underlaying NiMnIn film may have inspired c-axis oriented AlN columnar structure normal to the underneath surface (**inset of figure 5.1 (a)**). Further, **figure 5.1 (b)** shows the fractured cross-sectional FESEM image of the layered AlN/NiMnIn heterostructure. The morphology shows bi-layer formation with columnar AlN grains, Island by island (Stranski-Krastanov) growth of AlN film, and a thickness of ~800 nm and ~ 750 nm for AlN and NiMnIn layer respectively. Inset of **figure 5.1(b)** shows the SEM image of uniform grain morphology of AlN layer.

The piezoelectric coefficient of the AlN/NiMnIn is measured by the Double Beam Laser Interferometry (DBLI) method **[17]**. As shown in **figure 5.1(c)**, the longitudinal piezoelectric coefficient (d_{33}) is found to be around 4.23 pm/V. DBLI is a technique used to characterize the piezoelectric response of piezoelectric materials with high precision (in order of Å). The magnetostriction coefficient of the NiMnIn layer is measured using the static cantilever deflection method **[18]**. In the cantilever deflection method, a layer of FSMA was deposited on a cantilever beam (580 µm X 200 µm).

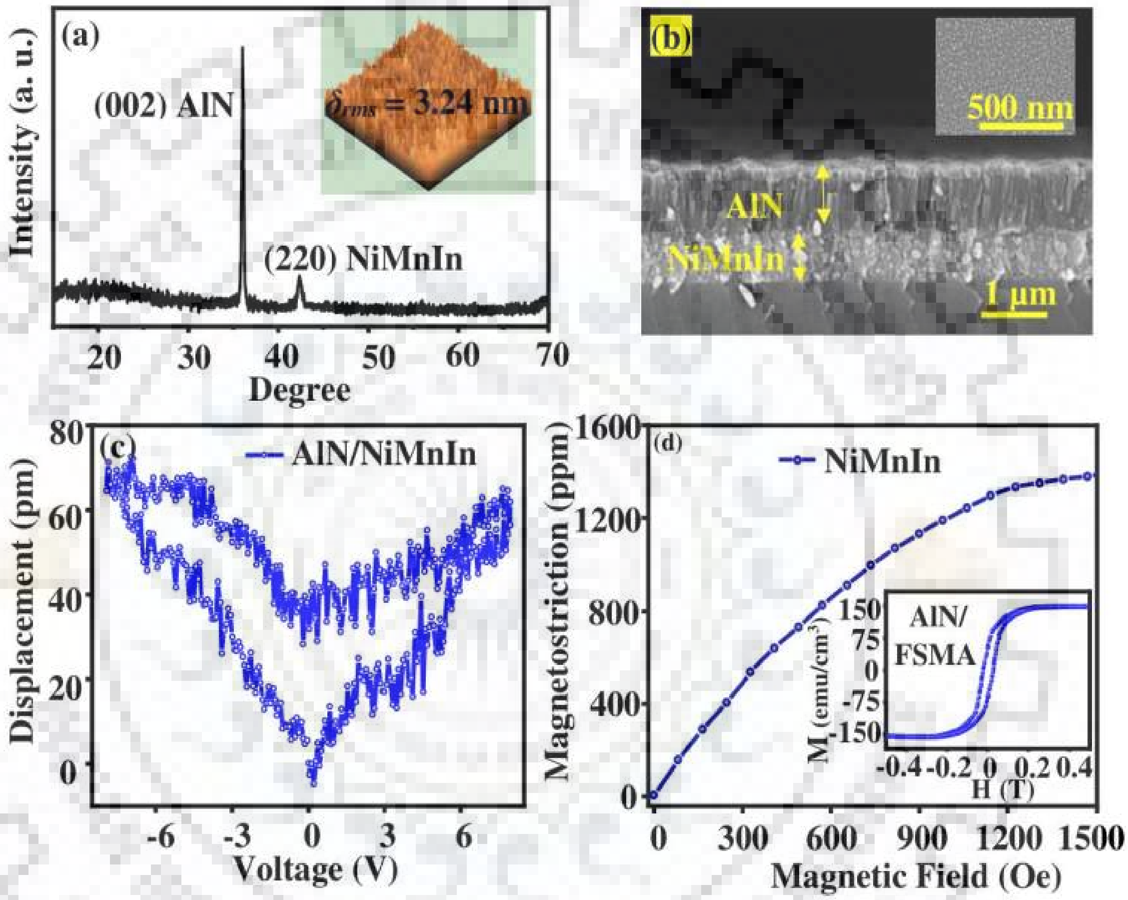

Figure 5.1 (a) XRD pattern of AlN/FSMA structure. The inset shows the AFM image of NiMnIn layer. (b) Cross-sectional FESEM image of Layered Structure. The inset depicts the SEM image of the AlN layer. (c) Piezoelectric Coefficient using DBLI method and (d) Magnetostriction measurement of NiMnIn layer using Cantilever method. The inset shows the M-H measurement of AlN/FSMA structure.

Laser interferometry was used to measure the cantilever deflection (displacement) due to magnetostriction of the ferromagnetic layer in the presence of the DC magnetic field. The magnetostriction coefficient was found to be about 1260 ppm for 1200 Oe magnetic field **(figure 5.1(d)) [19]**. The NiMnIn thin film is the austenite phase, (**figure 5.1(a)**). Therefore, the significant contribution of strain is via domain wall motions. Inset of **figure 5.1 (d)** reflects the magnetization hysteresis loop of AlN/NiMnIn bilayer structure at room temperature. Initially, RF measurements of the fabricated BAW resonator with AlN piezoelectric layer were performed with VNA by wire bonding BAW device onto a testing board. Inset of **figure 5.2 (a)** shows the prototype of the one port BAW device. The reflection parameter (S_{11}) frequency spectra of fabricated AlN/NiMnIn layered resonator with preferential excitation shear mode in the range 0– 18 GHz is shown in **figure 5.2 (a)**. The excitation was given using a coaxial connector with the centre pin connected to the top NiMnIn layer and grounding the bottom electrode.

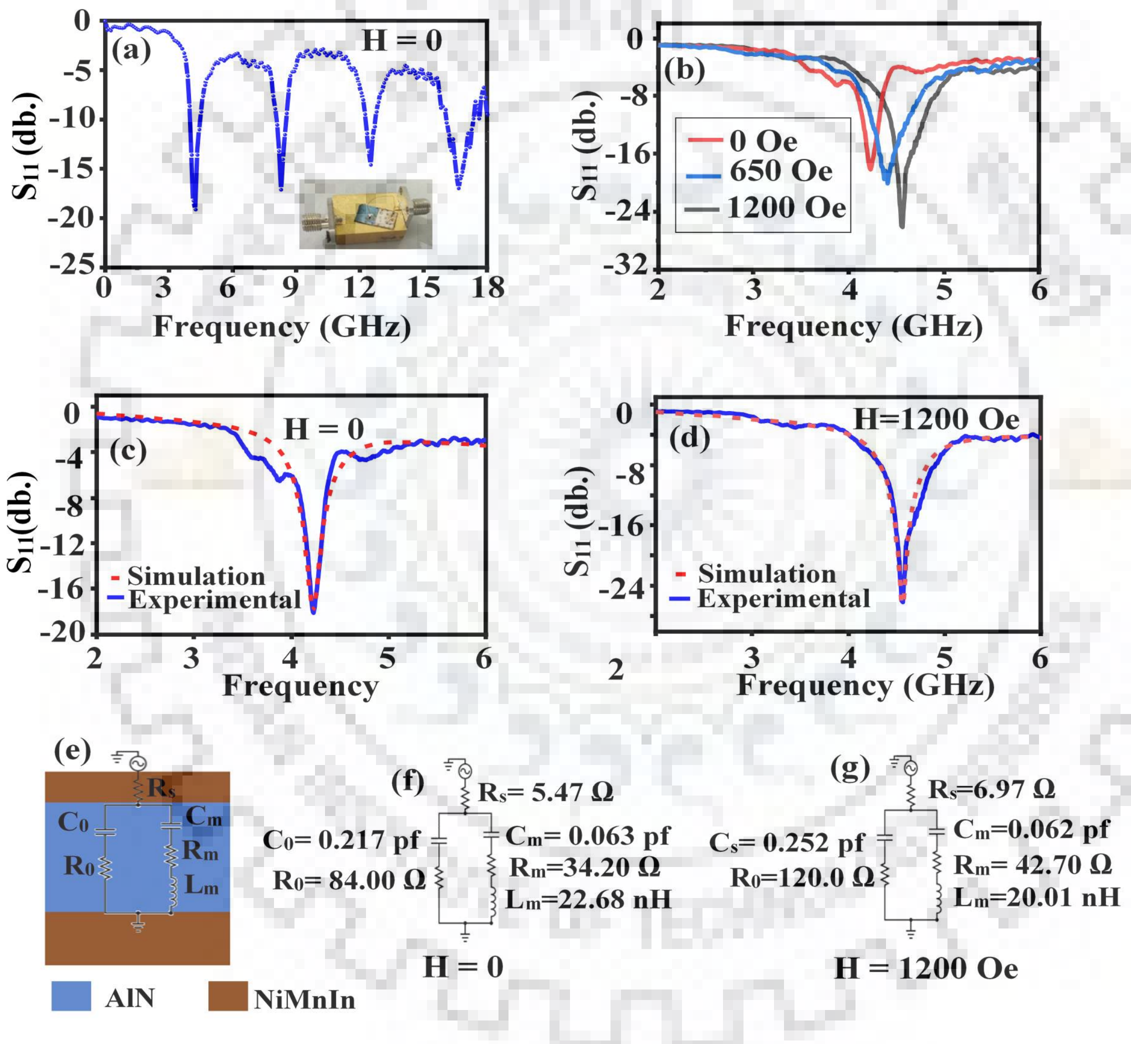

Figure 5.2 (a) The S_{11} spectrum of AlN/NiMnIn structure without a magnetic field. The inset shows the fabricated structure with the setup used for measurement. (b) Resonant frequency at a different magnetic field. (c), (d), (e), (f) & (g) Simulated m-BVD model with H_{dc}=0 and H_{dc}=1200Oe respectively using ADS software.

The fundamental resonant frequency of the device was found to be around 4.22 GHz.

The acoustic velocity (v) of the resonator was found to be ~6750 m/s using the formula, $f=v/2d$, where f, v, and d are the equivalent fundamental frequency, acoustic velocity, and thickness of the resonator respectively. The obtained value of acoustic velocity is comparable to the previous results reported in the literature **[20]**. The S_{11} measurement was repeated several times over a long duration, but the resonance frequency was steady. It shows the suitability of the fabricated device for sensing application.

The effect of magnetic field on the resonant frequency of BAW resonator is studied by placing it between poles of permanent rare-earth-based magnets with the field applied parallel to the plane of the resonator. The NiMnIn layer being a ferromagnetic magnetic shape memory alloy has a significant magnetostriction coefficient (λ). Therefore, it is used as a magnetic field sensing layer in the fabricated BAW resonator. On the application of an external DC magnetic field, there is a change in Young's modulus (E_m) of the magnetostrictive layer (Delta-E effect) due to the reorganization of the magnetic domains **[21]**. The change in young modulus is directly proportional to the square of the applied magnetic field H_{dc} **[22]**. This alteration in Young's modulus (E_m) produces a strain in the NiMnIn layer. Transfer of strain from the ferromagnetic layer to the piezoelectric AlN layer underneath via strain mediated magnetoelectric coupling **[23]**. Strain transferred from the magnetostrictive layer to the piezoelectric layer alters the young's modulus (E_p) of the piezoelectric layer.

The Young's modulus of the piezoelectric layer and the resonant frequency of BAW resonator can be related to acoustic velocity (v), $v = \sqrt{(E_p / \rho_p)}$ and $f = v / 2d_p$ where d, ρ_p and E_p are thickness, density and young's modulus of AlN thin film respectively. This shift in resonant frequency can be ascribed to strain transfer between the magnetic field sensing NiMnIn layer and the piezoelectric layer due to magnetoelectric coupling. There is an increase in the resonant frequency with the increment in the strength of the magnetic field. The shift in resonance frequency (Δf) is directly proportional to Em or square of H_{dc} under the limit $\Delta E_m \ll E_m$, where E_m is the young's modulus of the magnetostrictive layer **[24]**. The shift in resonance frequency can be related to change in young modulus (ΔE_m) of the magnetostrictive layer is given by eq. (5.1)

$$\frac{\Delta f}{f_o} = \frac{1}{2}\ \frac{t_m}{t_p}\ \left[3\ \frac{\Delta E_m + E_m}{E_p} - \frac{\rho_m}{\rho_p}\right]^{1/2} \tag{5.1}$$

Where t_m, t_p, E_m, E_p, ρ_m, ρ_p are thickness, young's modulus, and density of the magnetostrictive and the piezoelectric layer respectively and f_o is the resonance frequency of the resonator in the absence of magnetic field. Assuming $E_m >> \Delta E_m \; and \; E_m \geq E_p$, the shift in resonant frequency (Δf) is given by eq. (5.2).

$$\frac{\Delta f}{f_o} = \frac{3}{4} \frac{t_m}{t_p} \frac{1}{\left(3 - {\rho_m}/{\rho_p}\right)^{1/2}} \frac{\Delta E_m}{E_m} \tag{5.2}$$

The above equations reveal that the change in the magnitude of the resonance frequency *(f)* is directly proportional to the change in the magnitude of the young modulus (ΔE_m) of the magnetostrictive layer. These results reflect the potential of such multiferroic BAW resonators for tunable microwave resonator /filter and magnetic field sensor.

Advance Design System software (Agilent) was used to extract an equivalent modified Butterworth-Van Dyke (mBVD) circuits of BAW resonator in the absence and presence of magnetic field (**figure 5.2(c-g)**). The circuits parameter such as resistance, capacitance and inductance show a variation in their value with the magnetic field. R_m, C_m and L_m are motional resistance, motional capacitance, motional inductance respectively of a resonator. C_o corresponds to the static capacitance between the electrodes of resonator and R_s is the contact resistance of the magnetostrictive layer. The resistance R_s increases due to the magnetoresistance effect of the ferromagnetic layer **[25]**.

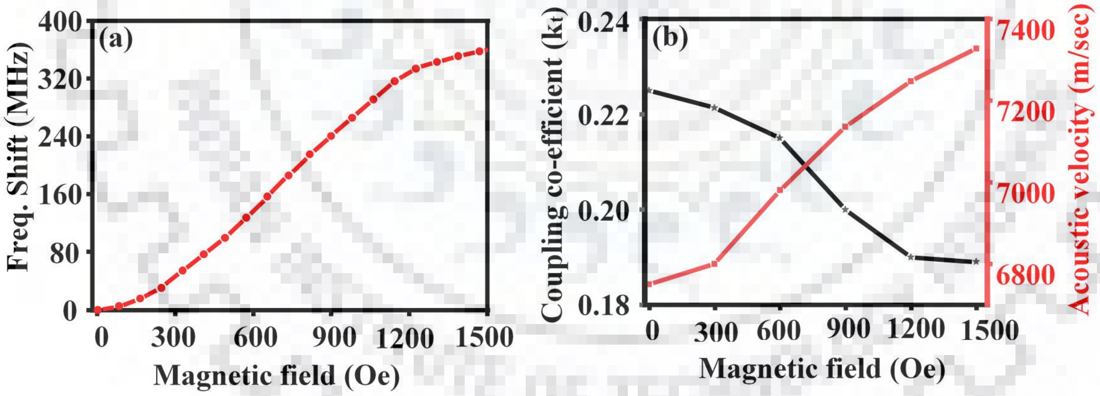

Figure 5.3 (a) Change in resonant frequency with Magnetic field. (b) Variation in coupling coefficient and acoustic velocity of the fabricated structure.

The value of C_o depends on the geometry and dielectric permittivity of the AlN film. The magnetoelectric coupling in layered structure leads to the changes in effective dielectric permittivity and thus facilitates in the variation of static capacitance **[26]**. The strain transferred from the magnetostrictive layer leads to the alteration in the unit cell geometry of the AlN layer. This strain could result in the variation of dipole alignment in the piezoelectric layer. Thus, it alters the motional capacitance/inductance of the resonator. The generation of eddy current in the magnetic field introduces variation in motional resistance.

To further investigate the magnetic field sensitivity of the BAW resonator, the variation in the resonant frequency was plotted as a function of magnetic field strength as presented in **figure 5.3 (a)**. A magnetic field of 1200 Oe produces a variation of ~350 MHz. Furthermore, an increase in an external magnetic field decreases the electromechanical coupling coefficient (k_t) of the BAW resonator. A maximum value of k_t ~ 0.22 is achieved in the absence of a magnetic field **(figure 5.3 (b))**. The acoustic velocity of the piezoelectric shows an increment with applied magnetic field strength.

5.4. Conclusion

In summary, highly magnetostrictive NiMnIn and AlN piezoelectric thin film based magnetic field sensing resonator was fabricated with magnetron sputtering. Without the magnetic field, the resonant frequency of the resonator was 4.22 GHz. A magnetic field of 1200 Oe produces a shift of ~360 MHz in the resonant frequency of the resonator. Such tunable resonators can be vital in designing futuristic tunable filters, and magnetic field sensors without using the complex fabrication processes.

5.5. References.

[1]. Fattinger, G.G., 2008, May. BAW resonator design considerations-an overview. In 2008 IEEE [1]. International Frequency Control Symposium (pp. 762-767). IEEE.

[2]. Berge, J. and Gevorgian, S., 2011. Tunable bulk acoustic wave resonators based on $Ba_{0.25}Sr_{0.75}TiO_3$ thin films and a HfO_2/SiO_2 Bragg reflector. IEEE transactions on ultrasonics, ferroelectrics, and frequency control, 58(12), pp.2768-2771.

[3]. Adams, S.G., Bertsch, F.M., Shaw, K.A., Hartwell, P.G., Moon, F.C. and MacDonald, N.C., 1998. Capacitance based tunable resonators. Journal of Micromechanics and Microengineering, 8(1), p.15.

[4]. Yao, Z., Wang, Y.E., Keller, S. and Carman, G.P., 2015. Bulk acoustic wave-mediated multiferroic antennas: Architecture and performance bound. IEEE Transactions on Antennas and Propagation, 63(8), pp.3335-3344.

[5]. Polzikova, N., Alekseev, S., Kotelyanskii, I., Raevskiy, A. and Fetisov, Y., 2013. Magnetic field tunable acoustic resonator with ferromagnetic-ferroelectric layered structure. Journal of Applied Physics, 113(17), p.17C704.

[6]. Pawar, S., Kumar, A., Singh, K. and Kaur, D., 2018. High magnetoelectric coupling in Si-integrated AlN/NiMnIn thin film double layers at room temperature. Applied Physics Letters, 113(24), p.242902.

[7]. Guo, M. and Dong, S., 2009. A resonance-bending mode magnetoelectric-coupling equivalent circuit. IEEE transactions on ultrasonics, ferroelectrics, and frequency control, 56(11), pp.2578-2586.

[8]. Kumar, A., Goswami, A., Singh, K., McGee, R., Thundat, T. and Kaur, D., 2019. Magnetoelectric Coupling in Ni–Mn–In/PLZT Artificial Multiferroic Heterostructure and Its Application in Mid-IR Photothermal Modulation by External Magnetic Field. ACS Applied Electronic Materials, 1(11), pp.2226-2235.

[9]. Singh, K. and Kaur, D., 2017. Four logic states of tunneling Magnetoelectroresistance in ferromagnetic shape memory alloy based multiferroic tunnel junctions. Applied Physics Letters, 111(2), p.022902.

[10]. Paudel, B., Vasiliev, I., Hammouri, M., Karpov, D., Chen, A., Lauter, V. and Fohtung, E., 2019. Strain vs. charge mediated magnetoelectric coupling across the magnetic oxide/ferroelectric interfaces. RSC advances, 9(23), pp.13033-13041.

[11]. Choi, B.S., 2006. Thermal, magnetic, and magnetoelastic data on three different Heusler alloys based on Ni-Mn-X (X= Ga, in, or Sn). IEEE transactions on magnetics, 42(7), pp.1770-1777.

[12]. Chen, S.Y., Ye, Q.Y., Miao, W., Wang, D.H., Wan, J.G., Liu, J.M., Du, Y.W., Huang, Z.G. and Zhou, S.Q., 2010. Direct and converse magnetoelectric effects in $Ni_{43}Mn_{41}Co_5Sn_{11}$/Pb (Zr, Ti) O_3 laminate. Journal of Applied Physics, 107(9), p.09D901.

[13]. Yang, Y.T., Gong, Y.Y., Ma, S.C., Shen, C.J., Wang, D.H., Cao, Q.Q., Zhong, Z.C. and Du, Y.W., 2015. Electric-field control of exchange bias field in a $Mn_{50.1}Ni_{39.3}Sn_{10.6}$/piezoelectric laminate. Journal of Alloys and Compounds, 619, pp.1-4.

[14]. Pawar, S., Singh, K., Sharma, S., Pandey, A., Dutta, S. and Kaur, D., 2018. Growth assessment and scrutinize dielectric reliability of c-axis oriented insulating AlN thin films in MIM structures for microelectronics applications. Materials Chemistry and Physics, 219, pp.74-81.

[15]. García-Gancedo, L., Zhu, Z., Iborra, E., Clement, M., Olivares, J., Flewitt, A.J., Milne, W.I., Ashley, G.M., Luo, J.K., Zhao, X.B. and Lu, J.R., 2011. AlN-based BAW resonators with CNT electrodes for gravimetric biosensing. Sensors and Actuators B: Chemical, 160(1), pp.1386-1393.

[16]. Kumar, A., Pawar, S., Sharma, S. and Kaur, D., 2018. Bipolar resistive switching behavior in MoS_2 nanosheets fabricated on ferromagnetic shape memory alloy. Applied Physics Letters, 112(26), p.262106.

[17]. Urbanaviciute, I., Meng, X., Biler, M., Wei, Y., Cornelissen, T.D., Bhattacharjee, S., Linares, M. and Kemerink, M., 2019. Negative piezoelectric effect in an organic supramolecular ferroelectric. Materials Horizons, 6(8), pp.1688-1698.

[18]. Hunter D, Osborn W, Wang K, Kazantseva N, Hattrick-Simpers J, Suchoski R, Takahashi R, Young ML, Mehta A, Bendersky LA, Lofland SE. Giant magnetostriction in annealed $Co_{1-x}Fe_x$ thin-films. Nature communications. 2011 Nov 1;2(1):1-7.

[19]. Singh, J., Kumar, A. and Chelvane, J.A., 2019. Stress compensated MEMS magnetic actuator based on magnetostrictive $Fe_{65}Co_{35}$ thin films. Sensors and Actuators A: Physical, 294, pp.54-60.

[20]. Tadesse, S.A. and Li, M., 2014. Sub-optical wavelength acoustic wave modulation of integrated photonic resonators at microwave frequencies. Nature communications, 5, p.5402.

[21]. Hubert, O. and Daniel, L., 2010. Measurement and Analytical Modeling of the ΔE Effect in a Bulk Iron-Cobalt Alloy. IEEE Transactions on Magnetics, 46(2), pp.401-404.

[22]. Ludwig, A. and Quandt, E., 2002. Optimization of the ΔE effect in thin films and multilayers by magnetic field annealing. IEEE transactions on magnetics, 38(5), pp.2829-2831.

[23]. Singh, K., Singh, S.K. and Kaur, D., 2014. Strain mediated coupling in magnetron sputtered multiferroic PZT/Ni-Mn-In/Si thin film heterostructure. Journal of Applied Physics, 116(11), p.114103.

[24]. Yoshizawa, N., Yamamoto, I. and Shimada, Y., 2005. Magnetic field sensing by an electrostrictive /magnetostrictive composite resonator. IEEE transactions on magnetics, 41(11), pp.4359-4361.

[25]. Cao, D., Zhang, Y., Dong, W., Yang, J., Bai, W., Chen, Y., Wang, G., Dong, X. and Tang, X., 2015. Structure, magnetic and transport properties of $La_{0.7}CaSr_xMnO_3$ thin films by sol–gel method. Ceramics International, 41, pp. S381-S386.

[26]. Ding, Y., Yao, Y.D., Wu, K.T., Chen, P.S., Tu, C.S., Hsu, J.C., Hung, D.S. and Lee, S.F., 2012. Thickness Effect of Interlayer on the Dielectric Permittivity of $BaTiO_3$/Co/$BaTiO_3$ and $BaTiO_3$/Ta/$BaTiO_3$ Films. IEEE transactions on magnetics, 48(11), pp.4297-4300.

Chapter 6

Conclusion and Future Prospects

भारतीय प्रौद्योगिकी संस्थान रुड़की
INDIAN INSTITUTE OF TECHNOLOGY ROORKEE

CHAPTER 6

CONCLUSION AND FUTURE PROSPECTS

6.1. Growth assessment and scrutinize dielectric reliability of AlN thin films

6.2. Room temperature ME coupling AlN/NiMnIn thin film structure.

6.3. Influence of encapsulating a magnetostrictive thin film on magneto-dielectric (MD) response.

6.4. Magnetic field tunable Ferromagnetic Shape Memory Alloy based Piezo-Resonator


भारतीय प्रौद्योगिकी संस्थान रुड़की
INDIAN INSTITUTE OF TECHNOLOGY ROORKEE

The main aim of the present thesis is to fabricate the AlN/FSMA thin film structures using DC magnetron sputtering for MEMs acoustic resonators while preserving the ferromagnetic shape memory effect and piezoelectric properties of FSMA and AlN respectively. The structural, piezoelectric, electrical and magnetic properties of AlN and FSMA were systematically investigated. We have integrated CMOS compatible aluminium nitride (AlN) with highly magnetostrictive ferromagnetic shape memory alloy (FSMA) to develop a magnetoelectric layered composite with high magnetoelectric strength, high ME coefficients, high reproducibility, broad availability and operational at room temperature. Lastly, a magnetic field tunable Piezo-Resonator was realized using FSMA/AlN magnetoelectric structure was designed and characterized for its application in MEMS acoustic devices. A summary and conclusion of the entire work are as follows.

6.1. Growth assessment and scrutinize dielectric reliability of AlN thin films for microelectronics applications.

In this work, the effect of bottom electrodes (Al, Pt & Ti) on the texture, piezoelectric characteristics, dielectric properties and leakage current behavior of reactive DC magnetron sputtered AlN thin films was systematically studied **[Table 6.1]**.

Table 6.1 Properties of AlN thin film with different bottom electrodes

Parameters	Electrode		
	Al	**Ti**	**Pt**
FWHM	5.45º	4.70º	7.70º
Roughness (nm)	13.5	10.5	12.5
Grain Size (nm)	47	55	44
Piezoelectric Coefficient (d_{33}) (pm/V)	4.84	5.08	5.24
Dielectric Constant (Ɛ)	8.32	8.63	8.63
Breakdown Voltage (MV/cm)	2.1	2.4	2.3

X-ray diffraction results revealed that the lattice structure and texture of the bottom electrode plays a vital role in c-axis wurtzite phase growth of aluminum nitride (AlN) thin films. A highly (002) oriented c-axis AlN thin film was obtained over Ti as compared to Al and Pt electrodes. The piezoelectric coefficient (d_{33eff}) of these fabricated AlN thin films were measured by piezoresponse force microscopy to evaluate their piezoelectric efficiency in resonators. AlN is a good option for passivation purpose in microelectronic devices because of high chemical stability and excellent dielectric properties. Therefore, the dielectric reliability of AlN thin films is very crucial. Among all structures, AlN/Ti structure exhibits the highest dielectric constant (ε_r) ~ 8.63 at 1 MHz. This work also provided a comprehensive study of leakage current conduction mechanism with the electric field. The leakage behavior depicts that all AlN film endures a transition from ohmic conduction ($E < 70$ kV/cm) to SCLC conduction ($E > 70$ kV/cm). Also, the breakdown characteristic of these fabricated films was studied for deciding the long-term device reliability and life. This study suggests that the electrode engineering of AlN thin films is potential in devices for electrical and micro-electro-mechanical system (MEMS) applications.

6.2. Room temperature ME coupling AlN/NiMnIn thin film structure.

In this study, Si-integrated NiMnIn/AlN magnetoelectric heterostructures were fabricated using DC magnetron sputtering. The c-axis wurtzite growth of AlN thin film over L$_{21}$ structured NiMnIn under layer is revealed by the X-ray diffraction pattern and FESEM images of AlN/NiMnIn heterostructure. The presence of typical hump in dielectric value of ME heterostructure over ~ 270 K to 294 K temperature regime could be ascribed to the transfer of strain generated during the first-order structural transformation in the NiMnIn layer. The magnetoelectric measurements of AlN/NiMnIn heterostructure show a high magnetoelectric coupling coefficient of ~99.2 V/cm Oe at 300 Oe bias field due to the large magnetic field induced strain in NiMnIn layer and higher piezoelectric voltage coefficient of the AlN layer. These results suggest the potential of AlN/NiMnIn ME heterostructure in magnetic field sensing and energy harvesting applications [**Table 6.2**].

Table 6.2 AlN/FSMA based Magnetoelectric heterostructure properties

Parameter		**Values**
Roughness (nm)	NiMnIn	2.7
	AlN	7.3
Dielectric Constant		7.8
Transformation region (T)		273 K-295 K
Dielectric tunability (@250 Oe)		0.09
ME coupling Coefficient (V/cm Oe)		99.2

6.3. Influence of encapsulating a magnetostrictive thin film on magneto-dielectric (MD) response of AlN/FSMA heterostructures.

In the present study, a lead-free magnetoelectric composite of NiMnIn (180 nm) / AlN (180 nm) / NiMnIn (50 nm) / AlN (180 nm) / NiMnIn (180 nm) structure has been fabricated using magnetron sputtering. The AlN structure with encapsulated NiMnIn layer exhibits higher dielectric permittivity, piezoelectric response and magnetodielectric response as compared to pure AlN (~360 nm) structure. The dielectric constant of the encapsulated structure was found to be about 300 % (22.3) more as compared to that of pure AlN (~ 7.24) structure. The piezoelectric coefficient of the multilayered structure was found to be about 7.49. A high value (~1268 ppm) of the magnetostriction coefficient was obtained for ferromagnetic NiMnIn layer using cantilever deflection method. The magnetic field sensing characteristics of the fabricated encapsulated structure is studied in terms of magneto-dielectric effect was as large as 8.5%. Such proposed multilayered structures with enhanced dielectric constant and good magnetodielectric characteristics are useful for future magnetic field sensing and microelectromechanical systems (MEMS) based devices applications.

6.4. Magnetic field tunable ferromagnetic shape memory alloy based piezo-resonator

In this study, we report a comprehensive analysis of the influence of the magnetic field on bulk acoustic wave (BAW) resonator consisting of a highly magnetostrictive layer and AlN thin film **[Table 6.3]**. The fundamental resonant frequency of the fabricated BAW resonator is about ~4.22 GHz. In the presence of a magnetic field, the effect on the resonator parameters such as resonant frequency, acoustic velocity, and coupling coefficient was studied. For the magnetic field of strength 1200 Oe, the resonant frequency significantly shifts by ~360 MHz. Resonant frequency increases and electromechanical coupling coefficient (k_t) decreases with the increase in the DC magnetic field. The maximum acoustic velocity of ~7350 m/sec was observed at the magnetic field of 1500 Oe when applied parallel to the surface. Agilent Advanced Design Software (ADS) was used to extract the equivalent Modified Butterworth-Van Dyke circuit parameters (R_m, C_m, and L_m) of the resonator. Further, in the presence of the magnetic field, we obtained the variation in values of R_m, C_m, and L_m of the resonator structure. Such tunable resonators can be vital in designing futuristic tunable filters, and magnetic field sensors without using the complicated fabrication process and dealing with varying frequency bands for sustainable growth in wireless communication. Further, **Table 6.4** shows the improvement in sensing parameter of the proposed device with the existing reported work.

Table 6.3 Measured parameters of the fabricated tunable resonator

Parameters		**Value**
Resonant Frequency (GHz)		4.22
Roughness (nm)		3.24
Piezoelectric Coefficient (pm/V)		4.23
Magnetostriction of FSMA (ppm)		1260
Resonant frequency (GHz)	H=0	4.22
	H=650 (Oe)	4.41
	H=1200 (Oe)	4.56
R_m (ohm)	H=0	34.2
	H=1200 (Oe)	42.7
C_m (pf)	H=0	0.063
	H=1200 (Oe)	0.062
L_m(nH)	H=0	22.68
	H=1200 (Oe)	20.01
Acoustic velocity (m/sec)	H=0	6750
	H=1200 (Oe)	7350
Coupling Coefficient (k_t)	H=0	0.22
	H=1200 (Oe)	0.19

Table 6.4. Comparison of present work with the existing literature.

Ferromagnetic	**Piezoelectric/ Substrate**	**Resonance frequency**	**Sensitivity**	**Reference**
FeGaB	**AlN**	93 MHz	~50kHz/10Oe	**[1]**
Ni	**GaN**	2.92 GHz	4123 ppm/2850Oe	**[2]**
FeCo	**ZnO**	1.2 GHz	7 MHz	**[3]**
NiMnIn	**AlN**	4.22 GHz	350 MHz	[**present work**]

Future Directions

There are various novel ideas linked to AlN based multiferroic heterostructure, on which one can continue the study in future with the following points:

- Fabrication of surface acoustic wave (SAW) resonator and thin film bulk acoustic wave resonator (FBAR) using optimized AlN thin films.
- Incorporation for new magnetoelectric composites in fabricated acoustic resonators for MEMS magnetic sensor applications.
- To explore the use to MEMS acoustic resonators for different sensors (biosensors, gas sensors, magnetic sensors, etc.) with high sensitivity.
- Different MEMS structure such as cantilever, diaphragm, etc. can also be incorporated for sensing applications.

References.

[1]. H. Lin et al., "Tunable RF band-pass filters based on NEMS magnetoelectric resonators," 2016 IEEE MTT-S International Microwave Symposium (IMS), San Francisco, CA, 2016, pp. 1-4.

[2]. A. C. Bunea, D. Neculoiu, G. Konstantinidis, A. Kostopoulos, A. Stavrinidis and G. Stavrinidis, "Magnetoelectric GaN film bulk acoustic wave resonator," 2019 IEEE Asia-Pacific Microwave Conference (APMC), Singapore, Singapore, 2019, pp. 1119-1121.

[3]. Singh, J., Kumar, A., Das, S. and Kothari, P., 2018, November. Tunable Film Bulk Acoustic Wave Resonator Based on Magnetostrictive Fe65Co35 Thin Films. In 2018 Asia-Pacific Microwave Conference (APMC) (pp. 800-802). IEEE.